

# Wake dynamics in offshore wind farms

**de Mare, Martin Tobias**

*Publication date:*
2016

# Wake dynamics in offshore wind farms

Department of Wind Energy PhD Report 2016

Martin de Maré

DTU Wind Energy PhD-0048 (EN)

September 2015

DTU Wind Energy
Department of Wind Energy

**Authors:** Martin de Maré

**Title:** Wake dynamics in offshore wind farms

**Department:** DTU Wind Energy

**DTU Wind Energy PhD-0048 (EN)**

**September 2015**

**ISBN: 978-87-93278-33-2**

**Pages:** 128

**Supervisors:**

Jakob Mann, Gunner Larsen, Leo Jensen

**Sponsorship:**

Forskings- og Innovationsstyrelsen

DONG Energy A/S

Vestas Wind Systems A/S

**Technical University of Denmark**
Department of Wind Energy
Frederiksborgvej 399
Building 118
4000 Roskilde
Denmark
Telephone 46 77 55 58

kaal@dtu.dk

www.vindenergi.dtu.dk

# Summary (English)

Wind turbines within offshore wind farms spend considerable time operating in the wake of neighboring wind turbines. An important contribution to the loads on a wake-affected wind turbine is the slow movement of the wake from the upstream wind turbine across the rotor of the wake-affected wind turbine. A new approach to this so called wake meandering is proposed. Beside the advantage of higher physical realism, the new approach also offers practical advantages compared to the current state-of-the-art method.

An input to the new meandering approach is the time evolution of the so called spectral velocity tensor. An improved such spectral tensor is therefore developed, which, for neutral atmospheric stratification, predicts spatial correlations comparably to the Mann spectral tensor and temporal coherence significantly better than previously existing models, including the Mann model, which is incapable of predicting any temporal correlations beyond those that follows from the application of Taylor's frozen turbulence hypothesis. As part of the framework a spectral tensor for Lagrangian correlations in space and time is also developed and validated versus measurements of isotropic turbulence. Combined, the models reproduce the cross-over point between Eulerian and Lagrangian temporal covariances. The applications of the Lagrangian spectral tensor, e.g. in the fields of dispersion and mixing, deserve further investigation.

The values of the input parameters of the spectral tensor are shown to be uniquely determined by the friction velocity, the shear and the dissipation of turbulent kinetic energy, all of them physical properties of the flow. If local equilibrium between the turbulent kinetic energy produced by shear and the turbulent kinetic energy dissipated as heat is assumed, then, for neutral atmospheric stratification, the friction velocity and the mixing length determine the spectral tensor.

The developed spectral tensor also depends on a dimensionless quantity, which would be beneficial to determine with higher accuracy. An experiment with this objective, studying the ratio between different components of the cross-spectra at known shear, is proposed. Future work could also include investigating if a Rapid Distortion formulation that also includes a term for buoyancy effects is needed in order to make accurate predictions for non-neutral atmospheric stratification.

# Summary (Danish)

Vindmøller i store havmølleparker tilbringer en stor del af deres tid i vindskygge af andre vindmøller. Vindskyggens bevægelse frem og tilbage over rotoren øger belastningen på vindmøllen. En ny måde at kvantificere denne langsomt mæandrerende bevægelse er foreslået. Denne nye metode er mere fysisk realistisk og giver også praktiske fordele i forhold til de gængse metoder.

Metoden bruger Fouriertransformation af turbulensens kovariansfunktionen som base. En ny model for denne såkaldte spektraltensor udvikles. Den nye model giver bedre forudsigelser af korrelationer i tid end de nuværende modeller og forudsiger korrelationer i rummet på lige fod med Manns spektraltensor. En spektraltensor for Lagrangeske korrelationer i tid og rum foreslås også, og den valideres mod målinger af isotrop turbulens. Sammen forudsiger begge modeller skæringspunktet mellem Eulerske og Lagrangeske kovarianser som funktion af tiden. Den Lagrangeske spektraltensors anvendelsesområder, inden for f.eks spredning og blanding, fortjener nærmere undersøgelse.

Værdierne for spektraltensorns parametre viser sig at være bestemte af friktionshastighed, shear og energiomdannelse til varme, som alle er fysiske egenskaber af strømningen. Hvis nydannelse af turbulens energi og omdannelse til varme antages at være i lokal ligevægt, så bestemmes spektraltensoren, ved neutral atmosfærisk stabilitet, af shear og friktionshastigheden.

Spektraltensoren afhænger også af en dimensionsløs størrelse, der med fordel kan bestemmes med større nøjagtighed. Der foreslås et eksperiment med dette formål, hvor krydsspektrets komponenter sammenlignes ved kendt shear. Det fremtidige arbejde kan også omfatte undersøgelser af, hvis en Rapid Distortion-formulering med et opdriftsled er nødvendig for at lave forudsigelser ved ikke-neutral atmosfærisk stabilitet.

# Summary (Swedish)

Vindkraftverk i stora havsbaserade vindkraftsparker tillbringar en ansenlig del av sin tid i vindskugga av andra vindkraftverk. Vindskuggans rörelse fram och tillbaka över rotorn ökar belastningen på vindkraftverket. Ett nytt sätt att kvantifiera denna långsamt meandrerande rörelse föreslås. Detta nya angreppssätt är mer realistiskt fysiskt sett och erbjuder även praktiska fördelar, jämfört med förhärskande metoder.

Angreppssättet använder Fouriertransformen av turbulensens kovariansfunktion som bas. En ny model för denna så kallade spektraltensor utvecklas. Den nya modellen ger bättre förutsägelser av korrelationer i tid än nuvarande modeller samt förutsäger korrelationer i rummet i paritet med Mann's spektraltensor. En spektraltensor för lagranska korrelationer i tid och rum föreslås också, och den valideras gentemot mätningar av isotropisk turbulens. Tillsammans förutsäger de båda modellerna skärningspunkten mellan eulersk och lagransk kovarians som funktion av tiden. Den lagranska spektraltensorns användingsområden, inom exempelvis dispersion och blandning, förtjänar närmare studier.

Värdena på spektraltensorns parametrar visas vara bestämda av friktionshastigheten, skjuvningen och energiomvandlingen till värme, vilka alla är fysiska egenskaper hos flödet. Om tillförseln av turbulensenergi och omvandlingen till värme antas vara i lokal jämvikt så bestäms spektraltensorn, vid neutral atmosfärisk stabilitet, av skjuvningen och friktionshastigheten.

Spektraltensorn beror också på en dimensionslös kvantitet som med fördel kan bestämmas med större noggrannhet. Ett experiment med detta ändamål föreslås, där korsspektrets komponenter jämförs vid känd skjuvning. Kommande arbete skulle även kunna inkludera undersökningar av om en Rapid Distortion-formulering med en flytkraftsterm behövs för att göra förutsägelser vid icke-neutral atmosfärisk stabilitet.

# Preface

The project was initiated at Vestas Wind Systems A/S by my former manager, Jens Jakob Wedel-Heinen, and Senior Specialist Dick Veldkamp. In the context of developing the V164-8MW wind turbine, which is aimed for the offshore market, Vestas wanted to learn more about the operating environment within large offshore wind farms. Together with Professor Jakob Mann and Senior Scientist Gunner C. Larsen at DTU Wind, we applied to Forskings- og Innovationsstyrelsen and were granted a 3 year Industrial PhD project.

Encouraged by the Industrial PhD Programme, 5 months were spent in Professor Julie Lundquist's group at Colorado University in Boulder, Colorado. While in Boulder my fellow Vestas PhD-student Rolf-Erik Keck and I cooperated with Pat Moriarty, Matt Churchfield and Sang Lee at the National Renewable Energy Laboratory (NREL). I also interacted with Branko Kosovic and Ned Patton at the University Corporation for Atmospheric research (UCAR).

When Vestas drastically downsized its research organization 22 months into the project, the project was taken over by DONG Energy. The final 14 months of the project I was located in the Loads Aerodynamics and Control Department headed by Torben Søndergaard, under the supervision of Chief Specialist Leo Jensen.

The thesis was completed at the Wind Assessment Department, headed by Raymond Downey.

Gentofte, September 2015

Martin de Maré

# Acknowledgements

I would like to thank Jens-Jakob Wedel-Heinen and Dick Veldkamp for initiating and supporting the project at Vestas Wind Systems A/S.

I owe gratitude to Julie Lundquist and Branko Kosovic for welcoming me in Boulder, and Pat Moriarty, Matt Churchfield and Sang Lee at NREL and Ned Patton at UCAR for generously sharing time and data.

Thank you, Rolf-Erik and AnnLouise Keck, for a fantastic time in both USA and Scandinavia! On that note, I am also grateful that our old Saturn made it through Death Valley in one piece!

At DONG Energy, I would like to thank Torben Søndergaard and Leo Jensen for championing the project, and Raymond Downey for his patience. I would also like to thank my colleagues in LAC and WAM for interesting discussions and encouragement.

At DTU, I would like to thank Søren Ott for interesting discussions and feedback, Steen Sørensen for facilitating access to measurement data, and Jakob Mann and Gunner Larsen for being generous with both time and guidance, and always being supportive and encouraging!

Finally, I would like to thank my sisters and their families, and my parents, for all their help, encouragement and support!

# List of Papers

Paper A: **On atmospheric stability in the dynamic wake meandering model**

Rolf-Erik Keck, Martin de Maré, Matthew J. Churchfield, Sang Lee, Gunner Larsen and Helge Aagaard Madsen

*Wind Energy, Volume 17, Issue 11, pp 1689–1710, Nov 2014*

Paper B: **A new approach to modelling the meandering of a wind turbine wake in homogeneous turbulence**

Martin de Maré, Jakob Mann, Matthew J. Churchfield and Edward G. Patton

*EWEA Offshore Conference 2013*

Paper C: **Validation of the Mann spectral tensor for offshore wind conditions at different atmospheric stabilities**

Martin de Maré and Jakob Mann

*Journal of Physics: Conference Series Volume 524, Conference 1, 2014*

Paper D: **On the space-time structure of sheared turbulence**

Martin de Maré and Jakob Mann

*Accepted by Boundary-Layer Meteorology*

# Contents

Chapter 1

# Introduction

Wind is driven by high and low pressure in the atmosphere. As we approach the ground, the wind speed eventually goes to zero. As depicted in Figure 1.1 we thus have a vertical gradient in the horizontal flow velocity, or shear. If the Reynolds number, i.e. the flow speed times the flow depth divided by the (kinematic) viscosity, is high enough, turbulence, i.e. chaotic fluctuations in the flow velocity, will occur. The dimensions of the flow are so large and the viscosity of air is so low that wind is almost always turbulent.

Turbulence can be driven by processes other than shear. One example is turbulence driven by heat. This process can be observed when water being heated starts convecting well before reaching the boiling point. In the atmosphere, shear driven turbulence and heat driven turbulence usually occur in conjunction, and the relative strength of these processes defines the so called atmospheric stability. This term originates from the observation that heating of the ground magnifies the shear driven turbulence, and the atmosphere is said to be unstable. In the opposite situation when the ground is cooler, the resulting temperature gradient dampens the shear driven turbulence, and the atmosphere is said to be stable. When neither stable nor unstable the atmosphere is said to be neutral. Atmospheric stability can be quantified by the so called *Monin-Obukhov length* (Monin and Obukhov, 1959). We will follow Peña et al. (2010), where the Monin-Obukhov length was used to define the stability classes Very Unstable (VU), Unstable (U), Near Unstable (NU), Neutral (N), Near Stable (NS), Stable (S) and Very Stable (VS). For an introduction to atmospheric turbulence see e.g Stull (1988) or Wyngaard (2010).

Turbulence can be studied in the virtual world, using the Finite Volume method where the governing equations, i.e. the Navier-Stokes equations, are discretized and applied to a calculation domain divided into small calculation cells. For wind turbine applications, the need to resolve the smallest scales of turbulence leads to unmanageably large numbers of calculations cells. Large Eddy Simulations (LES) attempts to reduce the computational requirements by resolving only the largest eddies. The effect of the small scale eddies are instead modeled by a sub-grid turbulence model (Wyngaard, 2010).

Turbulence can also be studied in various experimental setups, however, due to the

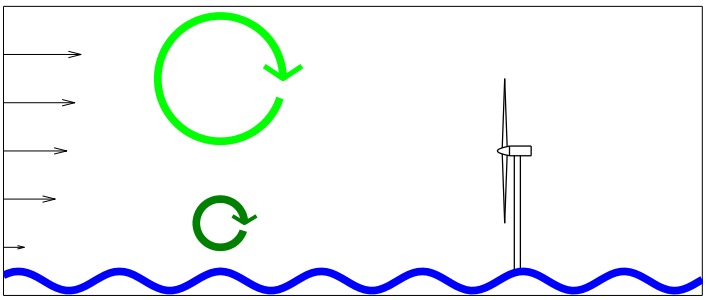

**Figure 1.1:** The wind speed approaches zero close to the surface, giving rise to a vertical gradient in the horizontal flow velocity (the black arrows), i.e. shear. At sufficiently high Reynolds numbers, shear gives rise to turbulent eddies (green).

chaotic nature of turbulence no matter how well the initial conditions are controlled each realization of turbulence will inevitably be different, making it challenging, to say the least, to make deterministic predictions. Statistical predictions can, however, be made, and this will be discussed next.

## 1.1 Describing turbulence statistically

Let us first consider a very different phenomenon, namely breaking waves at open sea. We know that at some wind speed (usually said to be between 6 to 8 m/s) breaking waves can be observed at the open sea. We know the equations of the physics involved, however, even so, we cannot predict which wave will break when. Even though we cannot predict the details in a deterministic sense, on a statistical level we can still study it. We can determine the mean wave height as a function of wind speed, or in more detail the expected distribution of wave height and wave lengths. This statistical information can then, for example, be used to simulate realistic ocean waves which in turn is useful when validating designs of offshore structures or ships.

The situation is similar for the study of turbulence. We know the conditions when turbulence occurs, and we know the governing equations. However, even with the afore-mentioned Finite Volume method, we cannot predict the turbulent fluctuations accurately for very long. But we can describe turbulence in a statistical sense, and this statistical description can be used to generate realistic 3-dimensional wind fields for validation of the designs of wind turbines, buildings and bridges (Mann, 1998).

It is common to assume statistical stationarity (as well as ergodicity), which means

that the 3-dimensional flow velocity $\tilde{\boldsymbol{u}}(\boldsymbol{x},t)$ can be (Reynolds) decomposed into a mean velocity, $\boldsymbol{U}(\boldsymbol{x})$, and a fluctuating part, $\boldsymbol{u}(\boldsymbol{x},t)$, according to $\tilde{\boldsymbol{u}}(\boldsymbol{x},t) = \boldsymbol{U}(\boldsymbol{x}) + \boldsymbol{u}(\boldsymbol{x},t)$. It follows that the expected value (the mean value if observed long enough) of the fluctuating part, $\langle \boldsymbol{u}(\boldsymbol{x},t) \rangle$, is $\mathbf{0}$.

After some manipulations of the Navier-Stokes equations, the expected transfer of energy from the mean flow into turbulent kinetic energy is given by $\langle -u_1 u_3 \rangle \frac{\partial U_1(z)}{\partial z}$. Introducing the *friction velocity*, $u_* = \sqrt{-\langle u_1 u_3 \rangle}$, the expected transfer of energy from the mean flow into turbulent kinetic energy is $u_*^2 \frac{\partial U_1(z)}{\partial z}$. The larger the eddy, the more efficient it is in extracting energy from the mean shear gradient. In parallel, due to viscosity, a portion of the turbulent kinetic energy continually transforms into heat. The rate of this dissipation of energy, per unit mass of the fluid, is denoted $\epsilon$. This dissipation is more efficient in the small scales. The scales in between, which are involved in the transfer of energy from the large scales (that extract energy) to the small scales (that dissipate energy), make up the inertial subrange. For an introduction to turbulence theory see e.g. Tennekes and Lumley (1972).

We define the coordinate system to move with a suitable velocity, $\boldsymbol{U_0}$, so that in our coordinate system $\boldsymbol{U}(\mathbf{0}) = \mathbf{0}$. We further assume a constant and non-negative shear, $\frac{\partial U_1}{\partial z}$, such that

$$\tilde{\boldsymbol{u}}(\boldsymbol{x},t) = \boldsymbol{U}(\boldsymbol{x}) + \boldsymbol{u}(\boldsymbol{x},t) = (x_3 \frac{\partial U_1}{\partial z}, 0, 0) + \boldsymbol{u}(\boldsymbol{x},t). \tag{1.1}$$

If we also assume that $\boldsymbol{u}(\boldsymbol{x},t)$ is statistically homogeneous, then we can define a covariance tensor, $R_{ij}$, which describes the covariance of the flow at $\boldsymbol{x}$ and $\boldsymbol{x}+\boldsymbol{r}$, and at $t$ and $t+\tau$. We account for the mean velocity of the flow varying with height by including a term $\boldsymbol{U}(\boldsymbol{x}+\boldsymbol{r})\tau$ according to

$$R_{ij}(\boldsymbol{r},\tau) = \langle u_i(\boldsymbol{x},t)\, u_j(\boldsymbol{x}+\boldsymbol{r}+\boldsymbol{U}(\boldsymbol{x}+\boldsymbol{r})\tau, t+\tau) \rangle\,. \tag{1.2}$$

The role of $\boldsymbol{U}(\boldsymbol{x}+\boldsymbol{r})\tau$ is easiest to demonstrate for $\boldsymbol{r} = 0$, when it causes the right-hand side of (1.2) to denote the covariance at a point which moves with the mean flow velocity, $\boldsymbol{U}(\boldsymbol{x})$.

Turbulence is said to consist of eddies, a concept that in practice is hard to both define and to work with. Mathematically, it is more convenient to describe turbulence in the Fourier domain, which means that the turbulent fluctuations are seen as a super-position of sine-waves. We therefore continue by defining the spectral velocity tensor

$$\widehat{R}_{ij}(\boldsymbol{k},\tau) = \frac{1}{(2\pi)^3} \iiint R_{ij}(\boldsymbol{r},\tau)\, e^{-\mathrm{i}\,\boldsymbol{k}\cdot\boldsymbol{r}} \mathrm{d}\boldsymbol{r}. \tag{1.3}$$

An improved model for $\widehat{R}_{ij}(\boldsymbol{k}, \tau)$ is discussed in 2.4 and is one of the key contributions presented in this thesis.

## 1.2 Loads on offshore wind turbines

Offshore wind turbines are subjected to the full force of the sea, with waves and perhaps ice battering the structure. The loads induced by these forces have to be accounted for when designing especially the foundations. Additionally the wind turbine and its foundation have to be strong enough to withstand the loads resulting from the interaction with the wind. For a solitary wind turbine, these wind induced loads are well understood and can be predicted using aero-elastic simulations, which somewhat simplified can be described as simulated turbulent wind interacting with components of the wind turbine described by beam-theory.

Light detection and ranging (lidar) systems use the Doppler shift in the laser light that is returned from microscopic particles to remotely determine the wind speed. Researchers are investigating whether forward-looking lidar systems can reduce mechanical loads on wind turbines by anticipating incoming gusts (Pao and Johnson, 2011; Bossanyi et al., 2012; Mikkelsen et al., 2013). The question arises whether the turbulent fluctuations measured upstream of the rotor would arrive unchanged to the rotor a moment later (Bossanyi, 2013). Related questions are how many laser beam directions (i.e. measurement points) will characterize the fluctuations in an optimal way (Schlipf et al., 2013), and how the significant probe volume of the lidar influences the measurements (Sathe and Mann, 2013). All these issues depend on the spatial *and* temporal structure of sheared turbulence, the topic of 2.4.

Now, consider two wind turbines and the wind direction such that one of the turbines is operating in the wake of the other. The energy extracted from the wind by the upstream wind turbine leaves a wind speed deficit which is advected downstream in the direction of the ambient wind. Bingöl et al. (2010) observed that the velocity at which the wake moves downstream differs from the mean wind speed. A method for determining this *wake transport velocity* is discussed in section 2.1.

Large scale turbulence causes the wind speed deficit to meander like a river (España et al., 2012). This meandering causes the wind speed deficit to move back and forth over the rotor of the wake-affected turbine, and this in turn results in increased loads on the wind turbine and its foundation, as is illustrated in Figure 1.2. A wind turbine in the middle of a modern offshore wind farm may very well spend most of its life in the wake of other wind turbines. It is therefore important for offshore wind turbine and foundation design to be able to accurately predict wake-induced loads.

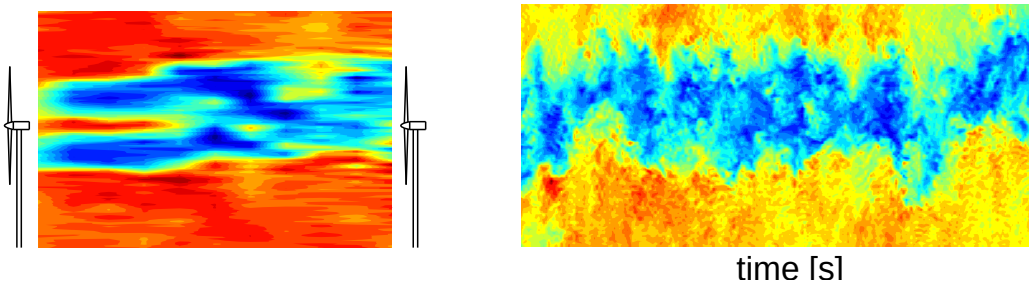


**Figure 1.2:** To the left, Large Eddy Simulations of a wake from an upstream wind turbine hitting a downstream wind turbine. To the right, the wind field as experienced by the downstream wind turbine, as a function of time. The movement of the wake deficit back and forth over the rotor increases the loads on the wake-affected wind turbine and its foundation.

## 1.3 The Dynamic Wake Meandering model

If wind turbines are represented in Large Eddy Simulations, loads can be calculated. This is, however, very computationally expensive and is therefore unfeasible for many engineering applications. There is a large number of less expensive wind turbine wake models of differing scope and complexity (Sanderse, 2009). One of the leading engineering models for the quantification of the loads of a wind turbine operating in the wake of another wind turbine is the Dynamic Wake Meandering Model (DWM), (Larsen et al., 2008; Madsen et al., 2010; Keck, 2013). The model initially calculates the wake deficit evolution as if no meandering was present. The calculation assumes that the incoming wind field is isotropic, i.e. similar in all directions and thus effects of the ground (including shear) are disregarded. The benefit of this assumption is that the result will be circular symmetric, and thus the (Reynolds averaged) Navier-Stokes equations only have to be solved in two spatial dimensions. To further reduce computational complexity, steady state is assumed, which means that the wake deficit changes with the downstream distance, but at a fixed distance the deficit is constant in time. The solution process also employs a number of additional simplifications, all with the aim of reducing computational complexity.

The turbulence intensity (which is defined as the relative standard deviation of $\tilde{u}_1$ during 10 minutes) is an input to the deficit calculation, as increased ambient turbulence leads to more mixing and thus more efficient wake dissipation. The gradient of the deficit will itself generate small scale turbulence and this wake-added turbulence influences the evolution of the wake deficit. The wake-added turbulence will not add to the meandering due to its small scale, but it still has to be accounted for when calculating the loads of the wake-affected turbine.

In order to account for wake meandering, the wake center is displaced according to a time series. This time series is generated by simulating the flight-paths of rotor-sized disc-shaped neutrally buoyant balloons advected downstream by a field of frozen turbulence which moves with the mean wind speed. If the disc-shaped balloons are released frequently enough their recorded horizontal and vertical displacements, after traveling for a time given by the wind turbine separation divided by the mean wind speed, will approach a continuous time series. This continuous time series is then the meandering time series that will combine with the deficit calculation in order to produce an input wind field to the load simulations of wake affected turbines. Larsen et al. (2008) proposed low-pass filtering the frozen turbulence field as a proxy for the disc-averaging, and defined the filter based on a wake diameter extracted from the deficit calculation rather than the rotor diameter. That paper also argued that the longitudinal turbulence component can be omitted when calculating meandering, a simplification which confines each wake segment to its own 2-dimensional plane of turbulence.

Assuming turbulence to be a frozen 3-dimensional field moving with the mean wind speed, has been very fruitful for applications where turbulence is studied from a stationary point. For that situation, “new” turbulence arrives continuously to the observation point. When following the flow as our disc-shaped balloons do, the frozen turbulence assumption likely leads to the experienced turbulence being unrealistically static. This motivates the formulation of a new approach to wake meandering which is presented in 2.3.

Wind turbine wake meandering is in DWM formulated as dispersion, analogous, for example, to a pollutant continuously being emitted from the chimney. Such applications traditionally employ tools from a *Lagrangian* analysis of turbulence (as opposed to the Eulerian approach in (1.1)), which means that turbulence is studied by following real or fluid particles released in the turbulent flow. We therefore introduce the Lagrangian covariance tensor defined by

$$R_{ij}^{\mathrm{L}}(\boldsymbol{r},\tau) = \left\langle u_i(\boldsymbol{x},t_0)\, u_j\big(\boldsymbol{X}_{t_0}^{\mathrm{L}}(\boldsymbol{x}+\boldsymbol{r},t_0+\tau),t_0+\tau\big)\right\rangle, \tag{1.4}$$

where $\boldsymbol{X}_{t_0}^{\mathrm{L}}(\boldsymbol{x},t)$ is the position at $t$ of the fluid particle which at $t_0$ was at $\boldsymbol{x}$. Analogously to (1.3), the Lagrangian spectral tensor is defined through

$$\widehat{R}_{ij}^{\mathrm{L}}(\boldsymbol{k},\tau) = \frac{1}{(2\pi)^3}\iiint R_{ij}^{\mathrm{L}}(\boldsymbol{r},\tau)\, e^{-\mathrm{i}\,\boldsymbol{k}\cdot\boldsymbol{r}}\mathrm{d}\boldsymbol{r}. \tag{1.5}$$

The formulation of a model for (1.5) is discussed in 2.5. This model likely has applications also in the fields of dispersion and mixing, see Yeung (2002) and references therein.

The meandering time series, corresponding to some downstream distance, is combined with the calculated deficit at the same downstream distance. To this, now, meandering wake deficit, synthetic atmospheric turbulence as well as synthetic small scale wake-added turbulence is added to form a wind field that includes wakes. This wind field can now be used as input to the afore-mentioned aeroelastic simulation, and loads can be calculated. The right-hand graph of Figure 1.2 gives an idea of what the DWM is aiming to accomplish.

Chapter 2

# Research topics

Meandering is a major contributor to wake dynamics, and especially so in the DWM model, where the wake deficit calculation is time-independent. As part of the research effort, different aspects of wake meandering are investigated, from the underlying turbulence description, via methods of calculating meandering time series from turbulence, to the added complication of a wake transport velocity. Chronologically these topics were researched in the reverse order and, therefore, that is the order they are presented here.

## 2.1 The wake transport velocity

Bingöl et al. (2010) observed that the velocity with which the wake moves downstream differs from the mean wind speed. We investigated this *wake transport velocity* and published the result in Keck et al. (2014). The paper also contains other results, an introduction to which can be found in Keck (2013).

Wind turbines can be represented in LES simulations in a number ways. In Keck et al. (2014) a single wind turbine is represented by actuator lines, which models the wind turbine blades only in terms of their resulting lift and drag forces (Troldborg, 2009). The wake transport velocity is investigated by studying time series of the wake centre position at two downstream sampling planes. By shifting one of the time series in time, it is possible to obtain the time offset which yields the maximum correlation, see Figure 2.1. The time offset corresponds to the transport time between the sampling planes, and the wake transport velocity is found by dividing the distance between the sampling planes with this transport time. The transport velocity for a range of cases is presented in Figure 2.2. From the figure it is concluded that the wake transport depends on, at least, turbulence intensity.

The paper concludes that the transport velocity lies between the mean flow velocity in the wake deficit and the ambient wind speed, and proposes using 80% of the ambient wind speed as an approximation of the wake transport velocity for now. The transport velocity has independently been studied in Machefaux et al. (2014).

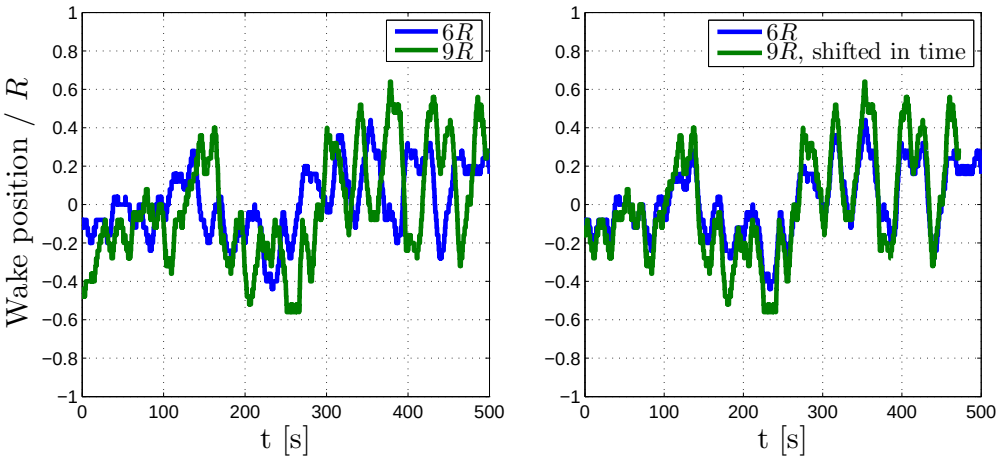


**Figure 2.1:** The left-hand graph shows the center position of the wake deficit in LES as a function of time, at two sampling planes, locacted 6 and 9 rotor radii, respectively, downstream of the wind turbine. The right-hand graph shows the same time series of wake centre position, but includes a time offset to find the best correlation between the time series.

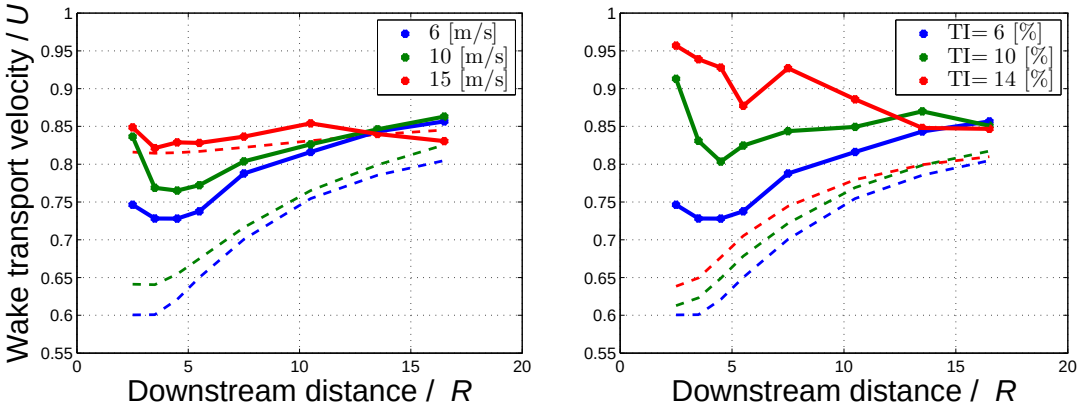


**Figure 2.2:** The wake transport velocities. The left-hand graph shows the effect of different ambient wind speeds at 6% turbulence intensity for different wind speeds. The difference between the curves is likely not an effect purely of increased wind speed, but rather an effect of the control system of the wind turbine behaving differently at different wind speeds (e.g. curtailing the production to rated power). The right-hand graph shows the influence of turbulence intensity at 6 $ms^{-1}$ wind speed. The dashed lines represent the mean flow velocity in the wake and is included for reference.

## 2.2 Meandering and Atmospheric stability

Paper A accounts for the effects of atmospheric stability in the DWM model by using the turbulence description offered by Mann spectral tensor parameter values derived from measurements. This is done under the assumption that, even though developed for neutral conditions, the Mann spectral tensor can be used to describe also non-isotropic turbulence. A sizable portion of Paper A investigates the effect of atmospheric stability on the wake deficit calculation. For an introduction to this research see Keck (2013). Here we will focus on the portion of Paper A that investigates the influence of atmospheric stability on meandering.

In Paper A the following methodology is used to generate a meandering time series

1. Based on the parameter values reported in Peña et al. (2010), the Mann spectral tensor is used to generate random Fourier coefficients in three dimensions.

2. The Fourier-equivalent of disc averaging is applied to obtain "the wind field as seen by a rotor-sized disc-shaped balloon".

3. Rotor-sized disc-shaped balloons are released at the wake-emitting wind turbine at a frequency of 1 Hz. The balloons travel with a wake transport velocity of 80% of the ambient wind speed (see section 2.1). The large box of frozen turbulence travels along the flow with the ambient wind speed. Consequently, the wake deficit travels at a negative speed of -20% of the ambient wind speed relative to the frozen turbulence field.

4. At every time step, the position of each emitted balloon is updated based on velocities in the streamwise, lateral and vertical directions, given by the current position in the turbulence box. When a balloon has traveled for the time given by the turbine separation divided by the wake transport velocity, its vertical and horizontal position is recorded. The combined registrations of all the balloons form a meandering time series for the downstream distance in question.

5. There are always turbulent structures too large to be captured by the generated turbulence box. The final step of the algorithm is therefore to multiply the time series by a factor that corrects for the resulting loss of meandering variance.

The afore-mentioned method is compared with LES data provided by the National Renewable Energy Laboratory (NREL) with wind turbines represented by actuator lines. In the LES data, the wake center is detected for every time step for a

number of downstream distances. In Figure 2.3, the resulting meandering time series is shown as the black line at downstream distances corresponding to 3 and 9 diameters, respectively.

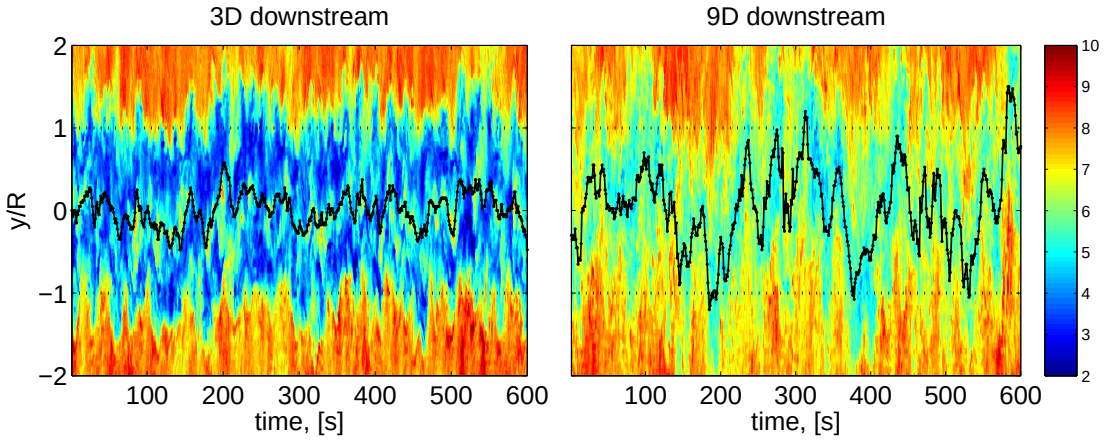


**Figure 2.3:** The graphs show wind speed extracted at two downstream distances in Large Eddy Simulations, high wind speeds in red and lower wind speed towards the blue end. The center point of the wake deficit is detected, resulting in the meandering time series in black. (The graphs are from Paper B.)

In Figure 2.4, we compare the standard deviation of the meandering time series simulated in LES with the predicted standard deviations using the DWM methodology. We find that our algorithm predicts the standard deviation of meandering well for neutral conditions (green lines), but significantly underestimates the standard deviation of the lateral meandering for the very unstable case. The observed discrepancy may warrant further study, e.g. using a spectral tensor that includes buoyancy effects consistently in its formulation.

## 2.3 A new approach to wake meandering

As detailed in the previous section, the meandering time series in the DWM model is generated by simulating the flight-paths of disc-shaped balloons advected downstream by a field of frozen turbulence which moves with the mean wind speed. We observe that releasing balloons with regular time intervals in a moving field of frozen turbulence is exactly equivalent to releasing them all at once along a straight line in the direction of the mean wind velocity. This observation inspired the main assumption of Paper B: that the spatial statistics of balloons, released all at once, can be used to approximate the statistics of an actual meandering time series also in non-frozen turbulence. Some kind of transform has to be applied before the resulting spatial statistics are interpreted as a temporal statistics, and Paper B takes

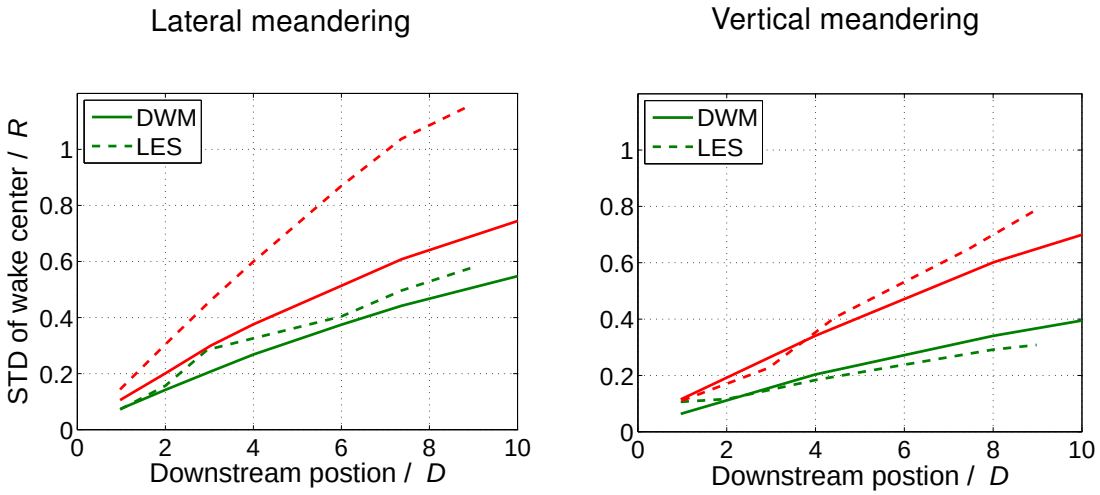


**Figure 2.4:** Standard deviation of meandering simulated in LES compared with the predicted standard deviations using the DWM methodology. We find that the our algorithm predicts the standard deviation of meandering well for neutral conditions (green lines) , but significantly underestimates the lateral meandering for the very unstable case (red lines).

advantage of the fact that the necessary transform can be derived from equivalence in the frozen turbulence case.

The resulting model is presented for $M_{ij}(f,s)$, the expected Fourier transform of the meandering time series, $\mathbf{m}(t,s)$ ,

$$M_{ij}(f,s) = \int \langle m_i(t,s) \cdot m_j(t+\tau,s) \rangle \, e^{-i\tau 2\pi f} d\tau \,. \tag{2.1}$$

where $s$ denotes the observation point. Knowing $M_{ij}(f,s)$ we can then generate realistic realizations of meandering time series, $m_i(t,s)$, which can be used in the DWM model. The final model, as presented in paper B, is more complex than (2.1), mainly due to the incorporation of the wake transport velocity.

The developed model requires knowledge of the spectral velocity tensor, $\widehat{R}_{ij}(\boldsymbol{k},\tau)$. However, the Mann spectral tensor, Mann (1994), provides this quantity only for $\tau = 0$. In Paper B, $\widehat{R}_{ij}(\boldsymbol{k},\tau)$ is approximated by a generalized version of

$$\widehat{R}^{iso}_{ij}(\mathbf{k},\tau) = \widehat{R}^{iso}_{ij}(\mathbf{k},0) e^{-\frac{1}{2}a^2 \langle u_1 u_1 \rangle |k|^2 \tau^2} \tag{2.2}$$

which was suggested by Hunt et al. (1987). In Ott and Mann (2005), (2.2) was tested for isotropic turbulence and the value $\frac{1}{2}$ was recommended for the constant, $a$.

In Figure 2.5 we compare the auto-spectra of the measured meandering time series in Figure 2.3 with the developed model, (2.1), as well as with spectra calculated using the frozen turbulence method, as described in section 2.2.

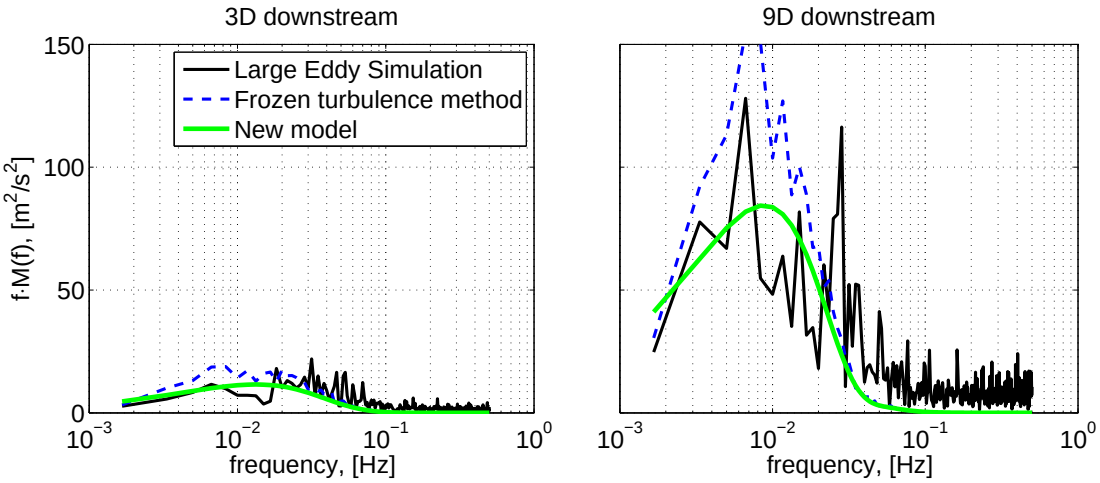


**Figure 2.5:** Comparison of the developed meandering model, (2.1), with auto-spectra calculated from the time series shown in Figure 2.3, as well as spectra calculated using the frozen turbulence method described in section 2.2.

The current state-of-the-art method based on frozen 3D wind fields tends to be quite computer memory intensive. The reason is that the larger the wind field the more of the large scale turbulent energy is represented (as indicated by the last step in the algorithm in section 2.2). There is therefore an incentive to work with the largest wind field the computer can handle. The proposed method on the other hand predicts the auto-spectra of the meandering time series without generating 3D wind fields. Realizations of meandering time series can therefore be generated with modest computing requirements. Thus, beside the theoretical advantage of un-freezing the turbulence, the new approach also offers practical advantages.

## 2.4 The time evolution of turbulence

In the previous section we mentioned that Ott and Mann (2005) recommended setting $a = \frac{1}{2}$ in (2.2) based on measurements of isotropic turbulence. However, in the Appendix we show theoretically that in the inertial sub-range $a$ should approach $1$. This result would favor the original formulation by Saffman (1963), more recently also proposed by Wilczek and Narita (2012), thus contradicting the empirical benchmarking effort in Ott and Mann (2005). These observations motivate interest in the formulation of an alternative model for $\widehat{R}_{ij}(\boldsymbol{k}, \tau)$.

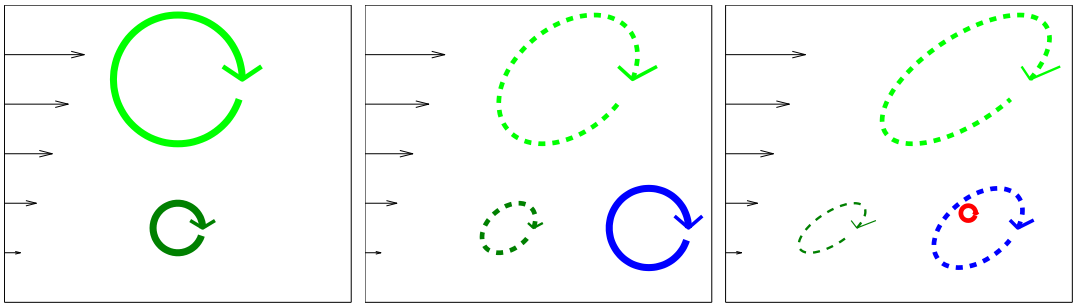

**Figure 2.6:** The three graphs show a sequence of snapshots of conceptional turbulence being distorted by shear (illustrated by the black arrows). The two green eddies are being rapidly distorted (from circles to ellipses) while at the same time decaying (illustrated by the shift from solid lines to dashed lines). The thickness of the dashed lines in the right-most graph indicates that the smaller, dark green, eddy decays faster than the larger, light green, eddy. We also notice the new-born blue eddy in the middle graph and the like-wise new-born red eddy in the right-most graph.

The new model rests to a large extent on the framework developed in Mann (1994), where isotropic turbulence is distorted by Rapid distortion theory (Moffatt, 1967; Townsend, 1976). Figure 2.6 shows a sequence of snapshots of conceptual turbulence in which Rapid Distortion theory is responsible for the circles, in the graphs, changing into ellipses. In the graphs, the turbulent eddies are also continuously decaying, illustrated by the shift from solid lines to dashed lines. This continuous decay is in mathematical terms achieved by introducing a decay term to the Rapid Distortion equation, which is then referred to as the *eddy decay equation*. The decay term uses the *eddy lifetime*, which in Paper D is given by

$$\tau_e(\boldsymbol{k}) = \tau_e(|\boldsymbol{k}|) = \frac{M}{\sqrt{\alpha_{\mathrm{K}}}}|\boldsymbol{k}|^{-\frac{2}{3}}\epsilon^{-\frac{1}{3}}. \tag{2.3}$$

where the quantity $M$ has been introduced. In Paper C, $M$ is estimated to around 3. Paper D quantifies the uncertainty of this estimate to around 20% and goes on to suggest an experiment which may be more appropriate for determining $M$ than the methodology chosen in paper C.

As a contrast, instead of decaying, the eddies in Mann (1994) are subjected to Rapid distortion according to their current age, which is set to the eddy life time.

The sequence of snapshots is continued in Figure 2.7. The dashed black lines which illustrate the evolution in time of a sample wave number, remind us that the model is formulated as a function of wave number. Kristensen's longitudinal coherence model (Kristensen, 1979) (which describes the coherence of the turbulent fluctuations as measured by two meteorologically instrumented measurement

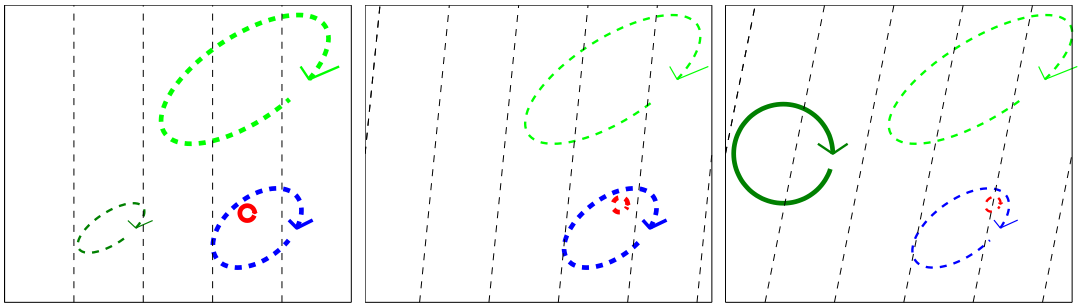

**Figure 2.7:** The three graphs continue the sequence of snapshots of conceptional turbulence in Figure 2.6. The left-most graph is identical to the last graph of Figure 2.6, except that the shear is now illustrated by the dashed black lines which represent a wave number evolving according to $\boldsymbol{k}(\tau) = (k_1, k_2, k_3 - \frac{\partial U_1}{\partial z}\tau\, k_1)$. In the two right-most graphs we notice that the blue eddy is advecting the smaller red eddy, causing it to move relative to the illustrated wavenumber.

masts) incorporated loss of correlation due to the afore-mentioned process of eddy decay, but also loss of correlation due to larger eddies advecting smaller ones. In the two right-most graphs of Figure 2.7 this process, which is also referred to as *sweeping*, is illustrated by the blue eddy advecting the smaller red eddy. In the new model, the loss of correlation is due to the movement of the red eddy relative to the illustrated wavenumber.

The detailed formulation of the model is discussed in Paper D, in which the model is validated versus Large Eddy Simulations obtained from the National Center of Atmospheric Research (NCAR). The validation section also includes comparisons with the experiments presented in Ott and Mann (2005), see the left-hand graph of Figure 2.8. The new spectral tensor is found to perform significantly better than any of the models evaluated in that, same, paper.

## 2.5 A model for the Lagrangian tensor

The Lagrangian approach can be described as observing the flow by tracking fluid particles and recording their instantaneous velocities. If we follow one of the fluid particles within the small red eddy of Figure 2.7 and use it to study the wavenumber illustrated by the dashed black lines, then it is clear that the Lagrangian velocity may lose coherence even when, as in this case, the blue eddy (which likely contributes to the illustrated wavenumber) stays more or less coherent. Our assumption is therefore that the evolution of the Lagrangian tensor is a combination of eddy decay and the fluid particles moving relative to the eddies of which they

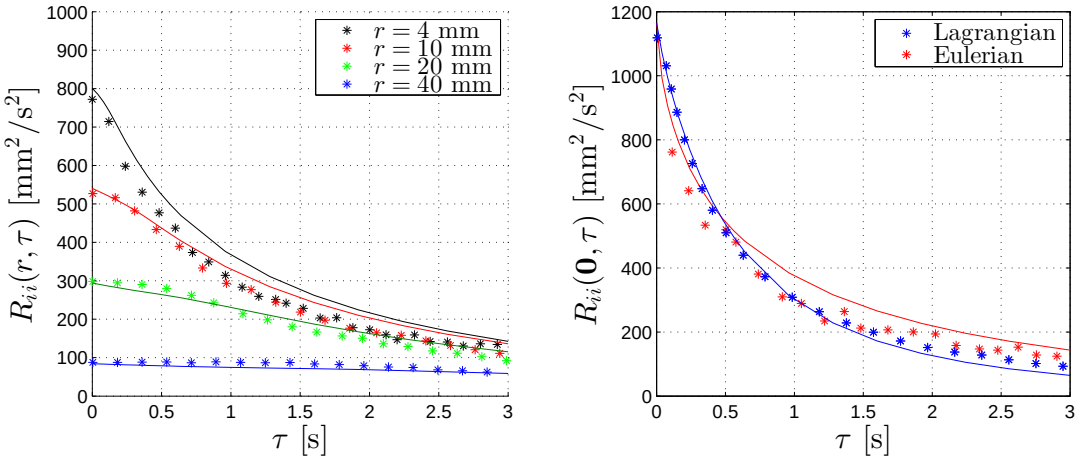


**Figure 2.8:** Sum of covariances for all three components derived from the spectral tensor (solid lines) compared to measured results for isotropic turbulence presented in Ott and Mann (2005). To the left, Eulerian covariance for various separations in space, $\boldsymbol{r}$, and time. To the right, a comparison between the Eulerian and the Lagrangian covariance for $\boldsymbol{r} = \mathbf{0}$.

are a part. Inspired by the Eulerian tensor and the above arguments, a model for $\widehat{R}^{\mathrm{L}}_{ij}(\boldsymbol{k},\tau)$ of (1.5) is introduced in Paper D. In the right-hand graph of Figure 2.8, both tensors are validated versus measured data presented in Ott and Mann (2005). We see that our models reproduce the cross-over of $R^{\mathrm{L}}_{ii}(\mathbf{0},\tau)$ and $R_{ii}(\mathbf{0},\tau)$ at approximately half the maximum value, a behavior also reported in Fung et al. (1992).

The Lagrangian spectral tensor was a late discovery in the project, and it deserves to be investigated and validated to a larger extent. It likely has applications, for example, in the fields of dispersion and mixing, see the review in Yeung (2002) and references therein.

## 2.6 The parameters of the spectral tensors

The Mann spectral tensor scales with the dissipation of turbulent kinetic energy, $\epsilon$, according to $\epsilon^{\frac{2}{3}}$. In practice it is convenient to combine $\epsilon^{\frac{2}{3}}$ with the Kolmogorov constant, to get $\alpha_{\mathrm{K}}\epsilon^{\frac{2}{3}}$. Furthermore the Mann spectral tensor depends on a length scale parameter, $L_M$, and a dimensionless parameter $\Gamma$ and can thus be written $\widehat{R}_{ij}\left(\alpha\epsilon^{\frac{2}{3}}, L_M, \Gamma, \boldsymbol{k}, 0\right)$.

For many applications, it is not obvious how to set the values of these input param-

eters, and they can instead be determined by fitting the spectra as derived from the spectral tensor to measured spectra (Mann, 1994). Paper C investigates how the values of $\alpha\epsilon^{\frac{2}{3}}$, $L_M$ and $\Gamma$ of the Mann spectral tensor, vary with height for the offshore site Rødsand II. Although the Mann spectral tensor was developed for neutral atmospheric stability, Paper C follows Peña et al. (2010) and Chougule (2013) and applies it also to non-neutral stability conditions.

The general behavior of the parameter values, obtained from the fitting procedure, are consistent with the observations in Chougule (2013) and Peña et al. (2010) except for the value of the parameter $\Gamma$, which in Paper C and in Chougule (2013) decreases with degree of stability, while Peña et al. (2010) reports a more complex behavior. The observed ratio between the mixing length, $l_{\mathrm{mix}} = u_*/\left(\frac{\partial U_1}{\partial z}\right)$and $L_M$, agrees reasonably well with the $\frac{1}{1.70} \approx 0.59$ presented in Peña et al. (2010).

High energy levels at low wave numbers are observed in the spectra, especially in the streamwise and the transversal components, and are not matched in the Mann spectral tensor spectra. Paper C argues that this is a contribution from the very large scale *quasi-geostrophic* turbulence, discussed e.g. in Lindborg (1999) and Tung et al. (2003), which is not included in the Mann spectral model description.

The spectral tensor of Paper D depends on the same input parameters as the Mann (1994) tensor, except that it uses a slightly modified definition of $\Gamma$, and to avoid confusion the new variant is instead denoted $G$. In the paper, the relationship between the input parameters $L_M$ and $G$ and the physical properties $\epsilon$, $u_*$ and $\frac{\partial U_1}{\partial z}$ is investigated. A key result of this investigation is the left-hand graph of Figure 2.9, which shows the relationship between $G$ and $M\frac{u_*^2\frac{\partial U_1}{\partial z}}{\alpha_{\mathrm{K}}^{3/(2)}\epsilon}$. The latter quantity can be interpreted as the ratio between the turbulent energy production from the shear gradient, $u_*^2\frac{\partial U_1}{\partial z}$, and the dissipation of kinetic energy, $\epsilon$, times a constant $M\alpha_{\mathrm{K}}^{-\frac{3}{2}}$. After $G$ has been determined, $L_M$ is given explicitly. In the right-hand graph of Figure 2.9, $L_M$ is related to the mixing length, $l_{\mathrm{mix}}$. This result can be compared to the empirical investigation of the relationship between $L_M$ and $l_{\mathrm{mix}}$ in Peña et al. (2010).

In Paper D, we thus show that values of the input parameters for the spectral tensor(s), $\alpha_{\mathrm{K}}\epsilon^{\frac{2}{3}}$, $L_M$ and $G$, are uniquely determined by $\epsilon$, $u_*$ and $\frac{\partial U_1}{\partial z}$, all being physical properties of the flow. We conclude by noting that if the production of turbulent kinetic energy from the shear gradient, $u_*^2\frac{\partial U_1}{\partial z}$, is assumed to be equal to the dissipation of kinetic energy, $\epsilon$, then we have in Paper D shown that the friction velocity and the mixing length determine the spectral tensor, that is, at least for neutral atmospheric stratification.

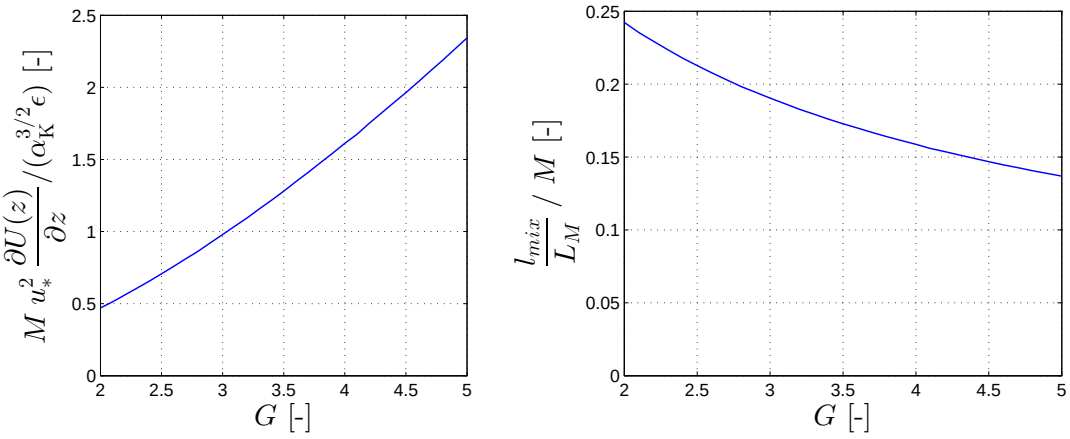


**Figure 2.9:** To the left, $Mu_*^2 \frac{\partial U_1}{\partial z} / \left( \alpha_K^{\frac{3}{2}} \epsilon \right)$ versus G shows that G is uniquely determined by the ratio between the turbulent energy production from the shear gradient and the dissipation or turbulent kinetic energy. The right-hand graph shows that the ratio $\frac{l_{mix}}{L_M}$ depends on $G$ and thereby, also this quantity depends on the ratio between the turbulent energy produced from the shear gradient and the dissipation.

Chapter 3

# Conclusions and Outlook

Wind turbines within offshore wind farms spend considerable time operating in the wake of neighboring wind turbines. An important contribution to the loads on a wake-affected wind turbine is the slow movement of the wake from the upstream wind turbine across the rotor of the wake-affected wind turbine. A new approach to this so called wake meandering is proposed. Beyond the advantage of higher physical realism, the new approach also offers practical advantages, compared to the current state-of-the-art method of simulating meandering within a 3D field of frozen turbulence.

An input to the new meandering approach is the time evolution of the spectral velocity tensor. A spectral tensor, including such features, is therefore developed based on a set of intuitive basic assumptions. For neutral atmospheric stratification, the resulting spectral tensor predicts spatial correlations comparably to the Mann (1994) tensor, and temporal coherence better than any of the models evaluated in Ott and Mann (2005). As part of the framework, a spectral tensor for Lagrangian correlations in space and time is also developed and validated versus measured isotropic turbulence data. Combined, the models reproduce the cross-over point between Eulerian and Lagrangian temporal covariances. This balance between the Eulerian and Lagrangian temporal covariances could be further investigated in order to validate some of the underlying modeling assumptions in more detail.

The values of all input parameters of the spectral tensor are shown to be uniquely determined by the friction velocity, the shear and the dissipation of turbulent kinetic energy, all of them physical properties of the flow. If local equilibrium between the turbulent kinetic energy produced by shear and the turbulent kinetic energy dissipated as heat, is assumed, then, for neutral atmospheric stratification, the friction velocity and the mixing length uniquely determine the spectral tensor. The problem of quantifying all correlations in space and in time (which has a large range of engineering applications) is thus reduced to describing a handful of measurable physical properties as function of observation height.

The developed spectral tensor depends on a dimensionless quantity $M$, and it would be beneficial if this quantity can be determined with higher accuracy. An experiment with this objective, studying the ratio between different components of

the cross-spectra at known shear, is proposed in Paper D. Future work could also include investigating if a Rapid Distortion formulation that also includes a term for buoyancy effects, is needed in order to make accurate predictions for non-neutral atmospheric stratification.

The next logical step would be to update the meandering model of Paper B, making use of one of the spectral tensors of Paper D. If so, simplifications should be considered in the meandering approach, e.g. including the so called *wake transport velocity* in a less complicated way. In Paper C, large scale *quasi-geostrophic* turbulence (Lindborg, 1999; Tung et al., 2003) is observed, and it would be interesting to investigate its contribution to wind turbine wake meandering.

As mentioned in the introduction the spectral tensor can be applied in the context of lidar assisted feed forward control of wind turbines, as it quantifies the correlation between the fluctuations measured at a distance and the turbulence that reaches the rotor plane. The spectral tensor likely has numerous other applications.

The Lagrangian spectral tensor was a late discovery in the project, and it can be investigated and validated to a larger extent. Presumably it also has applications in the fields of dispersion and mixing.

# Bibliography


Bingöl, F., Mann, J., and Larsen, G. C. (2010). Light detection and ranging measurements of wake dynamics part I: one-dimensional scanning. *Wind Energy*, 13(1):51–61.

Bossanyi, E. (2013). Un-freezing the turbulence: application to LiDAR-assisted wind turbine control. *IET Renewable Power Generation*, 7(4):321–329.

Bossanyi, E., Savini, B., Iribas, M., Hau, M., Fischer, B., Schlipf, D., van Engelen, T., Rossetti, M., and Carcangiu, C. E. (2012). Advanced controller research for multi-MW wind turbines in the UPWIND project. *Wind Energy*, 15(1):119–145.

Chougule, A. S. (2013). *Influence of atmospheric stability on the spatial structure of turbulence*. DTU Wind Energy PhD-0028 (EN).

España, G., Aubrun, S., Loyer, S., and Devinant, P. (2012). Wind tunnel study of the wake meandering downstream of a modelled wind turbine as an effect of large scale turbulent eddies. *Journal of Wind Engineering and Industrial Aerodynamics*, 101:24–33.

Fung, J. C. H., Hunt, J. C. R., Malik, N. A., and Perkins, R. J. (1992). Kinematic simulation of homogeneous turbulence by unsteady random Fourier modes. *Journal of Fluid Mechanics*, 236:281–318.

Hunt, J. C. R., Wray, A. A., and Buell, J. C. (1987). Big whorls carry little whorls. *Res. Proc. of 1987 Summer Program,CTR-S87. N.A.S.A. Centre for Turb. Res.*

Isserlis, L. (1916). On Certain Probable Errors and Correlation Coefficients of Multiple Frequency Distributions with Skew Regression. *Biometrika*, 11(3):185–190.

Keck, R.-E. (2013). *A consistent turbulence formulation for the dynamic wake meandering model in the atmospheric boundary layer*, volume 0012. DTU Vindenergi.

Keck, R.-E., Mikkelsen, R., Troldborg, N., de Maré, M., and Hansen, K. S. (2014). Synthetic atmospheric turbulence and wind shear in large eddy simulations of wind turbine wakes. *Wind Energy*, 17(8):1247–1267.

Kristensen, L. (1979). On longitudinal spectral coherence. *Boundary-Layer Meteorology*, 16(2):145–153.

Larsen, G. C., Madsen, H. A., Thomsen, K., and Larsen, T. J. (2008). Wake meandering: a pragmatic approach. *Wind Energy*, 11(4):377–395.

Lindborg, E. (1999). Can the atmospheric kinetic energy spectrum be explained by two-dimensional turbulence? *Journal of Fluid Mechanics*, 388:259–288.

Machefaux, E., Larsen, G. C., Troldborg, N., Gaunaa, M., and Rettenmeier, A. (2014). Empirical modeling of single-wake advection and expansion using full-scale pulsed lidar-based measurements. *Wind Energy*.

Madsen, H. A., Larsen, G. C., Larsen, T. J., Troldborg, N., and Mikkelsen, R. (2010). Calibration and Validation of the Dynamic Wake Meandering Model for Implementation in an Aeroelastic Code. *Journal of Solar Energy Engineering*, 132(4):41014.

Mann, J. (1994). The spatial structure of neutral atmospheric surface-layer turbulence. *Journal of Fluid Mechanics*, 273:141–168.

Mann, J. (1998). Wind field simulation. *Probabilistic Engineering Mechanics*, 13(4):269–282.

Mikkelsen, T., Angelou, N., Hansen, K., Sjöholm, M., Harris, M., Slinger, C., Hadley, P., Scullion, R., Ellis, G., and Vives, G. (2013). A spinner-integrated wind lidar for enhanced wind turbine control. *Wind Energy*, 16(4):625–643.

Moffatt, K. (1967). Interaction of turbulence with strong wind shear. *Atmosphere Turbulence and Radio Wave Propagation*, (Ed. A.M. Yaglom & V.I. Tatarski, (Nauka, Moscow)):139–156.

Monin, A. S. and Obukhov, A. M. (1959). Basic laws of turbulent mixing in the surface layer of the atmosphere. 24(151):163–187.

Ott, S. and Mann, J. (2005). An experimental test of Corrsin's conjecture and some related ideas. *New Journal of Physics*, 7(1):142.

Pao, L. Y. and Johnson, K. E. (2011). Control of wind turbines. *Control Systems, IEEE*, 31(2):44–62.

Peña, A., Gryning, S.-E., and Mann, J. (2010). On the length-scale of the wind profile. *Quarterly Journal of the Royal Meteorological Society*, 136(653):2119–2131.

Saffman, P. G. (1963). An approximate calculation of the Lagrangian autocorrelation coefficient for stationary homogeneous turbulence. *Applied Scientific Research, Section A*, 11(3):245–255.

Sanderse, B. (2009). Aerodynamics of wind turbine wakes. *Energy Research Center of the Netherlands (ECN), ECN-E–09-016, Petten, The Netherlands, Tech. Rep*.

Sathe, A. and Mann, J. (2013). A review of turbulence measurements using ground-based wind lidars. *Atmospheric Measurement Techniques*, 6(11):3147–3167.

Schlipf, D., Cheng, P. W., and Mann, J. (2013). Model of the Correlation between Lidar Systems and Wind Turbines for Lidar-Assisted Control. *JAOT*, 30:2233.

Stull, R. B. (1988). *An introduction to boundary layer Meteorology*. Kluwer Academic Publishers.

Tennekes, H. and Lumley, J. L. (1972). *A First Course in Turbulence*. MIT–press.

Townsend, A. A. (1976). *The Structure of Turbulent Shear Flow*. Cambridge University Press, 2nd edition.

Troldborg, N. (2009). *Actuator Line Modeling of Wind Turbine Wakes PhD thesis*. Ph.D. thesis.

Tung, K. K., Orlando, W. W., and Welch, T. (2003). On the differences between 2D and QG turbulence. *Discrete and continous dynamical systems - Series B*, 3(2):145–162.

Wilczek, M. and Narita, Y. (2012). Wave-number–frequency spectrum for turbulence from a random sweeping hypothesis with mean flow. *Physical Review E*, 86(6):066308.

Wyngaard, J. C. (2010). *Turbulence in the Atmosphere*. Cambridge University Press.

Yeung, P. K. (2002). Lagrangian investigations of turbulence. *Ann. Rev. Fluid Dyn.*, 34:115–142.

# Appendix

Here our objective is to explore the consequences of setting

$$\widehat{R}_{ij}^{iso}(\mathbf{k},\tau) = \widehat{R}_{ij}^{iso}(\mathbf{k},0)e^{-\frac{1}{2}a^2\langle u_1 u_1\rangle|k|^2\tau^2}. \tag{1}$$

It turns out that we can show that, for high Reynolds number flows, $a$ approaches 1 in the inertial sub-range.

In the inertial subrange of high Reynolds number flows, viscosity should have negligible direct effect. We can then make the simplification of removing the viscous term from the Navier-Stokes equations, which lands us with the Euler equations:

$$\frac{\partial\tilde{u}_i(\boldsymbol{x},t)}{\partial t} + \tilde{u}_j(\boldsymbol{x},t)\frac{\partial\tilde{u}_i(\boldsymbol{x},t)}{\partial x_j} = -\frac{\partial p(\boldsymbol{x},t)}{\partial x_i} \tag{2}$$

$$\frac{\partial\tilde{u}_i(\boldsymbol{x},t)}{\partial x_i} = 0. \tag{3}$$

Inserting $\tilde{\boldsymbol{u}}(\boldsymbol{x},t) = (x_3\frac{\partial U_1}{\partial z},0,0) + \boldsymbol{u}(\boldsymbol{x},t)$ for $\frac{\partial U_1}{\partial z} = 0$ into (2) and using (3) yields

$$\frac{\partial u_i(\boldsymbol{x},t)}{\partial t} + \frac{\partial\left(u_i(\boldsymbol{x},t)u_j(\boldsymbol{x},t)\right)}{\partial x_j} = -\frac{\partial p(\boldsymbol{x},t)}{\partial x_i}\cdot\cdot \tag{4}$$

As in Paper D, we will avoid the Fourier-Stieljes representation, and instead use the more intuitive (but less stringent) notation

$$\boldsymbol{u}(\boldsymbol{x},t) = \iiint \widehat{\boldsymbol{u}}(\boldsymbol{k},t)e^{\mathrm{i}\,\boldsymbol{k}\cdot\boldsymbol{x}}\mathrm{d}^3\boldsymbol{k}. \tag{5}$$

for the Fourier transform of the wind field.

Inserting (5) into (4) gives us

$$\frac{\partial \widehat{u}_i(\boldsymbol{k},t)}{\partial t} = -\,\mathrm{i}\,k_j \iiint \widehat{u}_i(\boldsymbol{\kappa},t)\overline{\widehat{u}_j(\boldsymbol{k}-\boldsymbol{\kappa},t)}\mathrm{d}^3\boldsymbol{\kappa} - \mathrm{i}\,k_i\hat{p}(\boldsymbol{k},t), \tag{6}$$

where $\hat{p}(\boldsymbol{k},t)$ has been introduced such that $p(\boldsymbol{x},t) = \iiint \hat{p}(\boldsymbol{k},t)e^{\mathrm{i}\,\boldsymbol{k}\cdot\boldsymbol{x}}\mathrm{d}^3\boldsymbol{k}$.

We now limit the analysis to a specific wave number, $\boldsymbol{k}_1 = (k_1,0,0)$, within the inertial subrange, for which we study only the second velocity component, i.e. $i = 2$, which means that the pressure term disappears, since $k_2 = 0$. If we then multiply both sides by their respective complex conjugates, we get

$$\begin{aligned}\left\langle \frac{\partial \widehat{u}_2(\boldsymbol{k}_1,t)}{\partial t}\overline{\frac{\partial \widehat{u}_2(\boldsymbol{k}_1,t)}{\partial t}} \right\rangle = \Bigg\langle \mathrm{i}\,k_1 \iiint \widehat{u}_2(\boldsymbol{\kappa},t)\overline{\widehat{u}_1(\boldsymbol{k}_1-\boldsymbol{\kappa},t)}\mathrm{d}^3\boldsymbol{\kappa} \\ \overline{\mathrm{i}\,k_1 \iiint_{\boldsymbol{\zeta}} \left(\widehat{u}_2(\boldsymbol{\zeta},t)\overline{\widehat{u}_1(\boldsymbol{k}_1-\boldsymbol{\zeta},t)}\right)\mathrm{d}^3\boldsymbol{\zeta}}\Bigg\rangle \\ = \Bigg\langle k_1^2 \iiint \iiint \widehat{u}_2(\boldsymbol{\kappa},t)\overline{\widehat{u}_1(\boldsymbol{k}_1-\boldsymbol{\kappa},t)} \\ \overline{\widehat{u}_2(\boldsymbol{\zeta},t)}\widehat{u}_1(\boldsymbol{k}_1-\boldsymbol{\zeta},t)\mathrm{d}^3\boldsymbol{\zeta}\,\mathrm{d}^3\boldsymbol{\kappa}\Bigg\rangle .\end{aligned} \tag{7}$$

We are working under the assumption that the turbulence field is homogeneous, which means that all statistics should be invariant under translation. For the integrand of right-hand side of (7), this implies that

$$\begin{aligned}&\left\langle \widehat{u}_2(\boldsymbol{\kappa},t)\,\overline{\widehat{u}_1(\boldsymbol{k}_1-\boldsymbol{\kappa},t)}\,\overline{\widehat{u}_2(\boldsymbol{\zeta},t)}\,\widehat{u}_1(\boldsymbol{k}_1-\boldsymbol{\zeta},t)\right\rangle \\ &= \Big\langle e^{-\mathrm{i}\,\boldsymbol{\kappa}\cdot\boldsymbol{r}}\,\widehat{u}_2(\boldsymbol{\kappa},t)\,e^{\mathrm{i}(\boldsymbol{k}_1-\boldsymbol{\kappa})\cdot\boldsymbol{r}}\,\overline{\widehat{u}_1(\boldsymbol{k}_1-\boldsymbol{\kappa},t)} \\ &\qquad e^{\mathrm{i}\,\boldsymbol{\zeta}\cdot\boldsymbol{r}}\,\overline{\widehat{u}_2(\boldsymbol{\zeta},t)}\,e^{-\mathrm{i}(\boldsymbol{k}_1-\boldsymbol{\zeta})\cdot\boldsymbol{r}}\,\widehat{u}_1(\boldsymbol{k}_1-\boldsymbol{\zeta},t)\Big\rangle \\ &= \left\langle \widehat{u}_2(\boldsymbol{\kappa},t)\,\overline{\widehat{u}_1(\boldsymbol{k}_1-\boldsymbol{\kappa},t)}\,\overline{\widehat{u}_2(\boldsymbol{\zeta},t)}\,\widehat{u}_1(\boldsymbol{k}_1-\boldsymbol{\zeta},t)\right\rangle e^{\mathrm{i}(2\boldsymbol{\zeta}-2\boldsymbol{\kappa})\cdot\boldsymbol{r}}\end{aligned} \tag{8}$$

is true for an arbitrary $\boldsymbol{r}$. This means that both sides of (8) has to be zero for $\boldsymbol{\zeta} \neq \boldsymbol{\kappa}$. Multiplying both sides of (7) by $\mathrm{d}^3\boldsymbol{k} = \mathrm{d}k_1\mathrm{d}k_2\mathrm{d}k_1$ and applying (8) we get

$$\begin{aligned}\left\langle \mathrm{d}^3\boldsymbol{k}\frac{\partial \widehat{u}_2(\boldsymbol{k}_1,t)}{\partial t}\overline{\frac{\partial \widehat{u}_2(\boldsymbol{k}_1,t)}{\partial t}} \right\rangle = \Bigg\langle \mathrm{d}^3\boldsymbol{k}\,k_1^2 \iiint \iiint \widehat{u}_2(\boldsymbol{\kappa},t)\overline{\widehat{u}_1(\boldsymbol{k}_1-\boldsymbol{\kappa},t)} \\ \overline{\widehat{u}_2(\boldsymbol{\zeta},t)}\widehat{u}_1(\boldsymbol{k}_1-\boldsymbol{\zeta},t)\mathrm{d}^3\boldsymbol{\zeta}\,\mathrm{d}^3\boldsymbol{\kappa}\Bigg\rangle \\ = k_1^2 \iiint \left\langle \left(\mathrm{d}^3\boldsymbol{\kappa}\right)^2 |\widehat{u}_2(\boldsymbol{\kappa},t)|^2\,|\widehat{u}_1(\boldsymbol{k}_1-\boldsymbol{\kappa},t)|^2\right\rangle \mathrm{d}^3\boldsymbol{\kappa} \\ = k_1^2 \iiint \widehat{R}_{22}(\boldsymbol{\kappa},0)\widehat{R}_{11}(\boldsymbol{k}_1-\boldsymbol{\kappa},0)\mathrm{d}^3\boldsymbol{\kappa},\end{aligned} \tag{9}$$

where in the last step we have assumed

$$\mathrm{Cov}\big(|\widehat{u}_2(\boldsymbol{k},t)|^2, |\widehat{u}_1(\boldsymbol{\kappa},t)|^2\big) = 0 \tag{10}$$

for $\boldsymbol{k} \neq \pm\boldsymbol{\kappa}$. This assumption seems reasonable to make, since there is no reason to be believe that $|\widehat{u}_2|^2$ and $|\widehat{u}_1|^2$ are correlated for different wave numbers, when $\widehat{u}_2$ and $\widehat{u}_1$, due to homogeneity, are not. We note, however, that we can alternatively show the last step of (9) by assuming that the Fourier components of the wind field are jointly Gaussian and then applying Isserlis' Theorem (Isserlis, 1916).

Regarding the left-hand side of (9)

$$\begin{aligned}\left\langle \mathrm{d}^3\boldsymbol{k}\frac{\partial\widehat{u}_2(\boldsymbol{k}_1,t)}{\partial t}\overline{\frac{\partial\widehat{u}_2(\boldsymbol{k}_1,t)}{\partial t}}\right\rangle &= -\frac{\partial^2\widehat{R}_{22}(\boldsymbol{k}_3,0)}{\partial\tau^2} \\ &= k_1^2a^2\langle u_1u_1\rangle\,\widehat{R}_{22}(\boldsymbol{k}_1,0).\end{aligned} \tag{11}$$

where in the last step, we have inserted (1). Combining (11) with (9) and isolating $a^2$ gives us

$$\begin{aligned}a^2 &= \frac{\iiint \widehat{R}_{22}(\boldsymbol{\kappa},0)\widehat{R}_{11}(\boldsymbol{k}_1-\boldsymbol{\kappa},0)\mathrm{d}^3\boldsymbol{\kappa}}{\widehat{R}_{22}(\boldsymbol{k}_1,0)\langle u_1u_1\rangle} \\ &\approx \frac{\widehat{R}_{22}(\boldsymbol{k}_1,0)\iiint \widehat{R}_{11}(\boldsymbol{\kappa},0)\mathrm{d}^3\boldsymbol{\kappa} + \widehat{R}_{11}(\boldsymbol{k}_1,0)\iiint \widehat{R}_{22}(\boldsymbol{\kappa},0)\mathrm{d}^3\boldsymbol{\kappa}}{\widehat{R}_{22}(\boldsymbol{k}_1,0)\iiint \widehat{R}_{11}(\boldsymbol{\kappa},0)\mathrm{d}^3\boldsymbol{\kappa}} \\ &= 1.\end{aligned} \tag{12}$$

In the approximation step of (12) we have, in the numerator, used the fact that outside the energy containing range $\widehat{R}_{ij}(\boldsymbol{k},0)$ is both slowly varying and very small, and in the last step, we have used $\widehat{R}_{11}(\boldsymbol{k}_1,0) = 0$ owing to incompressibility.

# Paper A

**On atmospheric stability in the dynamic wake meandering model**

Rolf-Erik Keck, Martin de Maré, Matthew J. Churchfield, Sang Lee, Gunner Larsen and Helge Aagaard Madsen

*Wind Energy, Volume 17, Issue 11, pp 1689–1710, Nov 2014*

# On Atmospheric Stability in the Dynamic Wake Meandering Model

Rolf-Erik Keck[1,2], Martin de Maré[1,2], Matthew J. Churchfield[3], Sang Lee[3], Gunner Larsen[2] and Helge Aagaard Madsen[2]

[1] Rotor Systems, Vestas Wind Systems A/S, DK-4000 Roskilde, Denmark
[2] Wind Energy Department, Risø DTU National Laboratory for Sustainable Energy, DK-4000 Roskilde, Denmark
[3] National Renewable Energy Laboratory, 15013 Denver West Parkway, Golden, CO 80401 USA

Corresponding author:
Rolf-Erik Keck – rolf.keck@gmail.com

## Abstract

The present study investigates a new approach for capturing the effects of atmospheric stability on wind turbine wake evolution and wake meandering using the dynamic wake meandering model. The most notable impact of atmospheric stability on the wind is the changes in length and velocity scales of the atmospheric turbulence. The length and velocity scales in the turbulence are largely responsible for the way in which wind turbine wakes meander as they convect downstream. The hypothesis of the present work is that appropriate turbulence scales can be extracted from the oncoming atmospheric turbulence spectra and applied to the dynamic wake meandering model to capture the correct wake meandering behaviour. The ambient turbulence in all stability classes is generated using the Mann turbulence model, where the effects of non-neutral atmospheric stability are approximated by the selection of input parameters.

In order to isolate the effect of atmospheric stability, simulations of neutral and unstable atmospheric boundary layers using large-eddy simulation are performed at the same streamwise turbulence intensity level. The turbulence intensity is kept constant by calibrating the surface roughness in the computational domain. The changes in the turbulent length scales due to the various atmospheric stability states impact the wake meandering characteristics and thus the power generation by the individual turbines.

The proposed method is compared with results from both large-eddy simulation coupled with an actuator line model and field measurements where generally good agreement is found with respect to the velocity, turbulence intensity, and power predictions.

## Introduction

The dynamic wake meandering (DWM) model is a low-fidelity wind turbine wake model which was first developed at Risø DTU in 2003 (Madsen et al. [1, 2] and Larsen et al. [3]). The objective of the DWM model is to capture the large-scale meandering motion of the wake deficit as it convects downstream and predict the resulting wind turbine loads and power production, with a computational cost significantly lower than computational fluid dynamics (CFD). The wake deficit development and its meandering motions have been identified through field observations as the dominant factors in the production of wind turbine fatigue loads. An important observation is that large-scale movements of the wake deficit affect the loads of a wind turbine differently than small-scale turbulence. This implies that describing the wake turbulence with a single turbulence intensity parameter, as in the case of the Frandsen model [4], is not sufficient to accurately account for the effects of wake operations on a wind turbine.

In the DWM model, this effect is captured by assuming a split in turbulence scales in which the small-scales affecting the wake deficit evolution can be treated independently from the large turbulent scales that drive the meandering of the wake. Larsen et al. [3] provide a thorough description of the wake meandering method in the DWM, and propose a "cut-off eddy size," which distinguishes the small-scale turbulence (affecting the wake deficit evolution) from the large-scale turbulence (governing the wake meandering) of two rotor diameters. The meandering approach is validated with measurement data from the Tellus rotor (Bingöl et al. [5] and Trujillo et al. [6]). The wake meandering motion was measured using a LIDAR unit mounted on top of the nacelle.

The wake deficit model implemented in the DWM is based on the work of Ainslie [7, 8]. Ainslie applied a thin shear layer approximation of the Navier-Stokes (N-S) equations in which the turbulent closure is a simple eddy viscosity formulation. This method predicts the mean wake flow behind a wind turbine. Recently, an improved eddy viscosity model was proposed by Keck et al. [9], where a two-dimensional eddy viscosity model was included in the DWM model to better represent the radial distribution of the turbulent energy.

The DWM model also includes an expression to account for wake-added turbulence, turbulence created in the wake shear layer that is in addition to the ambient turbulence. Madsen et al. [10] implemented a wake-added turbulence formulation based on the local depth and the radial gradient of the wake deficit. While this correction well accounts for additional mechanical loads caused by the small-scale turbulence, it is not coupled to the wake deficit evolution and does not affect the development of the wakes of downstream rotors. An alternative method to capture wake-added turbulence is described by Keck et al. [11], where the turbulent stresses in the oncoming wake are used to calculate the wake turbulence intensity level at the next downstream turbine. Furthermore, the wake-added turbulence in this formulation is coupled to the wake deficit evolution at the downstream rotor, allowing for increased turbulence to build-up over a row of wind turbines.

The present work is aimed at developing a model to capture atmospheric stability effects in the DWM model. The impact of atmospheric stability on turbine wake evolution has been shown in the past. Ainslie [7] investigated the effect of atmospheric stability on meandering wakes as early as in the 1980s. However, as pointed out by Barthelmie et al. [12], few current engineering wake models incorporate the effects of atmospheric stability.

The fundamental process of atmospheric stability is well described by Obukhov [13] and Monin and Obukhov [14], in which the buoyancy-induced momentum and heat transfer affect both the turbulent length and velocity scales of the atmospheric boundary layer (ABL). A correction for the effects of stable stratification was proposed by Businger et al. [15]. The effect on ABL shear was later verified experimentally by Kirchhoff and Kaminsky [16]. In later work, a simple model for the effects of atmospheric stability on shear was also proposed by Irvin et al. [17], including a correction for stable stratification by Zoumakis [18].

The effect of atmospheric stability on wake evolution, turbine loads, and power production has become an emerging research topic. A number of studies have documented the influence of the atmospheric stability on turbine loads and power both experimentally (Barthelmie et al. [19], Wharton et al. [20], Schepers et al. [21], and Hansen et al. [22]) and numerically (Sathe et al. [23], Churchfield et al. [24], Lee et al. [25], and Lavely et al. [26]). The physical mechanism of the non-neutral ABL is to enhance (unstable) or dampen (stable) turbulent fluctuations through buoyancy forces. A modified turbulence length scale is another important feature of the non-neutral ABL. Peña et al. [27] showed that modelling atmospheric stability effects by modifying the turbulence intensity alone is not sufficient. Both the shift in length and velocity scale should be explicitly modelled to capture the full effect of the non-neutral atmosphere.

The work presented in this paper is a continuation of the research described by Keck et al. [11]. An important aspect of that article was that a strain-rate contribution from the ABL needs to be included in the wake deficit calculations to accurately model the turbulent stresses in the DWM model. The effect of the strain-rate contribution and the build-up of turbulence over a row of turbines were shown for neutral stratification. The present study will build upon the previous model augmentations to capture the effect of atmospheric stability on the wake dynamics. Since the length and velocity scales of the atmospheric turbulence change as a function of atmospheric stability, the fraction of ambient turbulent energy that affects the wake deficit evolution and the fraction that affects wake meandering, as well as the ABL shear, will change.

The objectives of this work are to:

1. Incorporate the effect of non-neutral stratification on the wake evolution in the DWM model
2. Quantify the effects on the flow field and power production of wake-affected turbines by the proposed correction
3. Validate the atmospheric stability corrected DWM model to reference data.

The article will first give a description of the DWM model as formulated prior to the atmospheric stability effect implementation to serve as baseline in the code frame-work development. This is followed by a brief description of the large-eddy simulation (LES) combined with an actuator line (AL) rotor model used to validate the proposed method. The next sections briefly describe the fundamental physics of the atmospheric stability followed by the formulation of the stability model in DWM. Finally, the result section shows 1) the effect of atmospheric stability on the ambient turbulent spectra, wake meandering, and the power production of wake-affected turbines; 2) the effect of the included atmospheric stability formulation in the DWM model; and 3) a validation of the proposed DWM model to predict the wake evolution in non-neutral atmospheric conditions by comparing the flow field and power production to the LES-AL model and field data from the North Hoyle and OWEZ offshore wind farms.

# Dynamic Wake Meandering model

The baseline version of the DWM model used in this study is based on Madsen et al. [2], but employs the two-dimensional eddy viscosity model proposed by Keck et al. [9] and the wake-added turbulence with a strain-rate contribution from the ABL, also proposed by Keck et al. [11]. The wake meandering applied is based on the same principles as proposed by Larsen et al. [3]; however, a wake transport velocity equal to 80% of the free-stream velocity (as proposed by Keck at al. [28]) is employed rather than using the full free-stream velocity as proposed by Larsen et al. [3].

## Wake deficit module

The wake deficit in the DWM model is governed by the steady state, axisymmetric thin shear layer approximation of the Navier-Stokes (N-S) equations in which momentum is governed by

$$u\frac{\partial u}{\partial x} + v\frac{\partial u}{\partial r} = \frac{1}{r}\frac{\partial}{\partial r}\left(v_T r \frac{\partial u}{\partial r}\right) \quad (1)$$

and continuity is maintained through

$$\frac{1}{r}\frac{\partial}{\partial r}(rv) + \frac{\partial u}{\partial x} = 0 \quad (2)$$

In these equations, the velocity components *u* and *v* are in the mean flow (x) and radial (r) directions, respectively, and $\nu_t$ is the eddy viscosity. The turbulent diffusion is accounted for with an eddy viscosity formulation based on the following mixing length model described in dimensionless from by the equation,

$$\upsilon_T = F_1 k_{amb\ DWM} TI_{amb} + \frac{F_2 k_{2\ DWM} l^{*2} \left|\frac{\partial u}{\partial r}\right|}{U_{amb} R} \quad (3)$$

where $k_{amb\ DWM}$ and $k_{2\ DWM}$ are model constants (the $k_{amb\ DWM}$ constant includes a length scale based on a hub-height equal to *2R*), $TI_{amb}$ and $U_{amb}$ is the ambient turbulence intensity (std(u)/ $U_{amb}$) and mean velocity at hub-height, and *l** is the turbulence mixing length of the wake-added turbulence. $F_1$ and $F_2$ are filter functions that govern the development of turbulent stresses in the absence of a transport equation for turbulence. The details and motivation for this turbulence formulation are provided in Keck et al. [9] and the boundary condition and filter functions applied in this work are descried in Keck et al. [11].

Before applying the eddy viscosity from eq. (3) in eq. (1), it is scaled to include a strain-rate contribution due to the ABL shear, $du/dz_{ABL}$ by eq. (4) and (5).

$$\frac{du}{dr}_{Total} = \begin{cases} \frac{du}{dr}_{DWM} & , \left|\frac{du}{dr}_{DWM}\right| \geq \frac{du}{dz}_{ABL} \\ \frac{du}{dr}_{DWM} + \frac{1}{\pi}\int_{\alpha_1}^{\alpha_2} \left(\frac{du}{dz}_{ABL} \cdot \sin(x)\, dx\right) - (\alpha_2 - \alpha_1)\frac{du}{dr}_{DWM} & , \left|\frac{du}{dr}_{DWM}\right| < \frac{du}{dz}_{ABL} \end{cases} \quad (4)$$

$$\nu_t' = \nu_t \cdot \frac{\frac{du}{dr}_{Total}}{\left|\frac{du}{dr}_{DWM}\right|} \quad (5)$$

where $du/dr_{DWM}$ is the azimuthally average wake velocity gradient in the wake deficit region modelled by the DWM model, $du/dr_{TOTAL}$ is total velocity gradient with the ABL shear contribution included, and $\alpha$ is the angular locations where the effect of the atmospheric shear in cylindrical coordinates is larger than the wake deficit shear. $\alpha_1$ and $\alpha_2$, are found by $arcsin(\frac{du}{dr}_{DWM} / \frac{du}{dz}_{ABL})$ and $\pi$-$\alpha_1$ respectively. The details of this correction can be found in Keck et al. [11]. The equation system described by eqs. (1) - (5) is solved using a finite-difference scheme, in which a second-order central-difference scheme in the radial direction and a first-order upwind scheme in the mean flow direction are applied. As information only moves along the mean flow direction, a solution can be obtained by "marching" downstream, solving each axial position sequentially.

## Turbulence intensity in the deficit module

The wake-added turbulence in the DWM model is used to include the contribution of small-scale turbulence generated by the shear layer in the wake at the downstream turbine. This affects the loads and induction of the downstream turbine; however, the most important effect is the influence on the wake evolution of the wake-receiving turbine. The wake-added turbulence is calculated directly by the turbulent stresses in the wake deficit calculation as

$$TI_{DWM\ MFoR} = \max\left(\sqrt{\frac{1}{c_{u'w'} * (w'_{rms}/u'_{rms})} \cdot \tau_{stress\ DWM}}\ , TI_{amb}\right) \quad (6)$$

where the coefficient $C_{u'w'}$ and the ratio $w'_{rms}/u'_{rms}$ describe the relationship between axial and radial turbulent fluctuations in the wake. These relations are different compared to atmosphere turbulence due to the significantly smaller length scale and the increased degree of anisotropy of wake turbulence. In this work, the correlation coefficient is given the value 0.3, and the ratio $w'_{rms}/u'_{rms}$ is set to unity based on the findings of Larsen et al. [29]. The subscript *MFoR* denotes "meandering frame of reference", i.e., expressed in the reference frame following the centre of the wake deficit and the meandering movements.

### The effect of wake meandering

The DWM deficit module outputs the wind speed and turbulence intensity distribution in MFoR (i.e., without any large-scale movements). The meandering can be viewed as a series of wake segments in which the wake centre has a stochastic offset in lateral and vertical direction according to some statistical distribution. If the distribution of the meandering is known, it is possible to calculate the average wind field and turbulence intensity in the FFoR as the convolution of the deficit in the MFoR (both wind speed and variance, i.e., the square of $TI_{DWM\ MFoR}$ from eq. (6)) and the distribution of the wake centre in the vertical and lateral direction due to wake meandering as follows:

$$\theta_{DWM\ FFoR}(y,z) = \iint \theta(y-y_m, z-z_m)_{DWM\ MFoR} \cdot PDF_m(y_m,z_m)\, dy_m dz_m \quad (7)$$

In this equation, $\theta$ represent the wind speed or variance, $y$-$y_m$ and $z$-$z_m$ are the local coordinates in the MFoR, and $PDF_m$ is the probability density function for the meandering distribution. The subscripts *FFoR* and *MFoR* refer to fixed and meandering frame of reference (i.e., the probability of finding the wake centre at a certain location in a fixed plane perpendicular to the flow direction). The method used to find this meandering distribution is described in the "wake meandering as a function of atmospheric stability" section. The distribution of mean velocity and turbulence intensity in FFoR, given by eq. (7), is used to 1) estimate the "ambient conditions" at downstream rotors to allow for intra-turbine coupling, and 2) find the mean flow field in the simulation domain. For more information see Keck et al. [11].

## Atmospheric stability

Atmospheric stability is related to the vertical distribution of virtual potential temperature, which has an important effect on the turbulence in the atmosphere due to buoyancy effects. Virtual potential temperature is the absolute temperature, with the temperature change due to expansion with altitude and moisture effects removed. In a stable atmosphere, the buoyancy forces suppress the vertical fluctuations, whereas the vertical fluctuations are enhanced in an unstable atmosphere. The neutral condition, in which buoyancy effects have negligible influence on the vertical turbulence, is only experienced a fraction of the time in the atmosphere (see Sathe et al. [23]).

The stability of the atmosphere is dictated by the direction of the heat transfer at the surface. When heat is transferred from the surface upwards this leads to an unstable ABL in which air of higher virtual potential temperature lies under air of virtual lower potential temperature. When the heat flux is directed into the surface, the air becomes cooler near the surface, and the ABL is stable. In simple terms, this can be expressed by saying that when the surface is warmer than the air, an unstable atmosphere will develop and when the surface is cooler than the air, the ABL will be stable (Stull [30]).

The most common measure to characterise atmospheric stability is the Monin-Obukhov length scale (M-O length), see Obukhov [13],

$$L = -\frac{\overline{\theta_v} u_*^3}{\kappa g \left(\overline{w'\theta_v'}\right)_s} \quad (8)$$

where $\theta_v$ is the virtual potential temperature, $\kappa$ is the von Karman coefficient, $g$ is the gravitational constant, and $u_*$ is the friction velocity. The overbar denotes time averaging and the prime symbol ($'$) denotes fluctuation about the mean value. The physical meaning of the M-O length scale is that it is the height above the ground at which the production of turbulent energy due to buoyancy effects is equal to turbulent production due to the strain-rate of the velocity field. It is thus an estimate of the height at which buoyancy effects become important for the turbulence dynamics (Wyngaard [31]). This interpretation of the M-O length shows that numbers of large absolute value indicate near-neutral atmospheric stability, since it indicates that buoyancy-driven turbulence is negligible in a large part of the boundary layer, and numbers of small absolute value represent strong influence of buoyancy. The sign of the length scale indicates the direction of the heat flux and, thereby whether the atmosphere is

stable or unstable. The exact numbers used to characterise the stability classes as a function of M-O length varies between sources. For this investigation, the definition of Peña et al. [27], given in table 1, is used.

*Table 1, the classification of atmospheric stability as a function of Monin-Obukhov length*

| Stability class | very stable | stable | near stable | neutral | Near unstable | unstable | very unstable |
|---|---|---|---|---|---|---|---|
| M-O Length | 10 < L < 50 | 50 < L < 200 | 200 < L < 500 | abs(L) > 500 | -500 < L < -200 | -200 < L < -100 | -100 < L < -50 |

# Mann turbulence model

The Mann turbulence model [32, 33] combines an eddy-lifetime assumption with rapid distortion theory to transform an isotropic spectral tensor to an anisotropic spectral tensor. The anisotropic spectral tensor,$\boldsymbol{\Phi}_{ij}(\boldsymbol{k})$, depends on three input parameters to characterise the turbulence: the product of the spectral Kolmogorov constant and the rate of dissipation to the power of two-thirds ($\alpha\varepsilon^{2/3}$), turbulence length scale ($L_{Mann}$), and degree of anisotropy ($\Gamma$). The Mann turbulence model can be used to generate a three-dimensional box containing random incompressible anisotropic turbulence. In applications it is customary to interpret the streamwise dimension as dependent on time using Taylors frozen turbulence assumption.

The spectral tensor can be used to find the power density spectra of any Reynolds stress component in any direction by spectral integration in the spectral tensor in Fourier space.

$$\boldsymbol{F}_{ij}(k_1) = \int_{-\infty}^{\infty}\int_{-\infty}^{\infty} \boldsymbol{\Phi}_{ij}(\boldsymbol{k})dk_2dk_3 \tag{9}$$

As the spectral tensor itself is the Fourier transform of the (idealised) correlation function of the turbulence, it can also be used directly to calculate statistical properties of the synthetic turbulence by inverse Fourier transform according to the relation,

$$R_{ij}(\boldsymbol{r}) = \int_{-\infty}^{\infty} \boldsymbol{\Phi}_{ij}(\boldsymbol{k})e^{-i\boldsymbol{k}\cdot\boldsymbol{r}}d\boldsymbol{k} = \overline{u_\iota(\boldsymbol{x})u_\iota(\boldsymbol{x}+\boldsymbol{r})} \tag{10}$$

From this it follows that the integral turbulent length scale in any direction can be found by eq. (11).

$$L_i = \int_0^{R_{ii}(r)>0} \frac{R_{ii}(r)}{R_{ii}(0)}dr \tag{11}$$

As indicated by the upper integration limit, the integration should only be carried out over the initial region with positive correlation. The turbulence velocity scale (or friction velocity), $u^*$, can also be obtained by the correlation function using eq. (12), where $R_{13}(\boldsymbol{0})$ is the equivalent to the shear stress $\langle\overline{u'w'}\rangle$.

$$u^* = \sqrt{|R_{13}(\boldsymbol{0})|} \tag{12}$$

The Mann turbulence model is derived to generate atmospheric turbulence in neutral stratification. However, Peña et al. [27] showed that with appropriate parameter selection the Mann model can be used to generate atmospheric turbulence with similar characteristics as non-neutral atmospheric turbulence. By applying the Mann parameters suggested by Peña et al. [27] and using eqs. (9)-(12) it is possible to estimate Reynolds stresses and turbulent length and velocity scales of the atmospheric turbulence in non-neutral atmospheric conditions.

# Incorporating atmospheric stability effects into the DWM model

The eddy viscosity formulation used in the DWM model was not derived to include buoyancy effects due to non-neutral atmospheric stability. The hypothesis of this work is that the effects of atmospheric stability can be emulated in the DWM model by changing the length and velocity scales of the atmospheric turbulence. The characteristic length scale for an unstable atmosphere is larger than for a neutral or stable atmosphere. The effect of this shift in turbulent length scale spectra of the atmospheric turbulence is illustrated in Figure 1. The turbulence, which affects the wake meandering versus the wake deficit evolution, can be separated by applying filter based on the *jinc*-function (Goodman [34], for more details see eq. (15)). It can then be seen that the atmosphere turbulence spectra in an unstable atmosphere (top row) has a smaller portion of energy in the scales affecting the wake deficit evolution (right figures), and a larger portion in the wake meandering scales (middle figures) compared to the stable case (bottom row). The black line included in the left figures shows the *jinc*-function filter.

To illustrate the effect of atmospheric stability on wake simulations with the DWM model, consider the situation in which atmospheric stability is varied while maintaining constant turbulence intensity (where turbulence intensity only accounts for variance in the streamwise flow). The atmospheric turbulence velocity scale ($u^*_{ABL}$) will be approximately constant as a consequence of the constant the turbulence intensity. The turbulence length scale of the atmosphere ($l^*_{ABL}$), however, will vary as a function of atmospheric stability. This will have three important effects on the wake dynamics of the DWM model:

1. The ABL shear that is input to the DWM model deficit equation via eq. (4) would increase with increasing atmospheric stability. Shorter length scales means larger vertical velocity gradients.

$$\frac{du}{dz}_{ABL} \cong \frac{u^*_{ABL}}{l^*_{ABL}} \tag{13}$$

2. The turbulent energy in scales larger than 2D, affecting the wake meandering, decreases with increasing atmospheric stability.

3. For a given turbulence intensity, the amount of energy in scales smaller than 2D, which is assumed to affect the wake deficit evolution, increases with increasing atmospheric stability.

## ABL length and velocity scales as a function of atmospheric stability

By applying the parameters suggested by Peña et al. [27] in the Mann model, the turbulent energy spectra in the non-neutral atmosphere can be approximated. The resulting spectral tensor can be used to estimate the atmospheric turbulent length scale as a function of atmospheric stability using eq. (11). The velocity scale of the atmospheric turbulence can be computed from eq. (12), but as the ambient turbulence intensity is an input parameter to the DWM model, it is more practical to relate the turbulence velocity scale to the turbulence intensity. This is achieved by integrating the energy content of the normal stress in flow direction ($\overline{u'u'}$) and the shear stress (-$\overline{u'w'}$) in the Mann turbulence spectra given by eq. (9). The ratio of the two Reynolds stresses is now a function of atmospheric stability and can be used to calculate the normalized turbulent velocity scale in all atmospheric stability classes from the ambient turbulence intensity using the relation,

$$u^*_{ABL} = \left[\left(TI^2_{AMB}\frac{-\overline{u'w'}}{\overline{u'u'}}\right)\right]^{1/2} \tag{14}$$

The parameters suggested by Peña et al. [27] are given as a function of height, which means that the resulting turbulence scales in the DWM model will be height dependent. In the previous version of the DWM model, the length scale of atmospheric turbulence is not explicitly given, and is invariant with respect to the height of the tower relative to the rotor radius (i.e., the length scale normalized with turbine radius has been assumed to be constant). However, as the length scale of the atmospheric

turbulence needs to be explicitly included in the wake deficit calculation of the DWM model to capture the effect of atmospheric stability, the height dependence on the turbulence length scale may also be incorporated.

Figure 2 shows the dependence of the turbulent velocity scale (left), length scales (middle), and shear (right) of the ABL on height and atmospheric stability at a fixed turbulence intensity. From the figure it can be seen that the turbulence velocity scale, which is related to turbulent shear stress, in the ABL is nearly invariant with both height and atmospheric stability. The fact that the velocity scale is nearly invariant with height is expected, as the turbulent shear stress is nearly constant in the lower part of the boundary layer. However, the fact that the velocity scale in the boundary layer is constant as atmospheric stability is varied is interesting. This requires the shear stress to be invariant with atmospheric stratification. The shear stress can be rewritten as: $-\overline{u'w'} = u'_{RMS}w'_{RMS}C_{u'w'}$, where $u'_{RMS}$ and $w'_{RMS}$ are the standard deviation of the fluctuation velocities in streamwise and vertical direction, and $C_{u'w'}$ is the correlation coefficient between the two fluctuating components. This means that the decrease in vertical turbulence ($w'_{RMS}$) in stable stratification is balanced by the stronger correlation between streamwise and vertical fluctuations ($C_{u'w'}$), which is presumably due to the increased ABL shear.

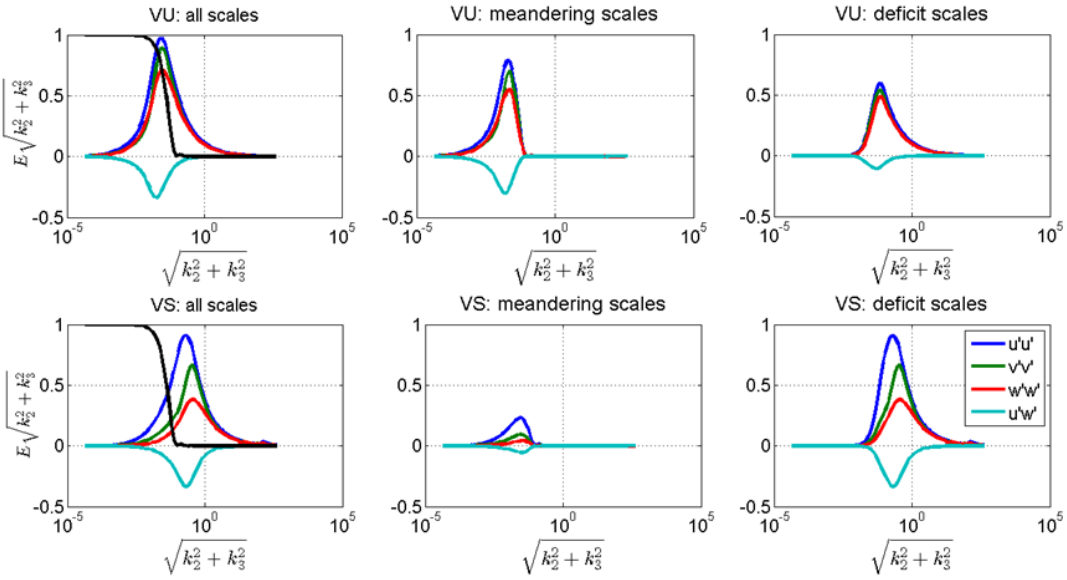


*Figure 1, the turbulent energy spectra for very unstable (top row) and very stable (bottom row) atmospheric conditions derived using the Mann model with the parameters suggested by Peña et al. [27]. The left figures show the turbulent energy spectra in all scales, the middle figures show the turbulent scales which affect the wake meandering, and the right figures show the turbulence which affects the wake deficit evolution. The black line in the right figures show the filter based on the "jinc" function applied to separate the turbulence affecting the wake meandering and the wake deficit evolution.*

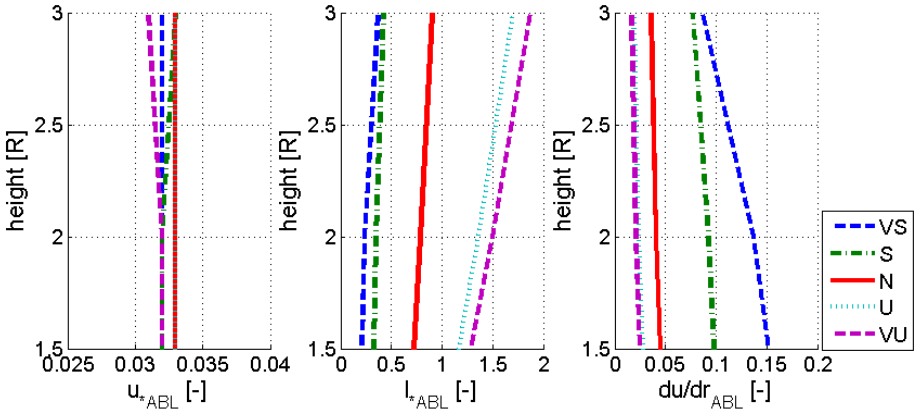


*Figure 2: turbulent velocity scale, length scales, and shear in the ABL as a function of height and atmospheric stability.*

## Wake meandering as a function of atmospheric stability

The wake meandering in the DWM model is calculated based on the turbulent eddies experienced by a circular disc in the oncoming wind field, as described by see Larsen et al. [3]. This approach is motivated by the assumption that the wake acts as a passive tracer in the turbulence field (i.e., the movements of the wake are completely dictated by the large-scale turbulent fluctuations of the oncoming flow). Based on this assumption, the effect of atmospheric stability can be included directly by using the Mann turbulence corrected for non-neutral atmospheric turbulence, as described by Penã et al. [27], as input to the meandering algorithm.

The physical principle used to find the wake meandering is as suggested by Larsen et al. [3], but two modifications to the method are made. The wake transport velocity applied to the meandered wake deficit in the turbulence field is reduced to 80% of free-stream velocity based on the results of Keck et al. [28]. The effect of this modification is shown in Figure 3.

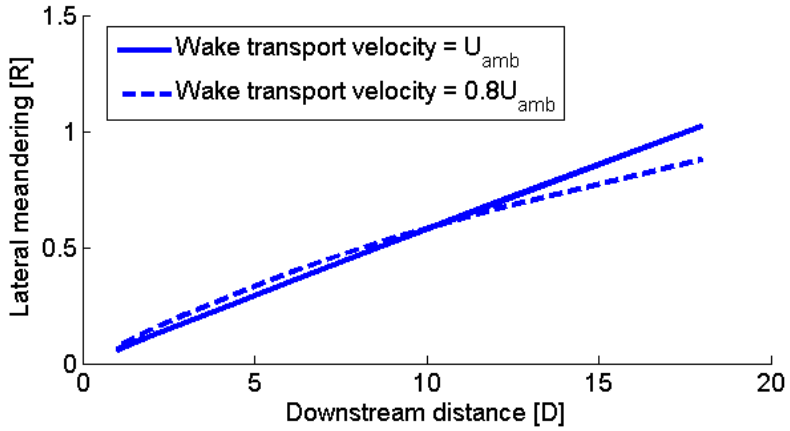


*Figure 3: Wake meandering in the DWM model using a wake transport velocity of 80% (dashed lines) and 100% (solid lines) of the ambient wind speed.*

Furthermore, the computational algorithm used in this work is different. Instead of averaging the wind field over the disc at every time step, as is the current method, a more computationally efficient technique is to “pre-multiply” the wind field with the circular disc to form “the wind field as seen by a circular disc”. This pre-multiplication operation is a convolution and can be carried out as a

multiplication in Fourier space, provided that the wind field and the circular disc have Fourier transforms. As the random wind field is generated in Fourier space and the transform of the circular disc is given by: $2\frac{J_1(|k|R)}{|k|R}$ (Goodman [34]), where $J_1$ is a Bessel function of the first kind, $k$ is the wave number and $R$ is the rotor radius, in this application this is a feasible approach. For wake meandering under the passive tracer assumption, the turbulent wind speed should be averaged over the disc. Assuming that the rotor disc is oriented perpendicular to the x-axis, the filter equivalent to the rotor averaging becomes eq. (15), which as mentioned above is often called the *bessinc* or *jinc* function,

$$jinc\left(\sqrt{k_2^2+k_3^2}\cdot R\right)=\frac{2\cdot J_1\left(\sqrt{k_2^2+k_3^2}\cdot R\right)}{\sqrt{k_2^2+k_3^2}\cdot R} \tag{15}$$

In order to apply eq. (15) to the spectral tensor in the Mann model, the spectral tensor is expressed in polar coordinates ($\sqrt{{k_2}^2+{k_3}^2}$, $\varphi=\arctan(k_2/k_3)$ and $k_1$) and the integration in eq. (9) is performed over the two latter coordinates, resulting in eq. (16).

$$\boldsymbol{F}_{ij}\left(\sqrt{k_2^2+k_3^2}\right)=\int_{-\infty}^{\infty}\int_{-\infty}^{\infty}jinc^2\left(\sqrt{k_2^2+k_3^2}\cdot R\right)\boldsymbol{\Phi}_{ij}(\boldsymbol{k})\cdot\sqrt{{k_2}^2+{k_3}^2}d\varphi\,dk_1 \tag{16}$$

In eq (16), the *jinc*-function is squared as a result of the multiplication of two wind speeds in eq. (10). Note that this squared *jinc*-filter can be applied outside of the integration, and this is the reason for using $\sqrt{k_2^2+k_3^2}$ as the dependent variable, e.g., in figure 2.

The algorithm used in this work to simulate meandering then becomes as follows:

1. Use the Mann turbulence model to generate random Fourier coefficients in three dimensions.
2. Multiply each Fourier component with eq. (15).
3. Wake-segments are released at the wake-emitting turbine at a frequency of 1Hz. The wake-segments travel downstream with a velocity of 80% of the ambient wind speed (based on the findings of Keck et al. [28]), which is referred to as the "wake transport velocity" ($U_{wake}$). The frozen turbulence box travels along the flow with the ambient wind speed. Consequently, the wake deficit travels at a negative speed of -20% of the ambient wind speed relative to the frozen turbulence field.
4. At every time step, the position of each emitted wake-segment is updated based on the fluctuating velocities in the streamwise, lateral and vertical direction, which are calculated based on the current position in the turbulence box. To avoid interpolation as the wake-segments move relative to the turbulence box, which otherwise causes a reduction of turbulent energy, the velocity at the location of the wake-segment is found by applying the definition of inverse Fourier transform (which is continuous and can be used to find the velocity at any location in the field, contrary to the inverse fast Fourier transform (IFFT) to generate turbulent fluctuations in a box of fixed spatial resolution as is commonly done).
5. Finally, when all the wake-segments have reached the desired downstream distance, the wake meandering is scaled by a factor determined by the square root of the ratio of the expected meandering energy to the total captured meandering energy. This ratio is a function of the dimensions of the turbulence box chosen.

Figure 4 shows the wake meandering as a function of atmospheric stability class and height. The wake meandering is quantified as the standard deviation of the wake centre position in lateral and vertical direction normalized by the rotor radius. The dependence on atmospheric stability is dominant compared to that of tower height, with the selected levels.

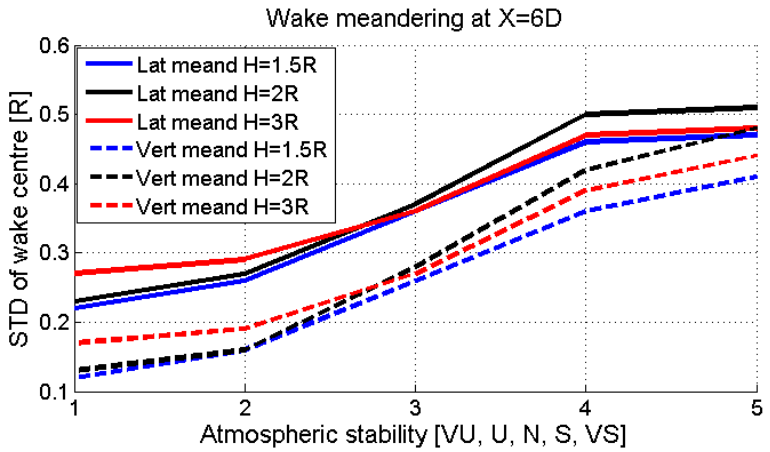


*Figure 4: Wake meandering 6D downstream of the wake-emitting turbine as a function of height and atmospheric stability.*

## Wake deficit evolution as a function of atmospheric stability

Based on the assumption of the "split in scales" in the DWM model, the part of the ambient turbulence that affect the wake meandering is assumed not to influence wake deficit evolution in meandering frame of reference. Therefore the effect of the ambient turbulence on the wake deficit evolution can be calculated by subtracting the energy contributing to the wake meandering. As discussed in the previous section, the meandering process uses a disc-averaged turbulent wind speed. This averaging operation is equivalent to multiplication of the spectral tensor in Fourier space by the filter described by eq. (15). The remaining part of the spectral tensor thus results in the relation,

$$\boldsymbol{\Phi}_{\mathrm{ij}}(\boldsymbol{k})_{\mathrm{DEF}} = \boldsymbol{\Phi}_{\mathrm{ij}}(\boldsymbol{k})\left(1 - jinc^2\left(\sqrt{k_2^2 + k_3^2}\cdot R\right)\right) = \boldsymbol{\Phi}_{\mathrm{ij}}(\boldsymbol{k})\left(1 - \left(\frac{2\cdot J_1\left(\sqrt{k_2^2+k_3^2}\cdot R\right)}{\sqrt{k_2^2+k_3^2}\cdot R}\right)^2\right) \quad (17)$$

The length scale of the wake deficit turbulence can be found by applying the spectra tensor for the wake deficit turbulence, $\boldsymbol{\Phi}_{\mathrm{ij}}(\boldsymbol{k})_{\mathrm{DEF}}$, in eq. (11). The normalized velocity scale of the wake deficit turbulence ($u^*_{DEF}$) is related to the atmospheric stability and the ambient turbulence intensity by the ratio of Reynolds stresses in the "deficit scales", eq. (17).

$$u^*_{DEF} = \left[\left(TI^2_{AMB}\frac{-\overline{u'w'}_{\lambda<2D}}{\overline{u'u'}_{\lambda<2D}}\right)\right]^{1/2} \quad (18)$$

$\lambda$ represents the wavelength of a turbulent eddy. Consequently, the subscript $\lambda<2D$ in eq. (18) indicates that the spectral integration is effectively only carried out over turbulent eddies smaller than 2 rotor diameters, as the rightmost term of eq. (17) removes most of the energy in scales where $\lambda = \frac{2\pi}{\sqrt{k_2^2+k_3^2}} > 2D$. Thus the rightmost term of eq. (17) works as a high pass filter.

The length and velocity scale on the ambient turbulence, including the effect of atmospheric stability, is described by eqs. (11) and (17), and eq. (18), respectively. By applying these expressions into the first term of eq. (3), it is possible to form an expression for eddy viscosity which incorporates stability effects. This is done by explicitly including the turbulent length scale of atmospheric turbulence in the equation (it was previously included in $k_{amb\ DWM}$, i. e. $k_{amb\ DWM} = k_{1\ DWM}\cdot l^*_{DEF}$), and replacing $TI_{amb}$ by $u^*_{DEF}$.

$$v_T = F_1 k_{1\,DWM} u^*_{DEF} l^*_{DEF} + \frac{F_2 k_2 l^{*2} \left|\frac{\partial u}{\partial r}\right|}{U_{amb} R} \quad (19)$$

Note that the new model constant for eddy viscosity due to ambient turbulence ($k_{1\,DWM}$), no longer includes a length scale, and is dimensionless. Instead, the length scale is explicitly given as a function of atmospheric stratification and hub-height.

Figure 5 shows the dependence of the turbulent velocity (left) and turbulent length (middle) scales and of wake deficit turbulence on height and atmospheric stability, together with the eddy viscosity in the DWM deficit evolution that is dependent on the ambient turbulence (right). Similar to the behaviour with the wake meandering, it can be seen that atmospheric stability has a much stronger influence on the eddy viscosity in the wake than tower height, with the selected levels. Furthermore, it can be seen that the eddy viscosity of the wake deficit increases approximately linearly in stable stratification but is close to invariant with height above 1,5R in unstable stratification.

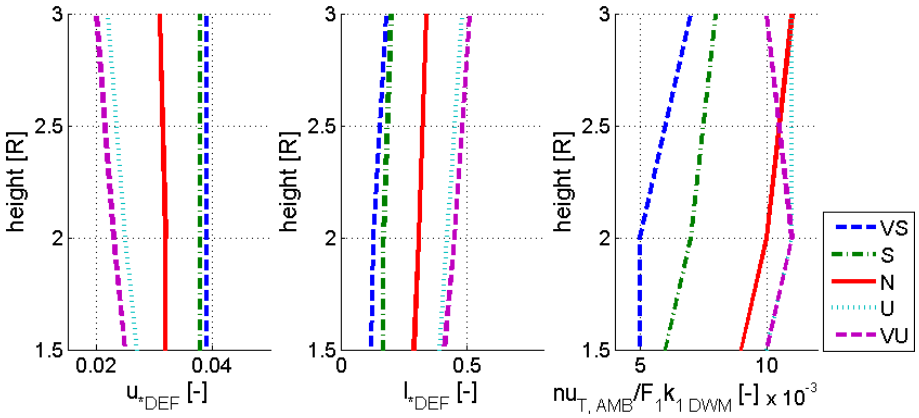


*Figure 5: Turbulent velocity and length scales which affect the wake deficit evolution, together with the eddy viscosity contribution due to ambient turbulence as a function of height and atmospheric stability.*

# Large-Eddy Simulation and Actuator Line Model

Validation of the atmospheric stability effects in the DWM is performed by comparing the turbulence and velocity fields with results from large-eddy simulation (LES) coupled with actuator lines (AL). The LES-AL simulations are performed with tools created at the U.S. National Renewable Energy Laboratory's (NREL) as part of the Simulator for Off/Onshore Wind Farm Applications (SOWFA) [35]. The tools are based on the Open-source Field Operation and Manipulation (OpenFOAM) [36] computational fluid dynamics (CFD) toolbox, which is a collection of libraries, written in object-oriented C++, that is meant to solve complex partial differential equations using the finite-volume formulation. Parallelization is included in these libraries using the Message-Passing Interface (MPI). OpenFOAM comes with a number of standard solvers and libraries for different physical models, such as models for turbulence. The creation of custom solvers and libraries is fairly straightforward because of the highly layered object-oriented nature of the code. The solver used for these LES-AL simulations is a custom OpenFOAM-based solver designed specifically for LES of the atmospheric boundary layer. It is coupled to a custom AL wind turbine model library. A more thorough description is given by Churchfield et al. [24]

## Simulation Process

Simulations were carried out over flat terrain under either neutral or stable conditions. The domain size in each case is 4 km in each horizontal direction and 1 km in the vertical direction. The driving pressure

gradient is adjusted such that the hub-height mean wind is out of the southwest, and a capping inversion is initially placed at 700 m above the surface.

First, a precursor atmospheric boundary layer LES is performed with no turbines on a mesh of uniform 12 m resolution. The lateral boundary conditions are periodic, the top is treated as a stress-free wall, and the surface stress model is applied to the lower surface. Time stepping is such that the local maximum Courant number never exceeds 0.75. Once the simulation reaches a quasi-equilibrium state, in which the mean wind begins to undergo gentle inertial oscillations and turbulence is fully developed up to the top of the boundary layer (which is capped by the capping inversion), the velocity and potential temperature field on the south and west boundaries are saved every time step for 2000 additional seconds. Also, the volume velocity and temperature field are saved once, at the start of quasi-equilibrium. For the neutral and unstable simulations, the quasi-equilibrium state is reached at 16000 s and 14000 s, respectively. The saved boundary and volume data are used as boundary and initial conditions, respectively, for the subsequent wind farm simulation. The surface temperature flux used in the neutral and unstable conditions was 0 and 0.02 K-m/s, respectively, and the surface roughnesses were 0.0003 m and 0.0002 m, respectively. These conditions yielded nearly the same hub height turbulence intensity (based on the variance of flow in the mean wind direction), but significantly different hub height turbulent kinetic energy (based on all three components of the velocity).

Once the precursor simulation is complete, the wind farm simulation is performed. It uses the same overall domain, but regions of local grid refinement down to 1.5 m resolution around the turbines and in their wakes are included to capture the smaller scales generated in the wake. The inflow lateral boundary conditions use the boundary data generated during the precursor stage, and the outflow lateral boundary conditions are set to have a zero normal gradient. The upper boundary is still treated as a stress-free wall, and the lower boundary continues to use Moeng's surface stress model (Moeng [37]). Time stepping is such that the tip of an AL rotor never traverses through more than one grid cell per time step, which is more restrictive than the normal Courant condition, but is required to properly resolve the wake formation. A few hundred seconds are required for the wakes to propagate and for the flow to come to quasi-equilibrium. Once that state is reached, the simulation continues for at least another ten minutes over during which averages and statistics are taken.

## Extracting Meandering from the LES-AL simulations

In the LES-AL simulations, the vertical and horizontal meandering time series are extracted from a vertical and horizontal plane passing through the turbine position, respectively. For each time step and downstream position the best fit between the downstream wind component and a simplified wake shape is calculated. The simplified wake profile used is given by,

$$\text{wake shape}(\mathrm{x},\mathrm{z}) = e^{-\frac{(z-hubheight)^2}{(R/\sqrt{2*\log(2)})^2}} - 2^{-\frac{x}{2R}} \cdot e^{-\frac{(z-hubheight)^2}{(0.1\cdot R/\sqrt{2*\log(2)})^2}} \quad (20)$$

The wake shape depends on both the offset from the centre line, and the downstream distance from the wind turbine and is constructed by two Gaussian distributions. The first Gaussian represents the whole wake deficit and the "*full width at half maximum*" is taken to be 2R. The second term is included to represent the "aerodynamic hole" in the centre of the rotor and is taken to be 0.2R wide. In the far-wake the second term vanished, and the whole assumes a Gaussian shape.

Figure 6 shows the wake meandering found by applying the proposed algorithm. From the figures, it can be seen that the algorithm performs well for the near wake situation (left figures). However, as the wake meandering increase, the wake deficit occasionally meanders outside of the planes where data are collected. An example of this is shown in the right figures of figure 6, where the top figure shows that the wake centre is located between 2-3R off the wake enter axis for a ~50s time-period around 100s into the simulation. In this situation, the wake deficit is difficult to detect in the vertical data plane, and the vertical wake centre position is thus relatively uncertain. As a consequence, cases with more wake

meandering will have higher uncertainty in the meandering statistics by the proposed method. In the figures below, the left set of figures has a lateral standard deviation of the wake centre position of 0.45R, and the right set of figures has a lateral standard deviation of 0.86R. It appears that these kinds of effects which create meandering magnitude uncertainty, begin to occur somewhere between the levels of meandering simulated in this study.

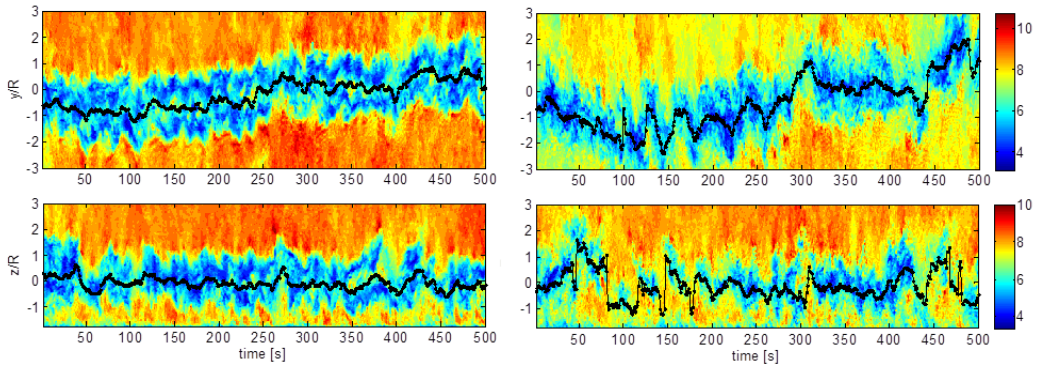


*Figure 6: Horizontal (top row) and vertical (bottom row) wake meandering as a function of time extracted from an AL simulation 3D (left column) and 6D (right column) downstream of the rotor under unstable atmospheric conditions.*

# Description of investigation:

As mentioned above, the overall objectives of the present study are to:

1. Investigate the influence of atmospheric stability on the ambient turbulence characteristics, wake meandering, and the turbulence and wind speed distributions in a wind turbine wake.
2. Develop a method to model the most important effects of non-neutral atmospheric stability in the DWM model.

A complication that occurs when characterizing the effect of atmospheric stability on the ambient turbulence and wake evolution is that atmospheric stability is closely related to the turbulence intensity level. Furthermore, both quantities are known to be positively correlated to the turbulent mixing in the wake, and thereby increase the recovery of the turbine wake. To draw firm conclusions, and to be able to quantify the effect by atmospheric stability, it is therefore desirable to isolate the atmospheric stability from the turbulence intensity. This is difficult to achieve in field observations as the oncoming turbulence intensity is dominantly a function of wind speed, atmospheric stability, and terrain. As a consequence, most previous studies have discussed the effects of atmospheric stability and turbulence intensity together.

In this investigation, the effect of atmospheric stability is isolated by conducting a set of LES-AL simulations in unstable and neutral atmospheres at the same ambient turbulence intensity. (Unfortunately, the flow solver capability for stable atmospheric conditions is not developed yet.) This is achieved by calibrating the surface roughness in the domain for each stability class to yield turbulence intensity close to 6.2%. The simulations are conducted to mimic the conditions along rows of turbines from the offshore wind farms of OWEZ, which consist of 36 V90-3MW turbines, and North Hoyle, which consist of 30 V80-2MW turbines (See table 2).

These sets of simulations allow detailed investigations of atmospheric stability impact on the ambient turbulence spectra and the wake meandering. Unfortunately, the wake deficit evolution cannot be studied independent of the wake meandering, as are performed in Keck et al. [11], since the data required to extract the deficit in meandering frame of reference are not available (such analysis would require the data in planes perpendicular to the mean flow direction). Instead, the effect of atmospheric

stability on the wind speed and turbulence intensity evolution in fixed frame of reference (i.e., both meandering and wake deficit together) is studied.

*Table 2: A list of simulation cases to study the effect of atmospheric stability on ambient turbulence and wind turbine wake evolution. The abbreviations "N" and "U" denote neutral and unstable conditions, respectively, and the abbreviation "N.H" denotes the North-Hoyle wind farm case.*

| Case | Turbine | WS | TI | L | Nr WTG | Spacing |
|---|---|---|---|---|---|---|
| N-N.H. row A | V80 | 8m/s | 6.12% | -∞ | 4 | 11D |
| U-N.H. row A | V80 | 8m/s | 6.16% | -83.6 | 4 | 11D |
| N-N.H. row B | V80 | 8m/s | 6.12% | -∞ | 4 | 10D |
| U-N.H. row B | V80 | 8m/s | 6.16% | -83.6 | 4 | 10D |
| N-N.H. row C | V80 | 8m/s | 6.12% | -∞ | 5 | 4.4D |
| U-N.H. row C | V80 | 8m/s | 6.16% | -83.6 | 5 | 4.4D |
| N-OWEZ row A | V90 | 8m/s | 6.12% | -∞ | 3 | 13D |
| U-OWEZ row A | V90 | 8m/s | 6.16% | -83.6 | 3 | 13D |
| N-OWEZ row B | V90 | 8m/s | 6.12% | -∞ | 3 | 11D |
| U-OWEZ row B | V90 | 8m/s | 6.16% | -83.6 | 3 | 11D |

The second part of the investigation focuses on verifying the effect and accuracy of the proposed atmospheric stability correction for the DWM model. The atmospheric stability correction is evaluated by comparing the result of the baseline DWM model and the modified DWM model to the unsteady AL results in table 2. The accuracy of the DWM model is determined by the standard error (STE) between the mean flow field calculated by the DWM model and the AL reference data in fixed frame of reference (FFoR) using the relation,

$$STE = \sqrt{\left[\frac{1}{n_d}\sum_{d=1}^{n_d}\left(\frac{1}{n_{d,r}}\sum_{r=1}^{n_{d,r}}\left(\theta_{d,r}^{ACL} - \theta_{d,r}^{DWM}\right)^2\right)\right]} \quad (21)$$

The indexes *d*, and *r* correspond to downstream distance and radial position, and θ is the property studied. In this investigation, mean wind speed and turbulence intensity have been evaluated. The STE metric is sensitive to misalignment of the mean wake deficit of the two models as it based on the square difference between the models at each calculation node. This means that misalignment causes increased STE even though the mean level and shape are correct, as shown in figure 7.

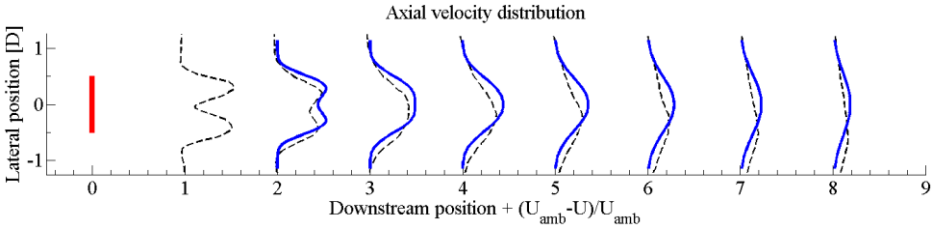


*Figure 7: An illustration of the misalignment of the wake deficit of the DWM model (solid lines) and the AL model (dashed lines) behind the first turbine for the case "U-N.H. row B". This misalignment causes the STE to increase.*

The misalignment mainly occurs as a consequence of the relatively short simulation time, roughly 10 minutes, of the LES-AL calculations. An estimation of the uncertainty due to wake centre misalignment for similar simulations was given in Keck et al. [11], where the uncertainty of the mean flow field based

on 10 min of simulation data in 6% ambient turbulence intensity and neutral conditions was estimated to 0.07m/s and 0.28 percentage points (i.e., *"ΔTI"*, from here on denoted pp) for wind speed and turbulence intensity respectively. As the wake meandering is roughly twice as large in very unstable atmospheric conditions the uncertainties in these cases are about 0.14m/s and 0.56pp.

Another source which contributes to the uncertainty is that the mean velocity at the hub height plane and away from the turbines and wakes in the LES-AL simulations is not uniform for the 10 min time series, as shown in figure 8. Streaks of higher and lower wind speed and turbulence intensity are present in the simulation domain. The uncertainty due to these streaks is estimated based on extracting a standard deviation of mean wind speed and turbulence intensity at hub height on the inflow boundaries. The non-uniform ambient conditions in the domain are estimated to yield an uncertainty of 0.10 m/s and 0.53pp for wind speed and turbulence intensity, respectively, in neutral conditions. The same values in the very unstable conditions are 0.11m/s and 0.71pp.

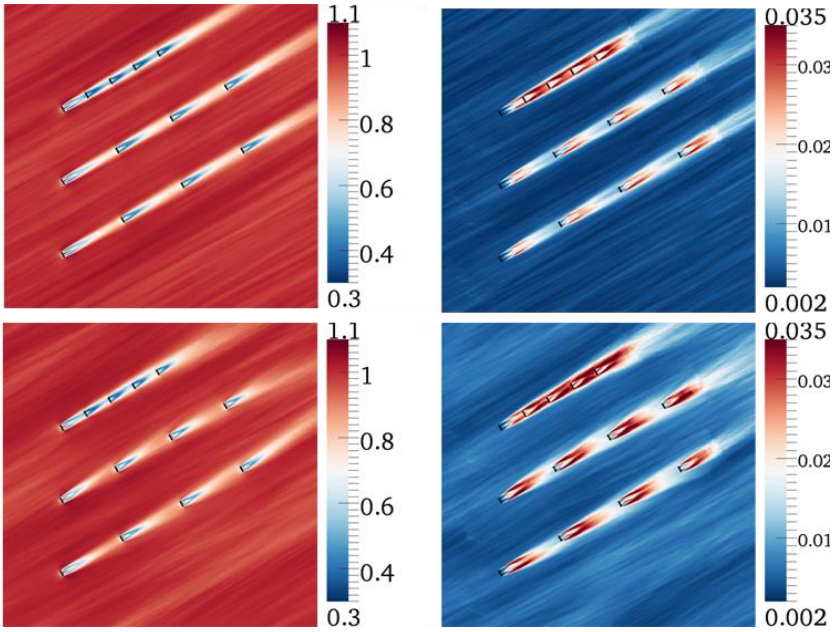


*Figure 8: Contours of mean velocity normalized by hub-height free stream speed (left figures) and resolved-scale turbulent kinetic energy normalized by the square of hub-height free stream speed (right figures) in a horizontal plane at hub height in neutral (top row) and very unstable (bottom row) conditions for the North Hoyle case.*

As the two sources of uncertainty can be assumed to be independent from each other, the combined uncertainty is found, as the root-square-sum, to be 0.12m/s and 0.60pp in neutral conditions and 0.18m/s and 0.92pp in very unstable conditions. When basing the comparison of the models on eq. (21), the uncertainty on the mean flow field increases the STE linearly. This means that if the true model mean profiles were identical, the STE would be equal to uncertainty of the AL simulations.

# Results and discussion:

## Verification of input wind field

The input turbulence fields of the two models are generated by fundamentally different methods. The ABL turbulence of the DWM is estimated using the Mann turbulence model with the input parameters

suggested by Peña et al. [27], whereas the ABL turbulence applied in the LES-AL simulations is created using a precursor LES in which the N-S equations dictate the flow. The turbulent energy spectra of the applied input velocity field are shown in figure 9. The turbulence spectra of the two models in neutral stratification are in fair agreement for all wave numbers above the cut-off frequency of the LES precursor simulation. This cut-off is grid-induced filtering in the LES precursor simulation. For the unstable case, however, the LES model contains more turbulent energy in the large scales of the lateral turbulence spectra, compared to the turbulence applied in the DWM simulation. The higher turbulence levels are seen in the range of $k_1$ 0.002 to 0.006, corresponding to turbulent eddies of 1 to 3km in size. In this range the turbulent energy level of the LES simulations are approximately four times as high as that in the Mann turbulence of the DWM model (although it should be noted that the energy levels fluctuate largely due to the few realizations). The highest energy level in the lateral spectra of LES-AL turbulence is seen at $k_1$= 0.003 (2km). The corresponding number in the Mann spectra turbulence is $k_1$= 0.02 (250m). The findings are consistent with the findings presented by Larsen et al. [38] for using the Mann turbulence model with calibrated input parameters to simulate unstable atmospheric conditions. In the unstable cases, the LES model resolves long lines of updrafts on the scale of 1 to 3 km, which is the range in which the LES turbulence has higher lateral energy than the Mann turbulence.

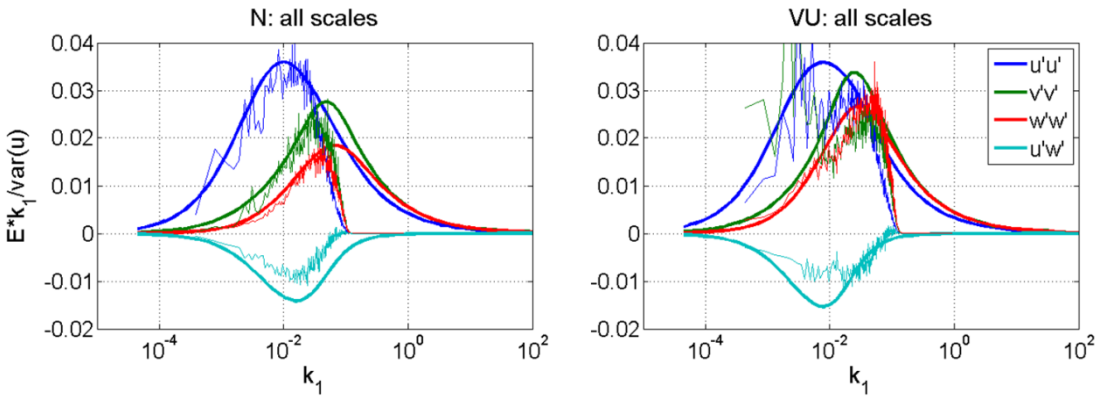


*Figure 9: The turbulence energy spectra of the wind field generated by Mann model (thick lines) and that generated with by precursor LES simulations (thin lines).*

As a consequence of the large length scales in the LES precursor turbulence, the most energy-containing turbulent eddies are only realized 2-3 times during the 10 min simulation time. This results in a high uncertainty in the STE comparison due to the inhomogeneous mean flow field and the alignment of the wake meandering (see figures 7 and 8). Furthermore, as seen in the subsequent analysis, the difference in the input spectra affects the lateral wake meandering for the unstable cases.

The cause of these differences in the lateral input turbulence requires further investigation. To reduce the effect of the discrepancies on the DWM validation, it would be interesting to conduct longer LES-AL simulations to obtain fully converged mean conditions for the comparison. Unfortunately, lengthening these calculations is too computationally expensive for the present study; a simulation to resolve the most energy containing structures ~30 times would require in the order of 5 million CPU-hours per case.

## Validation of wake meandering with the DWM method

Figure 10 shows the lateral (left) and vertical (right) wake meandering as a function of downstream position and atmospheric stability, as calculated by the DWM method (black), the EllipSys3D LES-AL model (red) (data from Keck et al. [28]) and the OpenFOAM LES-AL model. The figure shows that the wake meandering applied in the DWM model is in fair agreement with the two LES-AL data sets for the neutral cases. For the unstable cases, however, the lateral wake meandering of the DWM model is 40%

lower compared to that of the OpenFOAM LES-AL model. This is attributed to the differences in the input spectra, as discussed above and shown in figure 9. The vertical wake meandering and the input spectrum of vertical turbulence seen in figure 9 in the unstable atmosphere of the two models correlate well, which strengthens the conclusion that the deviations in lateral wake meandering are due to the difference in lateral input turbulence.

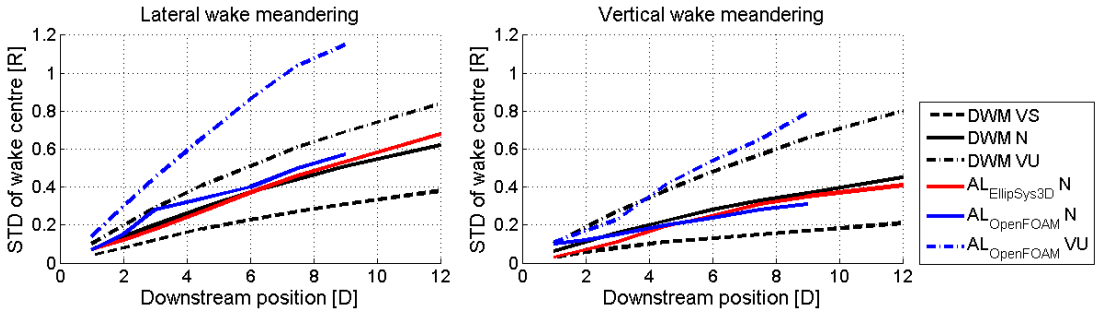


*Figure 10: Wake meandering as calculated by the DWM (black), EllipSys3D LES-AL (red) and OpenFOAM LES-AL models (blue) for a rotor of 80m in diameter and 70m hub height operating in 8m/s wind speed and 6% turbulence intensity. The left figure show the lateral meandering and the right figure show the vertical meandering, both expressed as the standard deviation of the wake centre normalised by R.*

## Effect of the atmospheric stability correction in DWM

This section shows the effect of including the atmospheric stability correction in the DWM model. In the first analysis the STE of all unsteady cases in table 2 are calculated both with the modified (DWM B) and the unmodified (DWM A) versions of the DWM model to verify that the suggested correction increases the ability to predict the flow field under unstable atmospheric conditions, see table 3. By comparing the results it can be concluded that the atmospheric stability correction reduces the average STE by 19% in terms of wind speed and 28% in terms of turbulence intensity

*Table 3: The STE (eq. (21)) of the DWM model without (A) and with (B) the atmospheric stability correction compared to the OpenFOAM LES-AL simulations for the unsteady simulations listed in table 2.*

| | STE WS DWM A [m/s] | STE WS DWM B [m/s] | Ratio B/A | STE TI DWM A [%] | STE TI DWM B [%] | Ratio B/A |
|---|---|---|---|---|---|---|
| N.H. row A | 0.53 | 0.39 | 0.74 | 2.9 | 2.0 | 0.69 |
| N.H. row B | 0.60 | 0.45 | 0.75 | 3.4 | 2.4 | 0.71 |
| N.H. row C | 0.71 | 0.63 | 0.89 | 2.1 | 2.0 | 0.95 |
| OWEZ row A | 0.48 | 0.40 | 0.83 | 2.0 | 1.2 | 0.60 |
| OWEZ row B | 0.52 | 0.43 | 0.83 | 1.7 | 1.1 | 0.65 |
| **Mean** | **0.57** | **0.46** | **0.81** | **2.4** | **1.7** | **0.72** |

To illustrate the effect of the atmospheric stability correction, the velocity and turbulence intensity profiles behind the two first turbines in the *"U-N.H. row A"* case are plotted in figure 11. It can be seen that the velocity deficit of the modified DWM model is more shallow and wider with higher average turbulence intensity.

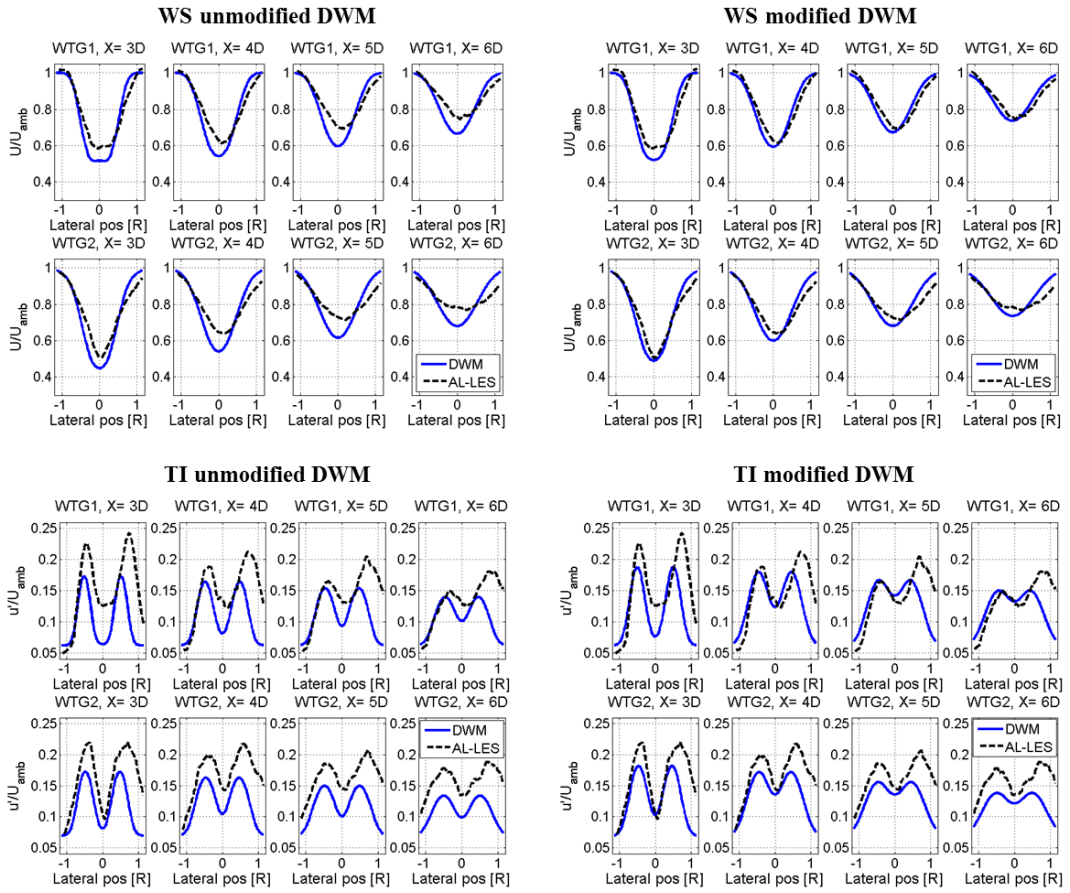


*Figure 11: The velocity (top) and turbulence intensity (bottom) profiles at hub height and 3, 4, 5 and 6D (from left to right) behind the two turbines in the "U-N.H. row A" case. The top row of group depicts the result behind the first turbine and the bottom row show the result behind the second turbine in the row.*

In the second analysis, the modified DWM version is used to investigate the effect on power production in single-wake operations as a function of incoming flow angle and atmospheric stability, as shown in figure 12. The ambient wind speed at hub-height is 8m/s and the turbulence intensity is 6%. The two turbines are located 7D apart. It can be seen that for this configuration the power deficit (one minus the ratio of the mean power of the second to the first turbine) is 45% larger in the very stable atmosphere (0.58) compared to a very unstable atmosphere (0.4) when the incoming flow is aligned with the axis of the two turbines. The difference decreases with increasing inflow angle to the turbines, and at a mean wind direction of $7^{o}$ the power deficit is independent of atmospheric stability. For inflow direction between $7^{o}$ and $15^{o}$ the power deficit is slightly increased in an unstable atmosphere. These effects are predominately governed by the wake meandering. By integrating over-all wind directions in figure 12, the loss of production due to the single wake for a site with a uniform wind distribution can be found. This yields a reduction in annual energy production (AEP) of 1.7%, 1.6%, and 1.4% for very stable, neutral, and very unstable atmosphere, respectively (under the assumption that no power loss is experienced in the $330^{o}$ that are not shown in the figure). The same analysis for a range of atmospheric conditions and turbine spacings is presented in figures 13 and 14.

The amount of increased turbulence intensity level experienced at the downstream turbine is also affected by the atmospheric stability. The wake-added turbulence is a combination of small-scale turbulence generated by the shear layer of the wake and "apparent" turbulence due to the wake meandering. The deeper wake deficit in stable stratification creates more shear layer generated

turbulence, whereas the apparent wake contribution is a combination of the depth of the wake deficit and the amount of wake meandering (see figure 15 to see how the ratio of the two components vary with atmospheric stability). For the case presented in figure 12, the increase in turbulence intensity at the second turbine is 5.4, 4.4, and 3.7 percentage points (pp) for very unstable, neutral and very stable atmosphere, respectively.

The same trends as in the case presented in figure 12 are seen throughout the study:

1. Stable atmospheric conditions causes larger power losses in single wake operations
2. Unstable atmospheric conditions are more turbulent at the second turbine. This is mainly due to a larger "apparent" turbulence contribution.
3. The neutral cases are, on average slightly closer to the very stable cases than the very unstable cases. The average difference for the tested cases is 0.22% in AEP from very stable to neutral and 0.33% from very unstable to neutral stratification.

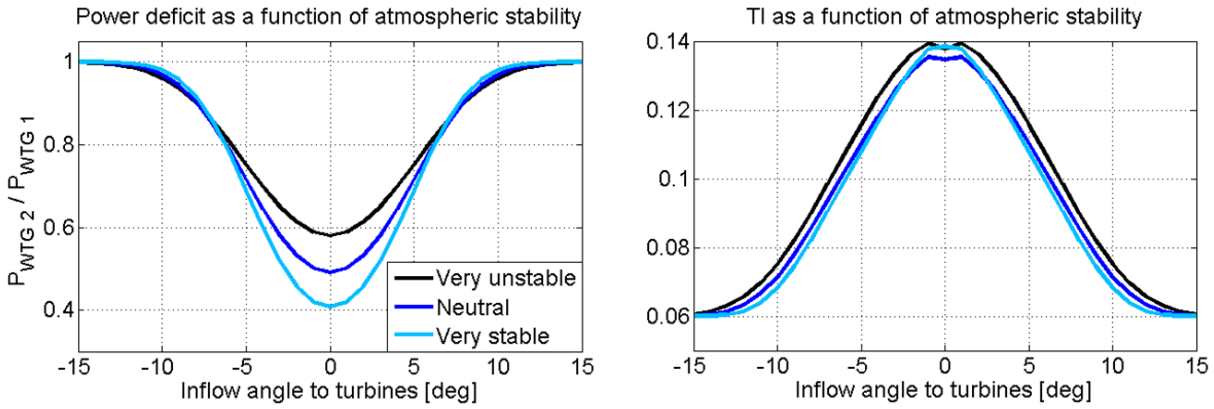


*Figure 12: The power deficit (left) and turbulence intensity profiles (right) as a function of the atmospheric stability and inflow direction at a wake-affected turbine 7D downstream of the wake-emitting turbine.*

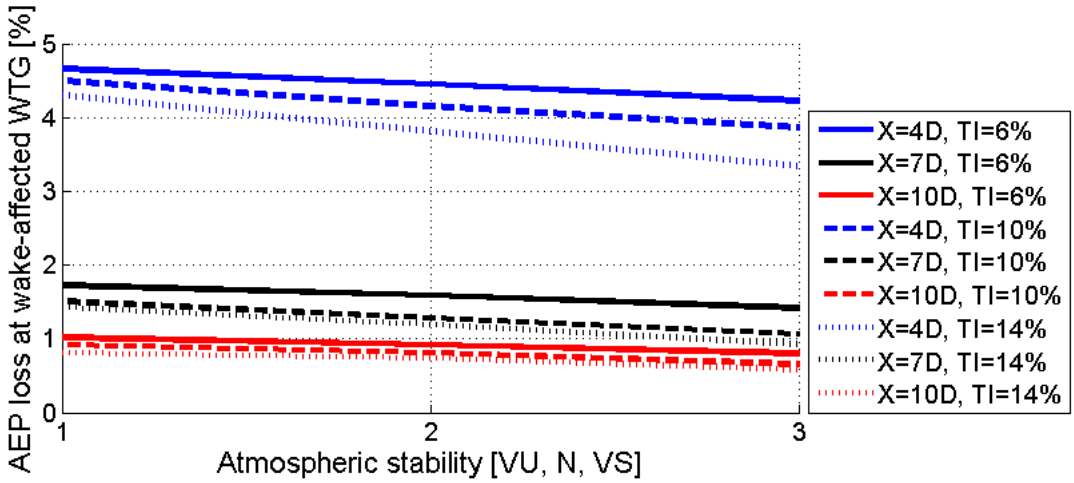


*Figure 13: Loss of AEP in % at the 2nd rotor as a function of distance, turbulence intensity and atmospheric stability in single wake operation. The AEP integration of power is performed over 360°.*

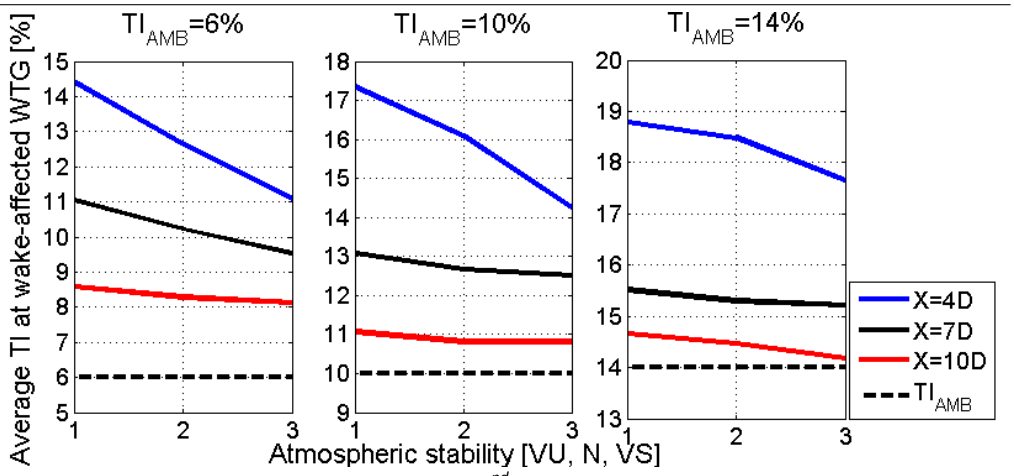


*Figure 14: Average turbulence intensity level at the 2nd rotor as a function of distance, turbulence intensity and atmospheric stability in single wake operation. The turbulence intensity is averaged in a -10° to +10° sector.*

Apart from an increase in the turbulence intensity (shown in figure 12), atmospheric stability also influences the composition of the wake turbulence. Figure 15 shows the composition of the wake turbulence in a cross section 6D downstream of the first turbine. The simulations are conducted in an ambient wind speed of 8 m/s and a turbulence intensity of 6%, under very stable (left), neutral (middle), and very unstable (right) atmospheric conditions. As mentioned above, the total turbulence experienced by a downstream rotor ($TI_{Tot}$) consists of small-scale turbulence ($TI_{Small-scale}$) and the apparent turbulence created by the meandering of the wake deficit ($TI_M$). From the figure it can be seen that the relative contribution to the turbulence intensity due to wake meandering is approximately twice as large in the very unstable case compared to the very stable case. The increased amount of turbulence in meandering scales will affect the fatigue loads of the wake-receiving turbine (see Madsen et al. [1], Sathe et al. [23] and Crespo et al. [39]), whereas the small-scale turbulence will mainly affect the wake deficit evolution of the wake-affected turbine.

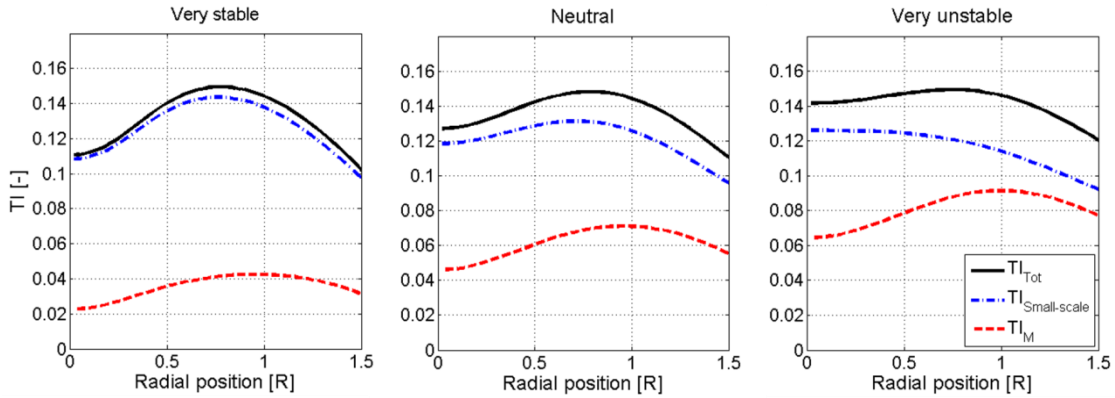


*Figure 15: The composition of turbulence intensity in the wake as a function of atmospheric stability.*

## Wake velocity and turbulence intensity with the modified DWM model

Table 4 show the STE based on wake velocity and turbulence intensity for all the conducted cases. The average STE for the conducted cases under neutral conditions is 0.25 m/s in terms of wind speed and 1.48 pp for turbulence intensity. The average STE for the unstable cases is 0.42 m/s for wind speed and 2.78 pp for turbulence intensity. An explanation for part of this increase in STE for the unsteady cases is the higher degree of uncertainty due to wake meandering and the non-uniform inflow conditions in the

computational domain. As discussed above, the uncertainty in the AL results increase the STE linearly. According to the estimations presented above, the uncertainty of 0.12 m/s and 0.60 pp in neutral conditions and 0.18 m/s and 0.92 pp in very unstable conditions for wind speed and turbulence intensity, respectively, is responsible for 45% of the STE of wind speed and 36% of the STE of turbulence intensity.

*Table 4: The STE (see eq. (21)) of the DWM model with the proposed atmospheric stability correction compared to the conducted AL simulations.*

| Cases: | STE WS [m/s] | STE TI [%] |
|---|---|---|
| N-N.H. row A | 0.31 | 1.6 |
| U-N.H. row A | 0.39 | 2.0 |
| N-N.H. row B | 0.35 | 1.3 |
| U-N.H. row B | 0.45 | 2.4 |
| N-N.H. row C | 0.57 | 2.2 |
| U-N.H. row C | 0.63 | 2.0 |
| N-OWEZ row A | 0.27 | 1.2 |
| U-OWEZ row A | 0.40 | 1.2 |
| N-OWEZ row B | 0.28 | 1.2 |
| U-OWEZ row B | 0.43 | 1.1 |

Figures 16 and 17 show the velocity and turbulence profiles for the *"N-OWEZ row B"* and *"U-N.H. row C"* cases as computed with the DWM and LES-AL. The results show the overall agreement with the range of STE achieved by the DWM model. By observing the *"U-N.H. row C"* case, it can be seen that both the velocity and the turbulence intensity field has the correct shape and good agreement with field data even at the higher STE numbers presented in table 12.

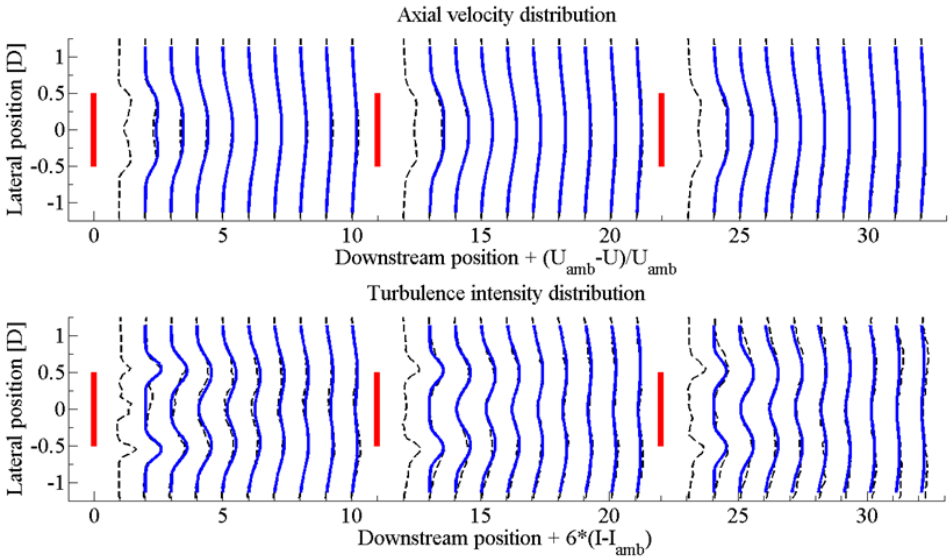


*Figure 16: Comparison of the velocity (top) and turbulence intensity (bottom) profiles for the "N-OWEZ row B" case found with the LES-AL model (dashed lines) and the modified DWM model (solid lines). The thick solid lines show the rotor positions.*

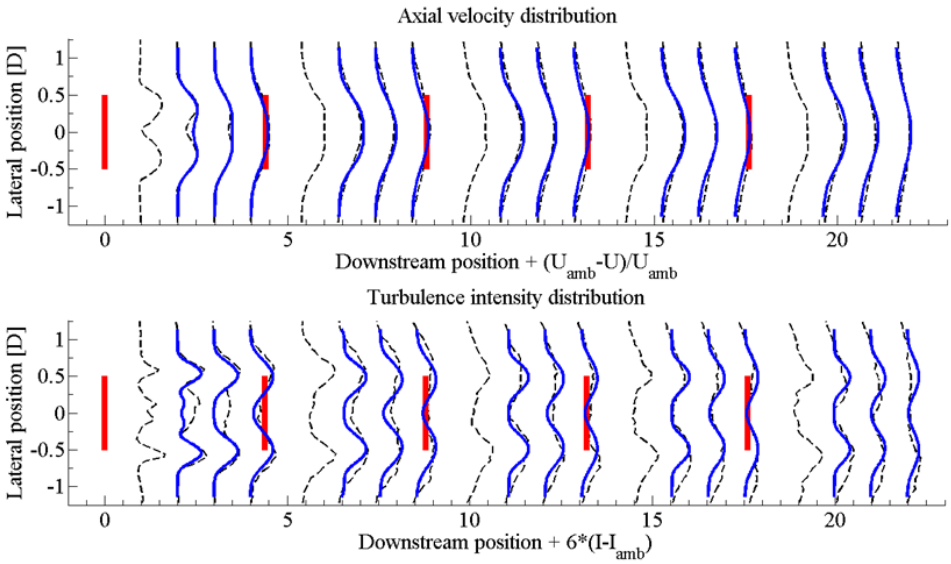


*Figure 17: Comparison of the velocity (top) and turbulence intensity (bottom) profiles for the "U-N.H. row C" case found with the LES-AL model (dashed lines) and the modified DWM model (solid lines). The thick solid lines show the rotor positions.*

## Power production with the modified DWM model

Figure 18 shows a comparison of the power production estimates of the modified DWM model field data from the North Hoyle wind farm. All modelled cases are computed with a hub-height mean wind speed of 8 m/s and turbulence intensity of 6%, which correspond to the mean conditions of the field data. The columns represent very stable, neutral and very unstable conditions from left to right; and the rows represent 11D, 10D, and 4.4D turbine spacing from the top down (i.e., row A to C of in table 4).

The field data in Figure 17 show lower wake losses compared to the numerical results. This may be due to a larger bin size of incoming wind direction. In the DWM model, only wind aligned with the row of turbines is considered.

The main motivation for the study of power production is to verify that the DWM model can capture the average effect on power production due to non-neutral atmospheric stability by implementing the suggested modifications. The average normalized power production of the wake affected turbines for the OWEZ and the North Hoyle wind farm cases are presented together with field data in table 5.

Both the DWM model and the field data show that increasing the atmospheric stability causes larger wake effects in wind farms, even when the turbulence intensity is maintained constant. By comparing the average wake losses in the table, it is seen that the wake losses in very unstable conditions are 10% and 6% smaller compared to neutral stratification for the DWM model and the field data, respectively (however, it should be noted that the power production in neutral atmosphere for the *N.H 10D* case is an outlier and influences the field data result, as seen in table 5; excluding the *N.H 10D* case yields a 13% difference between unstable and neutral atmospheric conditions instead of the current 6%). Comparing the average wake losses in very stable conditions and neutral conditions, the DWM model predicts 12% higher losses and the field data show 13% higher losses.

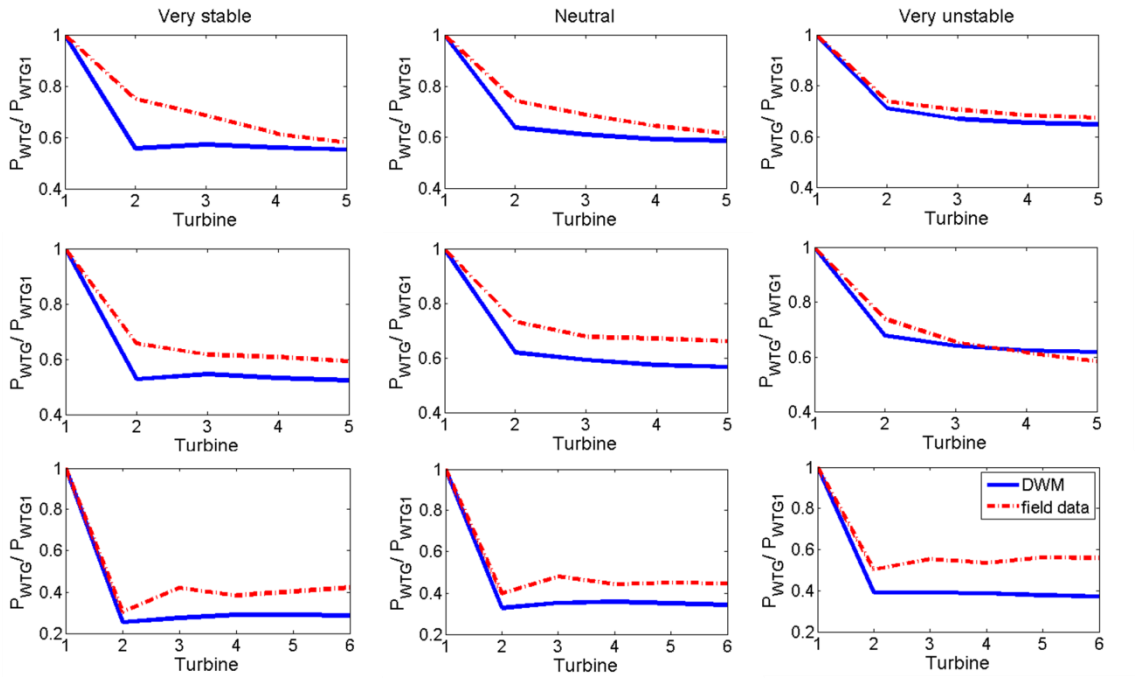


*Figure 18: The power production for all turbines in the rows from the simulation cases at the North Hoyle wind farm compared to field data. The ambient hub-height conditions in all cases are wind speed of 8m/s and a turbulence intensity of 6%. The column represent atmospheric stability class (very stable, neutral and very unstable from left to right) and the rows show different turbine spacing (11, 10 and 4.4D from top to bottom).*

*Table 5: Average power production of all wake affected turbines, normalized against the first turbine of the row, in the North Hoyle and OWEZ simulations compared to field data. The ambient conditions in all cases are wind speed of 8m/s and a turbulence intensity of 6%.*

| | Field data-VS | DWM-VS | Field data-N | DWM-N | Field data-VU | DWM-VU |
|---|---|---|---|---|---|---|
| **OWEZ 11D** | 0.62 | 0.57 | 0.71 | 0.61 | 0.72 | 0.67 |
| **OWEZ 13D** | 0.74 | 0.63 | 0.79 | 0.67 | 0.81 | 0.70 |
| **N.H 4.4D** | 0.39 | 0.28 | 0.44 | 0.35 | 0.54 | 0.38 |
| **N.H 10D** | 0.62 | 0.53 | 0.69 | 0.59 | 0.65 | 0.64 |
| **N.H 11D** | 0.66 | 0.56 | 0.67 | 0.61 | 0.70 | 0.67 |
| **Mean of COL** | 0.61 | 0.51 | 0.66 | 0.57 | 0.68 | 0.61 |

# Conclusions

The present findings show that atmospheric stability influences the wake effects experienced in a wind farm, even when the ambient turbulence intensity (based on wind speed variance in the mean flow direction, as is typically done) is held constant. This suggests that the impact of atmospheric stability on the turbulent length scale is important for wind farm dynamics, and that the turbulence intensity alone is not sufficient to describe wake dynamics in the atmospheric boundary layer. It also suggests that turbulence intensity based on the component of flow in the mean wind direction only is insufficient and

that all three components must be considered. Specifically, the presented data show that atmospheric stability affects the length scale of the atmospheric turbulence, and that this shift in length scale influences both the wake meandering and the wake deficit evolution. Furthermore, it is shown that the effect of atmospheric stability on the AEP of a wind turbine influenced by a single wake (the turbine is only in wake in a $30^{o}$ sector, but the AEP is calculated over $360^{o}$) is in the order of 0.50% comparing very unstable to very stable conditions (this is equivalent to ~25% of the AEP loss due to the wake). Although 0.5% seems small, it can translate into millions of dollars over the lifespan of a large modern wind plant, so having the capability to account for stability on AEP in the DWM model is important. The power produced by a row of wind turbines aligned with the wind direction is reduced by about 10% in very stable conditions compared to very unstable conditions, based on results from both field data and simulations of the North Hoyle and OWEZ wind farms.

The proposed increase in functionality of the DWM model to include the effects of atmospheric stability shows an improved agreement with the reference data sources compared to the baseline model. STE between the AL model and the modified DWM model are reduced by ~19% in terms of velocity field and ~28% in terms of turbulence intensity field on average.

The largest deviations are seen in the generated input turbulence in unstable atmospheric stability, where the turbulence field generated by the Mann model with the parameters suggested by Peña et al. [27] is found to contain less energy in the largest turbulence scales of the lateral component, compared to the LES precursor calculations. These findings are in agreement with the conclusions drawn by Larsen et al [38], where the calibrated Mann model was found to contain less large-scale lateral turbulence in unstable atmospheric conditions compared to field data. For the undertaken study, a consequence of the large length scale of the LES precursor turbulence (which is about 8 times larger than expected from the Mann model in unstable atmosphere) is that the eddies containing the largest amount of energy only pass through the domain a few times during the LES-AL simulations. This will yield an increased uncertainty of the local mean flow field of the LES-AL computations, affecting the STE comparison, and a larger lateral wake meandering in the LES-AL results compared to the DWM results. Suggested further work is to run the LES-AL cases longer to reduce the uncertainty, and to compare the unstable ABL turbulence fields generated by each method in detail. As mentioned above, no reference data is available for stable atmospheric conditions as this functionality is currently not available in the LES model used.

In this investigation, is has not been possible to verify the wake deficit evolution independently of the wake meandering, as is done in Keck et al. [11], as the LES-AL data required to extract the deficit in a meandering frame of reference is not available. Instead, the LES-AL and DWM flow fields in fixed frame of reference (i.e., both the velocity deficit and the wake meandering observed together) are compared. A good agreement is achieved in both magnitude and evolution of downstream profiles of mean velocity and turbulence intensity. The STE in terms of mean velocity is 0.36 m/s in neutral conditions and 0.46 m/s in very unstable conditions; and for turbulence intensity it is 1.50 pp in neutral conditions and 1.74 pp in very unstable conditions. These numbers are also influenced by the uncertainty of the LES-AL results due to the relatively short simulations times, which increase the STE linearly (as the STE is the root-square of the difference in the flow field of the DWM and the AL results). The uncertainties for the simulated cases are 0.12 m/s and 0.60 pp in neutral conditions and 0.18 m/s and 0.92 pp in very unstable conditions for wind speed and turbulence intensity, respectively. The uncertainty accounts for approximately 37% of the STE in terms of wind speed and 46% of turbulence intensity.

The effect of atmospheric stability on the power production of a row of wind turbines agrees well between the DWM model and the field data from the rows of wind turbines at the North Hoyle and OWEZ wind farms. Both show that the very stable stratification leads to about 13% higher wake losses than in neutral conditions and that very unstable conditions lead to about 10% lower wake losses compared to neutral conditions.

# References:


[1] Madsen, H.Aa., Thomsen, K., and Larsen, G.C. (2003) A new method for prediction of detailed wake loads. In: S-E Thor (ed), Proceedings of *IEA Joint Action of Wind Turbines 16th Symposium*, Boulder, USA, May 2003 at NREL, pp. 171-188.

[2] Madsen, H.Aa., Larsen, G.C., Larsen, T.J., Troldborg, N., and Mikkelsen, R. (2010) *Calibration and validation of the Dynamic Wake Meandering model implemented in the aeroelastic code HAWC2*. *Journal of Solar Energy Engineering.* Volume 132, Issue 4, 041014 (14 pages).

[3] Larsen, G.C., Madsen, H.Aa., Thomsen, K., and Larsen, T.J. (2008) *Wake meandering — a pragmatic approach. Wind Energy,* **11**, 377-395.

[4] Frandsen, S.T. (2007) *Turbulence and turbulence-generated structural loading in wind turbine clusters.* Risø-R-1188(EN). Risø National Laboratory, Technical University of Denmark, Roskilde, Denmark.

[5] Bingöl, F., Mann, J., and Larsen, G.C. (2010) *Light detection and ranging measurements of wake dynamics, Part I: One-dimensional Scanning. Wind Energy.* **13,** 51-61.

[6] Trujillo, J.J., Bingöl, F., Larsen, G.C., Mann, J., and Kühn, M. (2011) *Light detection and ranging measurements of wake dynamics, Part II: two-dimensional scanning. Wind Energy.* **14,** 61-75.

[7] Ainslie, J.F. (1988) *Calculating the flow field in the wake of wind turbines. Journal of Wind Engineering and Industrial Aerodynamics*. 27, pp. 213-224.

[8] Ainslie, J.F., (1986) Wake modelling and the prediction of turbulence properties. In: *Proceedings of the 8th British Wind energy Association Conference*, Cambridge, 19-21 March 1986. pp. 115-120.

[9] Keck, RE., Veldkamp, D., Madsen, H.Aa., and Larsen, G.C. (2011) *Implementation of a mixing length turbulence formulation into the dynamic wake meandering model. Journal of Solar Energy Engineering*. Volume 134, Issue 2, 021012 (13 pages).

[10] Madsen, H.Aa., Larsen, G.C., and Thomsen, K. (2005). Wake flow characteristics in low ambient turbulence conditions. In: *Proceedings of Copenhagen Offshore Wind 2005*.

[11] Keck, R.E., de Mare, M., Churchfield, M.J., Lee, S., Larsen, G., Madsen, H.Aa. (2012) Two Improvements to the Dynamic Wake Meandering Model: Including the effects of atmospheric shear on wake turbulence and incorporating turbulence build up in a row of wind turbines. Submitted to *Journal of Wind Energy.* July

[12] Barthelmie, R.J., Hansen. K., Frandsen, S.T., Rathmann, O., Schepers, J.G., Schlez, W., Philips, J., Rados, K., Zervos, A., Politis, E.S., and Chaviaropoulos, P.K.. (2009) *Modelling and measuring flow and wind turbine wakes in large wind farms offshore. Wind Energy*. WE-08-0099.

[13] Obukhov, A.M. (1971) *Turbulence in an atmosphere with a non-uniform temperature. Boundary-Layer Meteorology 2.* 7-29.

[14] Monin, A.S., Obukhov, A.M. (1954) *Basic laws of turbulent mixing in the surface layer of the atmosphere*. Tr. Geofiz. Inst., Akad. Nauk SSSR, 151, 163–187.

[15] Businger, J., Wyngaard, J. C., Izumi, Y., & Bradley, E. F. (1971). *Flux-profile relationships in the atmospheric surface layer. Journal of the Atmospheric Sciences*. 28(2), 181-189.

[16] Kirchhoff, R.H., Kaminsky, F.C. (1983) *Wind shear measurements and synoptic weather categories for siting large wind turbines. Journal of Wind Engineering and Industrial Aerodynamics*. Volume 15, Issues 1–3, December, Pages 287-297, ISSN 0167-6105, 10.1016/0167-6105(83)90198-8.

[17] Irwin, J.S. (1967) *A theoretical variation of the wind profile power-law exponent as a function of surface roughness and stability. Atmospheric Environment.* Volume 13, Issue 1, 1979, Pages 191-194, ISSN 0004-6981, 10.1016/0004-6981(79)90260-9.

[18] Zoumakis, N. M. (1993) *The dependence of the power-law exponent on surface roughness and stability in a neutrally and stably stratified surface boundary layer. Atmosfera.* 6, 79-83.

[19] Barthelmie, R.J., Frandsen, S.T., Hansen, K., Schepers, J.G., Rados, K., Schlez, W., Neubert, A., Jensen, L.E., and Neckelmann, S. (2009) Modelling the impact of wakes on power output at Nysted and Horns Rev. In: *European Wind Energy Conference*.

[20] Wharton, S., Lundquist, J.K., Marjanovic, H. (2012) Synergistic effects of turbine wakes and atmospheric stability on power production at an offshore wind farm. LLNL-TR-524756, January

[21] Schepers, J., Obdam, T., and Prospathopoulos, J. (2011) *Analysis of wake measurements from the ECN wind turbine test site wieringermeer, EWTW. Wind Energy*. DOI:10.1002/we.488.

[22] Hansen, K., Barthelmie, R.J., Jensen, L., and Sommer, A. (2011) *The impact of turbulence intensity and atmospheric stability on power deficits due to wind turbine wakes at Horns Rev wind farm. Wind Energy*. DOI:10.1002/we.512.

[23] Sathe, A., Mann J., Barlas, T., Bierbooms, W.A.A.M., and van Bussel G.J.W. I(????) *Influence of atmospheric stability on wind turbine loads. Wind Energy*. DOI:10.1002/we.1528.

[24] Churchfield, M.J., Lee, S., Michalakes, J., and Moriarty, P.J. (2012) *A numerical study of the effects of atmospheric and wake turbulence on wind turbine dynamics. Journal of Turbulence*. Vol. 13, No. 14.

[25] Lee, S., A Clifton, and P. Moriarty. Wind turbine wakes and turbulence under various atmospheric boundary layers. Manuscript submitted to *Computer and Fluids*.

[26] Lavely, A. W., Vijayakumar, G., Kinzel, M. P., Brasseur, J. G., and Paterson, E. G. (2011) *Space-time loadings on wind turbine blades driven by atmospheric boundary layer turbulence.* AIAA. 2011-635,

[27] Peña, A., Gryning, S.-E., and Mann, J. (2010) On the length scale of the wind profile. Quarterly Journal of the Royal Meteorological Society. 136(653), 2119–2131.

[28] Keck, R.E., Mikkelsen, R., Troldborg, N., de Maré, M., and Hansen, K.. (2012) Synthetic atmospheric turbulence and wind shear in large eddy simulations of wind turbine wakes. Submitted to *Journal of Wind Energy*. August 2012

[29] Larsen, G.C., Madsen, H.Aa., Bingöl, F., Mann, J., Ott, S.,Sørensen, J.N., Okulov, V., Troldborg, N., Nielsen, M., Thomsen, K., Larsen, T.J., and Mikkelsen, R. (2007) *Dynamic wake meandering modelling. Risø-R-1607(EN).* Risø National Laboratory, Technical University of Denmark, Roskilde, Denmark,.

[30] Stull, R.B. (1988) An Introduction to Boundary Layer Meteorology, 666pp., Kluwer, Norwell, Mass..

[31] Wyngaard, J C. (2010) Turbulence in the Atmosphere. Cambridge University Press, New York. ISBN 978-0-521-88769-4.

[32] Mann, J. (1994) *The spatial structure of neutral atmospheric surface-layer turbulence. Journal of Fluid Mechanics*. 273, 141-168.

[33] Mann, J. (1998) *Wind field simulation. Probabilistic Engineering Mechanics*. Vol. 13, No. 4, pp. 269-282.

[34] Goodman, J. W. (2005) Introduction to Fourier Optics. Roberts & Company Publishers, Greenwood Village, Colo., p1.

[35] SOWFA project homepage: http://wind.nrel.gov/designcodes/simulators/sowfa/

[36] OpenFOAM, The Open Source CFD Toolbox, Version 2.1.1, [available online], URL: http://www.openfoam.com, 2012, OpenCFD Limited (ESI Group), [accessed 7 December 2012].

[37] Moeng, C.H. (1984) *A large-eddy simulation model for the study of planetary boundary layer turbulence. Journal of the Atmospheric Sciences*. Vol. 41, No. 13, July 1984, pp. 2052—2062.

[38] Larsen, G. C., Larsen, T. J., Madsen, H. A., Mann, J., Peña, A., Hansen, K. S., and Jensen, L. (2009). The dependence of wake losses on atmospheric stability characteristics. In: *Euromech Colloquium* (Vol. 508, pp. 35-37).

[39] Crespo, A., Hernandez, J., and Frandsen, S. (1999) *Survey of modelling methods for wind turbine wakes and wind farms. Wind Energy*. 2(1):1–24.

# Paper B

**A new approach to modeling the meandering of a wind turbine wake in homogeneous turbulence**

Martin de Maré, Jakob Mann, Matthew J. Churchfield and Edward G. Patton

*EWEA Offshore Conference 2013*

The paper has been updated since the conference.

# A new approach to modelling the meandering of a wind turbine wake in homogeneous turbulence

Martin de Maré[1,2], Jakob Mann[2], Matthew J. Churchfield [3] and Edward G. Patton[4]

[1] DONG Energy A/S, Denmark

[2] Wind Energy Department, Risø DTU, Denmark

[3] National Renewable Energy Laboratory, Golden, Colorado, USA

[4] National Center for Atmospheric Research, Boulder, Colorado, USA

**Abstract**

The meandering of a wind turbine wake is an important input to aero-elastic simulation of a wind turbine operating in the wake of other wind turbines. The current state-of-the-art method for simulating the meandering motion, models the wake as a passive tracer emitted in a frozen turbulence field.

The approach presented here replaces the frozen turbulence assumption and models the wake meandering motion by a process that could be described as a wavelength dependent random walk. The model output includes statistics of the meandering motion at any downstream position and these are compared to data from large eddy simulations with wind turbines represented as actuator lines, and to the afore-mentioned frozen turbulence method.

The presented model opens a new and promising avenue for efficient modelling of the downstream movement of a wind turbine wake.

## 1 Introduction

When designing the layout of wind farms, it is important to be able to assess accurately the loads and production of a wind turbine operating in the wake of another wind turbine. In the Dynamic Wake Meandering model, see e.g. [4], one of the leading models for this use, a wind speed deficit meanders downstream due to large scale turbulent eddies. The turbulent eddies are simulated using a large frozen turbulence field moving with the mean wind speed, in which the deficit is moving as a passive tracer.

Attempting an alternative approach to wake meandering, we start by deriving a simple model for the displacement of a thin line of a passive tracer, emitted in dynamically evolving turbulence. This model will then be applied to the process of wake meandering.

## 2 Preliminaries

Before we start modelling we first need to introduce a number of useful tools and concepts, starting with the *velocity covariance tensor*, $R_{ij}$,

$$R_{ij}(\boldsymbol{r}, \Delta t) = \left\langle u_i(\boldsymbol{x}, t_0) \cdot u_j\left(\boldsymbol{x} + \boldsymbol{r} + \frac{\partial U}{\partial z}\left(x_3 + r_3\right)\Delta t, t_0 + \Delta t\right)\right\rangle \tag{1}$$

where $u_i(\boldsymbol{x}, t)$ is the instantaneous wind speed at $\boldsymbol{x}$. Note that the coordinate system in which $\boldsymbol{x}$ is defined is Galilean, moving with, $U$, the mean wind speed at $x_3 = 0$. We assume the velocity field to be stationary, so, consequently, $R_{ij}$ does not depend on $t_0$, and also to be homogeneous, so that $R_{ij}$ does not depend on $\boldsymbol{x}$. We futhermore assume that $R_{ij}$ is symmetric such that

$$R_{ij}(\boldsymbol{r}, \Delta t) = R_{ji}(\boldsymbol{r}, \Delta t) \tag{2}$$

The spatial Fourier transform, $\Phi_{ij}$, of $R_{ij}$ is defined by

$$\Phi_{ij}(\boldsymbol{k}, \Delta t) = \frac{1}{(2\pi)^3} \iiint R_{ij}(\boldsymbol{r}, \Delta t) \cdot e^{-i\boldsymbol{k}\cdot\boldsymbol{r}} dr_1 dr_2 dr_3 \tag{3}$$

The cross-spectra, $\chi_{ij}\left(k_1, \Delta t\right)$, are defined as

$$\chi_{ij}\left(k_1, \Delta t\right) = \frac{1}{2\pi} \int R_{ij}\left(\left(r_1, 0, 0\right), \Delta t\right) \cdot e^{-ik_1 r_1} dr_1 \tag{4}$$

and can also be derived from $\Phi_{ij}$ as

$$\chi_{ij}(k_1, \Delta t) = \iint \Phi_{ij}\left(\left(k_1, \kappa_2, \kappa_3\right), \Delta t\right) d\kappa_2 d\kappa_3 \tag{5}$$

Using logic inspired by [4] the wind fluctuations assumed to advect a segment of a wake is approximated by the spatial averaging over a disc with a radius equal to rotor radius $R$

$$u_i^R(\boldsymbol{x}, t) = \frac{1}{\pi R^2} \iint_{y^2+z^2<R^2} u_i\left(\boldsymbol{x} + (0, y, z), t\right) dy dz \tag{6}$$

Using this averaged wind speed we define $R_{ij}^R$ analogously to eq. (1) and $\Phi_{ij}^R$ analogously to eq. (3). If so, it can be shown that $\Phi_{ij}^R$ relates to $\Phi_{ij}$ as

$$\Phi_{ij}^R(\boldsymbol{\kappa}, \Delta t) = \mathrm{jinc}\left(R \cdot \sqrt{k_2^2 + k_3^2}\right)^2 \cdot \Phi_{ij}(\boldsymbol{\kappa}, \Delta t) \tag{7}$$

where the *jinc*-function, also called the *bessinc*-function, is defined such that the 2-dimensional Fourier transform of a unit disc is given by $\pi \cdot \mathrm{jinc}(|k|)$. Analogous to eq. (4) we define the cross-spectra of the rotor averaged wind speed

$$\chi_{ij}^R(k_1, \Delta t) = \int \Phi_{ij}^R\left(\left(k_1, \kappa_2, \kappa_3\right), \Delta t\right) d\kappa_2 d\kappa_3 \tag{8}$$

We introduce $\boldsymbol{X}_{t_0}^{L,R}(\boldsymbol{x}_0, t)$, the position at $t$ of a rotor-sized passive tracer released at $\boldsymbol{x}_0$, at time, $t_0$. This position is by definition related to the wind speed, $\boldsymbol{u}^R(\boldsymbol{x}, t)$, by

$$\frac{\partial \boldsymbol{X}_{t_0}^{L,R}(\boldsymbol{x}_0, t)}{\partial t} = \boldsymbol{u}^R\Big(\boldsymbol{X}_{t_0}^{L,R}(\boldsymbol{x}_0, t), t\Big) \tag{9}$$

and

$$\boldsymbol{X}_{t_0}^{L,R}(\boldsymbol{x}_0, t_0) = \boldsymbol{x}_0 \tag{10}$$

Inspired by eq. (10) a rotor averaged Lagrangian wind speed is introduced and defined as

$$\boldsymbol{u}_{t_0}^{L,R}(\boldsymbol{x}_0, t) = \boldsymbol{u}^R\Big(\boldsymbol{X}_{t_0}^{L,R}(\boldsymbol{x}_0, t), t\Big) \tag{11}$$

In [1] and [3] it was found that the wake is not translated downstream with the mean wind speed, $U$, but, in the case of full induction, with a *wake transport velocity*, $U_{WT}$, which is more like $0.8 \cdot U$. Introducing $W_T = U_{WT} - U$ which is the wake transport speed relative to the moving coordinate system, we can define $\boldsymbol{X}_{t_0}^{L,R}(\boldsymbol{x}_0, t, W_T)$ such that

$$\begin{aligned} \frac{\partial \boldsymbol{X}_{t_0}^{L,R}(\boldsymbol{x}_0, t, W_T)}{\partial t} &= \boldsymbol{u}^R\Big(\boldsymbol{X}_{t_0}^{L,R}(\boldsymbol{x}_0, t, W_T), t\Big) + (W_T, 0, 0) \\ &= \boldsymbol{u}_{t_0}^{L,R}(\boldsymbol{x}_0, t, W_T) + (W_T, 0, 0) \end{aligned} \tag{12}$$

where also $\boldsymbol{u}_{t_0}^{L,R}(\boldsymbol{x}_0, t, W_T)$ has been introduced.

## 3 Studying a streamwise timeline

Before addressing wake meandering we will study a related, but less complicated situation. Let us define

$$\boldsymbol{L}_{t_0}^R(x_1,t,W_T) = \boldsymbol{X}_{t_0}^{L,R}((x_1,0,0),t,W_T) - (x_1 + W_T{\cdot}t,0,0) \tag{13}$$

If $W_T$ and $R$ are zero then $\boldsymbol{L}_{t_0}^R$ denotes the displacement of a so-called *timeline*, i.e. a line of passive tracers, released along a line in the streamwise direction, at $t_0$. In the more complicated case where $W_T$ and $R$ are not equal to zero $\boldsymbol{L}_{t_0}^R$ consequently denotes the displacement of rotor-sized passive tracers, released at $t_0$ along a line in the streamwise direction, having a wake transport velocity, $W_T$, superimposed on the velocity induced by the turbulent wind.

Equations (12) and (13) give

$$\frac{\partial \boldsymbol{L}_{t_0}^R(x_1,t,W_T)}{\partial t} = \boldsymbol{u}_{t_0}^{L,R}(\boldsymbol{x}_1,t,W_T) \tag{14}$$

where $\boldsymbol{x}_1 = (x_1,0,0)$ has been introduced.

We will attempt to make a model for $\boldsymbol{\Lambda}^R$ the cross spectra of $\boldsymbol{L}_{t_0}^R$, defined by

$$\Lambda_{ij}^R(k_1,\Delta t,W_T) = \frac{1}{2\pi}\int \left\langle L_{\iota,t_0}^R(x_1,t_0+\Delta t,W_T)\cdot L_{j,t_0}^R(x_1+r_1,t_0+\Delta t,W_T)\right\rangle e^{-ik_1r_1}dk_1 \tag{15}$$

We can analyse the evolution of $\Lambda_{ij}^R\left(k_1,\Delta t,W_T\right)$ by investigating its derivative

$$\begin{aligned}\frac{\partial \Lambda_{ij}^R(k_1,\Delta t,W_T)}{\partial \Delta t} &= \frac{1}{2\pi}\int \frac{\partial\left\langle L_{i,t_0}^R(x_1,t,W_T)\cdot L_{j,t_0}^R(x_1+r_1,t,W_T)\right\rangle}{\partial t}e^{-ik_1r_1}dr_1 \\ &= \frac{1}{2\pi}\int\left(\left\langle\frac{\partial L_{i,t_0}^R(x_1,t,W_T)}{\partial t}L_{j,t_0}^R(x_1+r_1,t,W_T)\right\rangle\right. \\ &\qquad \left.+\left\langle L_{i,t_0}^R(x_1,t,W_T)\frac{\partial L_{j,t_0}^R(x_1+r_1,t,W_T)}{\partial t}\right\rangle\right)e^{-ik_1r_1}dr_1\end{aligned} \tag{16}$$

wherein, and from here on $t = t_0 + \Delta t$. For clarity we now focus on the first term in the paranthesis of the integrand, on the RHS of eq. (16), i.e.

$$\begin{aligned}\left\langle\frac{\partial L_{i,t_0}^R(x_1,t,W_T)}{\partial t}L_{j,t_0}(x_1+r_1,t,W_T)\right\rangle &= \left\langle\frac{\partial L_{i,t_0}^R(x_1,t,W_T)}{\partial t}\int_{t_0}^t\frac{\partial L_{j,t_0}^R(x_1+r_1,\tau,W_T)}{\partial\tau}d\tau\right\rangle \\ &= \int_{t_0}^t\left\langle\frac{\partial L_{i,t_0}^R(x_1,t,W_T)}{\partial t}\frac{\partial L_{j,t_0}^R(x_1+r_1,\tau,W_T)}{\partial\tau}\right\rangle d\tau \\ &= \int_{t_0}^t\left\langle u_{i,t_0}^{L,R}(\boldsymbol{x}_1,t,W_T)\cdot u_{j,t_0}^{L,R}(\boldsymbol{x}_1+\boldsymbol{r}_1,\tau,W_T)\right\rangle d\tau \\ &\approx \int_{t_0}^t\left\langle u_{i,t_0}^{L,R}(\boldsymbol{x}_1,t_0,W_T)\cdot u_{j,t_0}^{L,R}(\boldsymbol{x}_1+\boldsymbol{r}_1,\tau,W_T)\right\rangle d\tau\end{aligned} \tag{17}$$

where $\boldsymbol{r}_1 = (r_1,0,0)$. In the last step of eq. (17) we have used the approximation

$$\left\langle u_{i,t_0}^{L,R}(\boldsymbol{x}_0,t,W_T)\cdot u_{j,t_0}^{L,R}(\boldsymbol{x}_0+\boldsymbol{r},t-\tau,W_T)\right\rangle \approx \left\langle u_{i,t_0}^{L,R}(\boldsymbol{x}_0,t_0,W_T)\cdot u_{j,t_0}^{L,R}(\boldsymbol{x}_0+\boldsymbol{r},t_0+\tau,W_T)\right\rangle \tag{18}$$

As illustrated in figure 1 it seems plausible that the approximation of eq. (18) performs well as long as the separation between the particles released at $\boldsymbol{x}_0$ and $\boldsymbol{x}_0+\boldsymbol{r}$ is kept i.e. as long as

$$\boldsymbol{X}_{t_0}^L(\boldsymbol{x}_0+\boldsymbol{r},t,W_T) - \boldsymbol{X}_{t_0}^L(\boldsymbol{x}_0,t,W_T) \approx \boldsymbol{r} \tag{19}$$

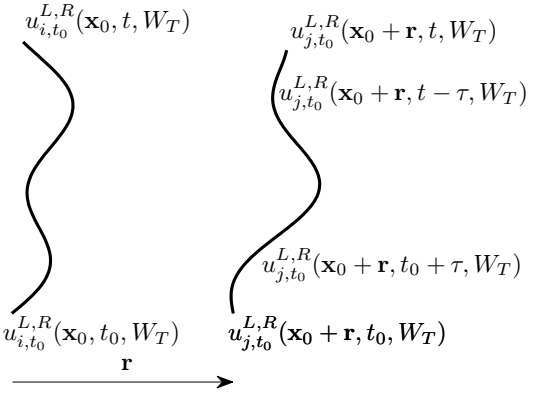


Figure 1: Illustration of two path lines, $\boldsymbol{X}^L_{t_0}(\boldsymbol{x}_0, t, W_T)$ and $\boldsymbol{X}^L_{t_0}(\boldsymbol{x}_0 + \boldsymbol{r}, t, W_T)$, of particles released at time, $t_0$, a distance, $\boldsymbol{r}$, apart. The approximation of eq. (18) likely performs well as long as $\boldsymbol{X}^L_{t_0}(\boldsymbol{x}_0 + \boldsymbol{r}, t, W_T) - \boldsymbol{X}^L_{t_0}(\boldsymbol{x}_0, t, W_T) \approx \boldsymbol{r}$.

However for a large $t$ eq. (19) is no longer true and then it is hard to imagine the approximation in eq. (18) performing well. From this arguement it is clear that the results from here will loose validity as $t$ becomes large.

We will now continue with both terms of eq. (16) and we will start by making the following approximation

$$\left\langle u^{L,R}_{i,t_0}(\boldsymbol{x}_0, t_0, W_T) \cdot u^{L,R}_{j,t_0}(\boldsymbol{x}_0 + \boldsymbol{r}, t_0 + \Delta t, W_T) \right\rangle \approx \left\langle u^R_i(\boldsymbol{x}_0, t_0) \cdot u^R_j(\boldsymbol{x}_0 + \boldsymbol{r} + (W_T \cdot \Delta t, 0, 0), t_0 + \Delta t) \right\rangle \tag{20}$$

where, as seen, the wind speed is Lagragian on the LHS, and Eulerian on the RHS. For $W_T$ and $R$ equal to zero this is an extension of an assumption attributed to Corrsin who assumed eq. (20) with $\boldsymbol{r} = 0$. That, less general, version of eq. (20) was validated for isotropic turbulence in [6].

Using equations (17) and (20), eq. (16) continues,

$$\begin{aligned}
\frac{\partial \Lambda^R_{ij}(k_1, \Delta t, W_T)}{\partial \Delta t} &\approx \frac{1}{2\pi} \int \left( \int_{t_0}^{t} \left\langle u^{L,R}_{i,t_0}(\boldsymbol{x}_1, t_0, W_T) \cdot u^{L,R}_{j,t_0}(\boldsymbol{x}_1 + \boldsymbol{r}_1, \tau, W_T) \right\rangle d\tau \right. \\
&\qquad \left. + \int_{t_0}^{t} \left\langle u^{L,R}_{i,t_0}(\boldsymbol{x}_1, \tau, W_T) \cdot u^{L,R}_{j,t_0}(\boldsymbol{x}_1 + \boldsymbol{r}_1, t_0, W_T) \right\rangle d\tau \right) e^{-ik_1 r_1} dk_1 \\
&\approx \frac{1}{2\pi} \int \left( \int_{t_0}^{t} \left\langle u^R_i(\boldsymbol{x}_1, t_0) \cdot u^R_j(\boldsymbol{x}_1 + \boldsymbol{r}_1 + (W_T \cdot \tau, 0, 0), \tau) \right\rangle d\tau \right. \\
&\qquad \left. + \int_{t_0}^{t} \left\langle u^R_i(\boldsymbol{x}_1 + (W_T \cdot \tau, 0, 0), \tau) \cdot u^R_j(\boldsymbol{x}_1 + \boldsymbol{r}_1, t_0) \right\rangle d\tau \right) e^{-ik_1 r_1} dk_1 \\
&= \int_0^{\Delta t} \left( \frac{1}{2\pi} \int R^R_{ij}((r_1 + W_T \cdot \tau, 0, 0), \tau) e^{-ik_1(r_1 + W_T \cdot \tau)} e^{ik_1 W_T \cdot \tau} dk_1 \right. \\
&\qquad \left. + \frac{1}{2\pi} \int R^R_{ij}((r_1 - W_T \cdot \tau, 0, 0), \tau) e^{-ik_1(r_1 - W_T \cdot \tau)} e^{-ik_1 W_T \cdot \tau} dk_1 \right) d\tau \\
&= \int_0^{\Delta t} \left( \chi^R_{ij}(k_1, \tau) e^{ik_1 W_T \cdot \tau} + \chi^R_{ij}(k_1, -\tau) e^{-ik_1 W_T \cdot \tau} \right) d\tau \\
&= 2 \int_0^{\Delta t} \chi^R_{ij}(k_1, \tau) \cos(k_1 W_T \cdot \tau) \, d\tau
\end{aligned} \tag{21}$$

In order to get further we crudely approximate $\chi_{ij}^R$ by a tent function, i.e.

$$\chi_{ij}^R(k_1,\Delta t) \approx \chi_{ij}^R(k_1,0)\frac{T_{ij,\chi}^R(k_1)-\frac{1}{2}|\Delta t|}{T_{ij,\chi}^R(k_1)}\Theta\left(T_{ij,\chi}^R(k_1)-\frac{1}{2}|\Delta t|\right) \tag{22}$$

where $\Theta(t)$ is the Heaviside step function and $T_{ij,\chi}^R$ is an integral time scale of the coherence of $\chi_{ij}^R$, defined as

$$T_{ij,\chi}^R(k_1) = \frac{\int_0^\infty |\chi_{ij}^R(k_1,\tau)|d\tau}{\sqrt{\chi_{ii}^R(k_1,0)\chi_{jj}^R(k_1,0)}}, \tag{23}$$

with no summation over the repeated indexes in the denominator intended. Approximating $\chi_{ij}^R$ by eq. (22) is an implicit assumption that wind speed at $t$ only contributes to $\Lambda_{ij}^R$ for a particular wave number, $k_1$, until on average $t+2T_{ij,\chi}^R(k_1)$, i.e. until the tent function in eq. (22) reaches zero. After this time the contribution to $\Lambda_{ij}^R$ from the wind speed is uncorrelated with the contribution at $t$, thus the process can thought of as a wave number dependent random walk, in which $\Lambda_{ij}^R$ gets a new and uncorrelated contribution every $2T_{ij,\chi}^R(k_1)$.

Using eq. (22) we can carry out the integration of eq. (21) to obtain $\frac{\partial\Lambda_{ij}^R(k_1,\Delta t,W_T)}{\partial\Delta t}$. Integrating once more we get

$$\begin{aligned}\Lambda_{ij}^R(k_1,\Delta t,W_T) = \frac{\chi_{ij}^R(k_1,\tau)}{k_1^3\cdot W_T^3\cdot T_{ij,\chi}^R(k_1)}\Bigg(&k_1\cdot W_T\cdot\left(|\Delta t|+2T_{ij,\chi}^R(k_1)\right)\\ &-k_1\cdot W_T\left(|\Delta t|-2T_{ij,\chi}^R(k_1)\right)\cos(k_1\cdot W_T\cdot T)^2-2\sin\left(2k_1\cdot W_T\cdot T_{ij,\chi}^R(k_1)\right)+\\ &\Theta\left(T_{ij,\chi}^R(k_1)-\frac{1}{2}|\Delta t|\right)\\ &\cdot\left(k_1\cdot W_T\cdot\left(|\Delta t|-2T_{ij,\chi}^R(k_1)\right)\left(\cos(k_1\cdot W_T|\Delta t|)+\cos\left(2k_1\cdot W_T\cdot T_{ij,\chi}^R(k_1)\right)\right)\right.\\ &\left.-2\sin(k_1\cdot W_T|\Delta t|)+2\sin\left(2k_1\cdot W_T\cdot T_{ij,\chi}^R(k_1)\right)\right)\Bigg)\end{aligned} \tag{24}$$

# 4 Modelling wake meandering

We are interested in studying a wake released at a stationary point that, say, has coordinate $(0,0,0)$ at $t=0$. As our coordinate system is moving with $U$, our source accordingly has a streamwise coordinate given by $x_1(t) = -U\cdot t$. Furthermore, let us assume that the separation between the release point and the observation point, i.e. the downstream wind turbine affected by the wake, is $s$. A wake reaching the observation point at $t$ must have been released at $t-s/U_{WT}$ from our release point, which then had streamwise coordinate $-U\cdot(t-s/U_{WT})$. In terms of $\boldsymbol{X}_{t_0}^R(x_1,t,W_T)$ we are, with the above notation, thus interested in

$$\boldsymbol{m}^R(t,s,U,U_{WT}) = \boldsymbol{X}_{t-s/U_{WT}}^{L,R}\left(-U\cdot(t-s/U_{WT}),t,U_{WT}-U\right)-(-Ut+s,0,0) \tag{25}$$

Note the subscript $t-s/U_{WT}$ of $\boldsymbol{X}_{t-s/U_{WT}}^{L,R}$ which means that the release time is not the same for all wake segments. This situation is fairly complicated so we choose to introduce

$$\begin{aligned}\boldsymbol{n}^R(\tau,s,U,U_{WT}) = \boldsymbol{X}_{t_0=0}^{L,R}&\left(-U\cdot(\tau-s/U_{WT}),s/U_{WT},U_{WT}-U\right)\\ &-(-U\cdot\tau+s,0,0)\end{aligned} \tag{26}$$

where, as seen, the release time is again fixed, to $t_0=0$. We will assume that $\boldsymbol{n}^R$ in suitable ways is similar to $\boldsymbol{m}^R$, although $\boldsymbol{m}^R$ as shown in figure 2 denotes wake segments being emitted continoulsy from a point source, while $\boldsymbol{n}^R$ denotes wake segments being emmitted all at once along a line, and being studied after a fixed time.

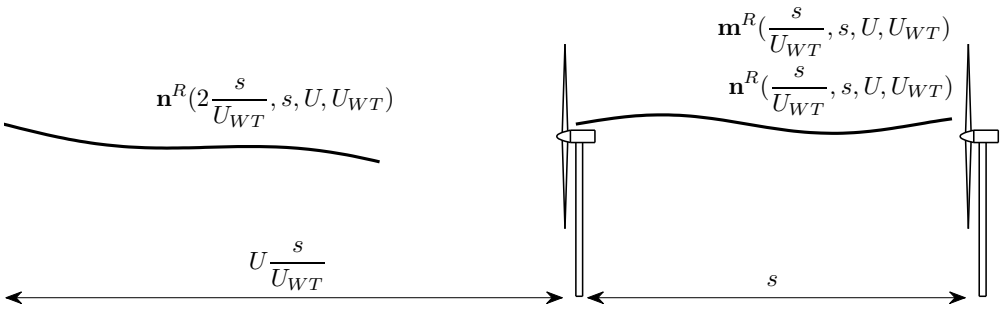


Figure 2: Snapshot of pathlines of wake segment at $t = \frac{s}{U_{WT}}$. All wake segments shown in the figure were released at $t_0 = 0$. The wake segment released at this moment from the left-most wind turbine will reach the right-most wind turbine at $2\frac{s}{U_{WT}}$, and will thus be denoted $\boldsymbol{m}^R\left(2\frac{s}{U_{WT}}, s, U, U_{WT}\right)$. The corresponding wake segment $\boldsymbol{n}^R\left(2\frac{s}{U_{WT}}, s, U, U_{WT}\right)$ was, as shown in the figure, released at $t_0 = 0$, from a point well upstream of both wind turbines. It so happens that the captured moment, i.e. $t = \frac{s}{U_{WT}}$, is the exact moment the displacements of all wake segments denoted $\boldsymbol{n}^R$ should be observed.

The precise assumption we will make is

$$\left\langle m_i^R(t_1, s_1, U, U_{WT}) \cdot m_j^R(t_2, s_2, U, U_{WT}) \right\rangle \approx \left\langle n_i^R(t_1, s_1, U, U_{WT}) \cdot n_j^R(t_2, s_2, U, U_{WT}) \right\rangle \tag{27}$$

Although not very clear from its formulation, eq. (27), similarly to the frozen turbulence assumption, assumes that the spatial and temporal spectra are very closely related. It should however be noted that eq. (27) does not go as far as to actually impose frozen turbulence.

By noting that

$$\boldsymbol{n}^R(\tau, s, U, U_{WT}) = \boldsymbol{L}^R_{t_0=0}(-U \cdot (\tau - s/U_{WT}), s/U_{WT}, U_{WT} - U) \tag{28}$$

we can now estimate $\boldsymbol{M}^R$, the cross-spectra of $\boldsymbol{m}^R$ with respect to frequency, $f$,

$$\begin{aligned}
M_{ij}^R(f, s, U, U_{WT}) &= \int \left\langle m_i^R(t, s, U, U_{WT}) \cdot m_j^R(t + \tau, s, U, U_{WT}) \right\rangle e^{-i\tau 2\pi f} d\tau \\
&\approx \int \left\langle n_i^R(t, s, U, U_{WT}) \cdot n_j^R(t + \tau, s, U, U_{WT}) \right\rangle e^{-i\tau 2\pi f} d\tau \\
&= \int \left\langle L_{i,t_0=0}^R(-U \cdot (t - s/U_{WT}), s/U_{WT}, U_{WT} - U) \cdot \right. \\
&\quad \left. L_{j,t_0=0}^R(-U \cdot (t + \tau - s/U_{WT}), s/U_{WT}, U_{WT} - U) \right\rangle e^{-i\tau 2\pi f} d\tau \\
&= \int \left\langle L_{i,t_0=0}^R(-U \cdot (t - s/U_{WT}), s/U_{WT}, U_{WT} - U) \cdot \right. \\
&\quad \left. L_{j,t_0=0}^R(-U \cdot (t - s/U_{WT}) - r_1, s/U_{WT}, U_{WT} - U) \right\rangle e^{-ir_1 \frac{1}{U} 2\pi f} \frac{1}{U} dr_1 \\
&= \frac{2\pi}{U} \Lambda_{ji}^R(\frac{2\pi f}{U}, s/U_{WT}, U - U_{WT}))
\end{aligned} \tag{29}$$

where $\boldsymbol{\Lambda}_{ji}^R$ can be evaluated using eq. (24).

# 5 Validation

To test the validity of our model we study the wake meandering in Large Eddy Simulations (LES), where wind turbines are represented by actuator lines. We use the simulations described in [2], where the turbine diameter is $80m$, the hub height is $70m$, the free wind speed is $8m/s$ and the turbulence intensity is between $0.06$ and $0.07$.

The preferred starting point for evaluating our model is to know $\Phi_{ij}(\boldsymbol{k}, \Delta t)$ and with this objective in mind, we start by choosing $\Phi_{ij}(\boldsymbol{k}, 0)$ as the Mann spectral tensor, see [5], with parameters $\alpha\epsilon^{\frac{2}{3}} = 0.0239$, $L_{Mann} = 28.4$ and $\Gamma = 2.675$ . Figure 3 shows a comparison between the spectra as derived from the Mann spectral tensor compared to the spectra of the LES.

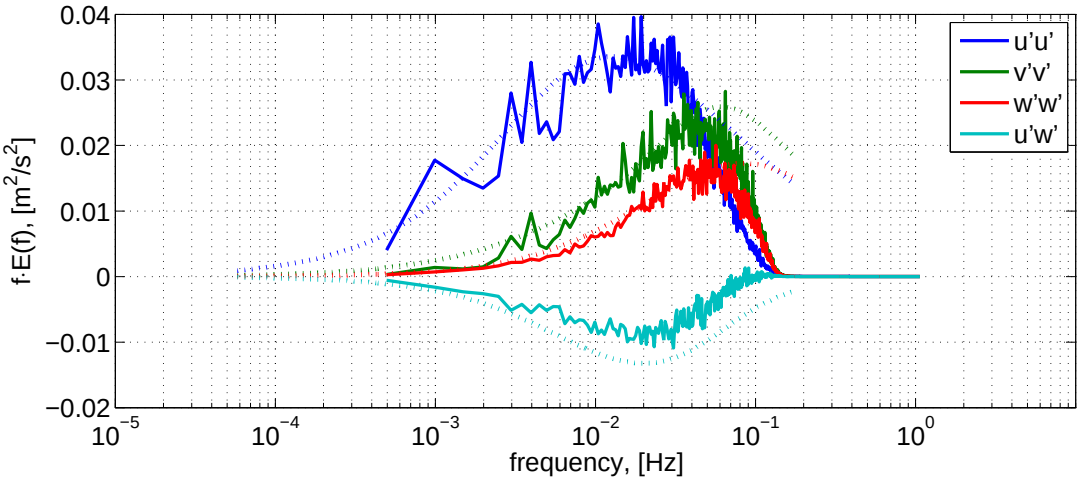


Figure 3: Comparison between the temporal spectra from the simulations and the temporal spectra derived from the Mann spectral tensor, with parameters $\alpha\epsilon^{\frac{2}{3}} = 0.0239$, $L_{Mann} = 28.4$ and $\Gamma = 2.675$,

As the LES spectra in figure 3 trails off faster than $k_1^{-5/3}$ due to numerical dissipation, only $\alpha\epsilon^{\frac{2}{3}}$ was determined according to the method outlined in [5]. The other two parameters, $L_{Mann}$ and $\Gamma$, were instead extracted from [7].

We proceed by generalising an expression for longitudinal coherence per wavenumber

$$\Phi_{ij}^{iso}(\boldsymbol{k}, \Delta t) = \Phi_{ij}^{iso}(\boldsymbol{k}, 0) e^{-\frac{1}{2} 0.5^2 \langle u_1 u_1 \rangle |k|^2} \tag{30}$$

which was tested for isotropic turbulence in [6], for the case of anisotropic turbulence, obtaining

$$\Phi_{ij}(\boldsymbol{k}, \Delta t) = \Phi_{ij}(\boldsymbol{k}, 0) e^{-\frac{1}{2} 0.5^2 \langle u_i u_j \rangle k_i k_j t^2} \tag{31}$$

From $\Phi_{ij}(\boldsymbol{k}, \Delta t)$ we calculate $\chi_{ij}^R(k_1, 0)$ according to (7) and (8), as well as $T_{ij,\chi}^R(k_1)$ according to (23), and obtain $\chi_{ij}^R(k_1, \Delta t)$ according to (22). We now calculate $M_{ij}^R(f, s, U, U_{WT})$ according to (24) and (29).

Following the procedure described in [2] we extract meandering time series, shown in figure 4, from the LES and calculate spectra. In figure 5 we compare these spectra to $M_{ij}^R(f, s, U, U_{WT})$, as well as spectra calculated using the frozen turbulence method, as described in [2].

We conclude from figure 5 that our model performs better than the frozen turbulence method. We also conclude that the model is valid, at least for the tested case, for the range most relevant for aero-elastic simulation.

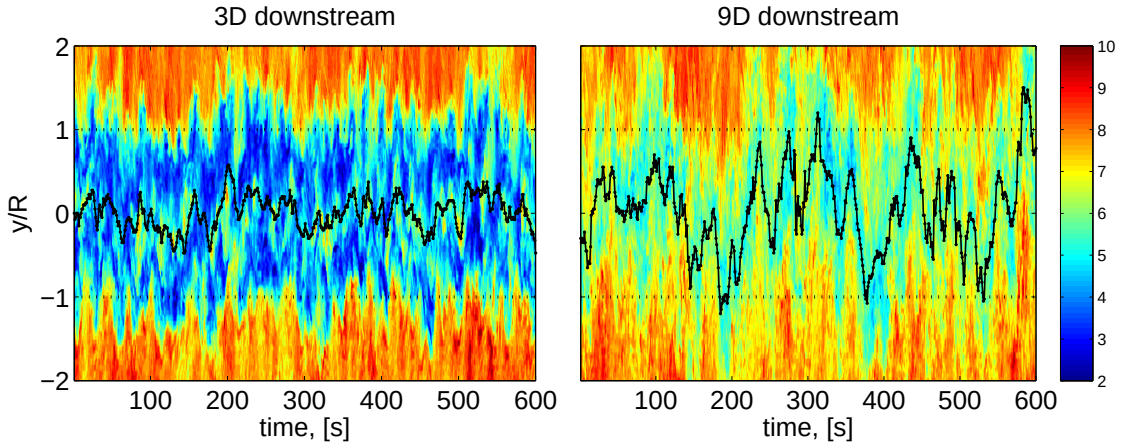


Figure 4: Extracting meandering time series (the black line)

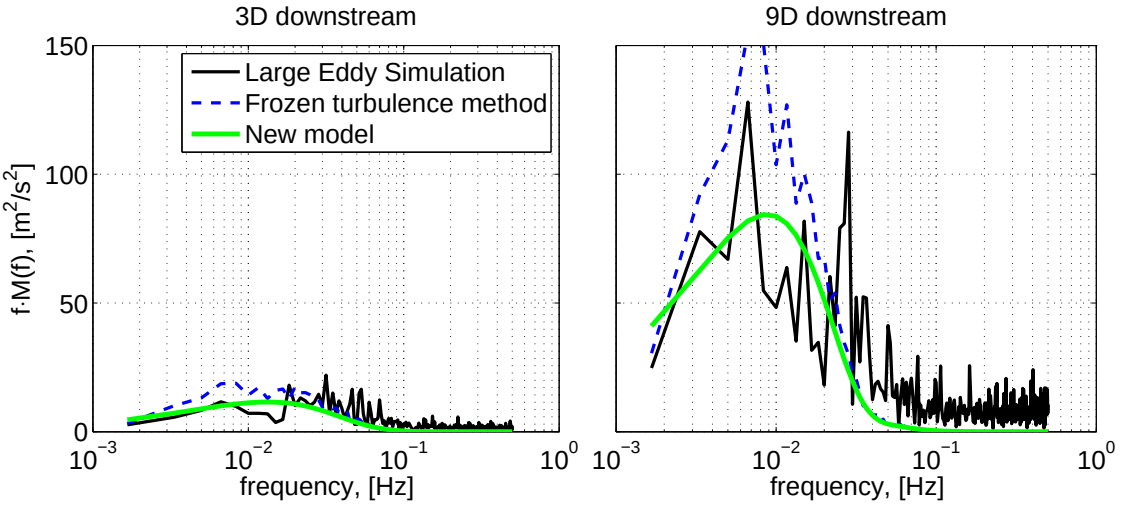


Figure 5: Comparison of $M_{ij}^{R}(f, s, U, U_{WT})$ to auto-spectra calculated from the timeseries shown in figure 4, as well as spectra calculated using the frozen turbulence method described in [2].

## 6 Conclusions

We have developed a model for the displacement of the wind turbine wake as it is transported downstream. The approach presented here aims at eventually replacing the frozen turbulence assumption which is the current state-of-the-art approach for meandering. Our new approach models instead the wake meandering motion by a process that could be described as a wavelength dependent random walk.

To make use of the model, knowing the velocity covariance tensor, $R_{ij}(\boldsymbol{r}, \Delta t)$, is preferable. This information can be obtained by combining the Mann spectral tensor with an assumption for the longitudinal coherence per wavenumber.

The model output, spectra of the meandering motion at any downstream position, was compared to meandering in LES and was found to perform better than the current state-of-the-art method.

## References

1. Bingöl F, Mann J, Larsen GC. Light detection and ranging measurements of wake dynamics part I: one-dimensional scanning. Wind Energy 2010; 13:51–61.

2. Keck RE, de Maré M, Churchfield MJ, Lee S, Larsen G, Madsen HA. On atmospheric stability in the dynamic wake meandering model 2013; .

3. Keck RE, Mikkelsen R, Troldborg N, de Maré M, Hansen KS. Synthetic atmospheric turbulence and wind shear in large eddy simulations of wind turbine wakes. Wind Energy 2013; :n/a—-n/a.

4. Larsen GC, Madsen HA, Thomsen K, Larsen TJ. Wake meandering: a pragmatic approach. Wind Energy 2008; 11:377–395.

5. Mann J. Wind field simulation. Probabilistic Engineering Mechanics 1998; 13:269–282.

6. Ott S, Mann J. An experimental test of Corrsin's conjecture and some related ideas. New Journal of Physics 2005; 7:142.

7. Peña A, Gryning SE, Mann J. On the length-scale of the wind profile. Quarterly Journal of the Royal Meteorological Society 2010; 136:2119–2131.

# Paper C

**Validation of the Mann spectral tensor for offshore wind conditions at different atmospheric stabilities**

Martin de Maré and Jakob Mann

*Journal of Physics: Conference Series Volume 524, Conference 1, 2014*

# Validation of the Mann spectral tensor for offshore wind conditions at different atmospheric stabilities

**Martin de Maré**[1,2] **and Jakob Mann**[2]

[1] DONG Energy A/S, Denmark
[2] Wind Energy Department, Risø DTU, Denmark

E-mail: mardm@dongenergy.dk

**Abstract.** Simulated wind fields are very useful when predicting loads on structures subjected to turbulent winds, wind turbines being a prime example. Knowledge of statistical properties such as the spatial and temporal correlations of real turbulent wind fields increases the realism of the simulated simulated wind fields. The statistical properties of real turbulent wind fields have been shown to depend on quantities such as the surface roughness, the mean wind speed, measurement height and atmospheric stability. The Mann spectral tensor attempts to predict all spatial correlations of shear generated turbulence given only three input parameters. The most suitable such input values have been investigated for different onshore surface roughnesses, but so far not for typical offshore conditions. The meteorological mast at the Rødsand II offshore wind farm has among other instruments sonic anemometers mounted at 15, 40 and 57 meters above sea level. Wind speed spectra at the three heights are calculated and binned with respect to both wind speed and atmospheric stability. The three parameters of the Mann spectral tensor are determined to ensure best fit to the spectra of each of the bins and are presented as a function of mean wind speed, measurement height and atmospheric stability. The behaviour of the presented parameters values are largely consistent with the previous onshore results. The parameter values are also compared to potentially related quantities and a constant quantity is derived. Given optimal parameters the spectral tensor is found to reproduce the surface layer generated turbulence well, also for different atmospheric stabilities, however in the wind speed spectra a contribution from the very large scale quasi-geostrophic turbulence is also observed, a contribution the spectral tensor does not attempt to model.

## 1. Introduction

The Mann spectral tensor [3] attempts to predict all second order spatial statistics of shear generated turbulence given only three input parameters, $\alpha\epsilon^{2/3}$, $L_M$ and $\Gamma$. The tensor can for example be used to generate realistic simulated turbulent wind fields, see [4]. These simulated wind fields are very useful as input to aero-elastic simulation of structures subjected to turbulent flows, wind turbines being a prime example.

The statistical properties of real turbulent wind fields has been shown to depend on quantities such as the surface roughness, the mean wind speed, measurement height and atmospheric stability. Although the Mann spectral tensor is developed for neutral atmospheric stability, the parameter values which describe the turbulence best for different atmospheric stabilities has been investigated using onshore measurements, see e.g. [1] and [6]. We will attempt to determine the

parameter values suitable for offshore conditions, at different wind speed, measurement height and atmospheric stability.

## 2. Methodology

The data was collected at the meteorological mast at the Rødsand II offshore wind farm, which is situated just south of the Danish island Lolland, from February 2010 to October 2012. We select wind directions from 255° to 285° where the wind has a fetch over water of approximately 100km. Among other instruments the mast has 3 Campbell Scientific sonic anemometers, a type that includes a temperature sensor, at 15, 40 and 57 meters above sea level. We will quantify atmospheric stability based on the Monin-Obukhov length [5], which is defined as

$$L = -\frac{{u_{*0}}^3 T_0}{\kappa g \overline{u_3 \Theta'_{v0}}} \tag{1}$$

where $u_{*0} = \sqrt{-\overline{u_1 u_3}}$ is the friction velocity, $T_0$ is the absolute temperature, $\kappa \approx 0.4$ is the von Karman constant and $\Theta'_v$ is the fluctuation in virtual potential temperature, all at the surface. We approximate these surface values with values measured at 15 m.

We employ Taylor's frozen turbulence assumption in order to estimate the spatial cross-spectra defined as

$$F_{ij}\left(k_1\right) = \frac{1}{2\pi} \int \left\langle u_i(\boldsymbol{x}, t)\, u_j(\boldsymbol{x} + (r_1, 0, 0)\,, t) \right\rangle e^{-\mathrm{i} k_1 r_1} \mathrm{d}r_1 \tag{2}$$

from 30-minute periods of measured wind velocities. These calculated cross-spectra are compared to cross-spectra derived from the spectral tensor, see [3].

We bin the data simultaneously for the 3 atmospheric stability classes shown in in table 1 and 3 wind speed bins, 8, 10 and 12 $\mathrm{ms}^{-1} \pm 1\ \mathrm{ms}^{-1}$, based on the anemometer at 15 m, resulting in a total of 9 bins per measurement height.

**Table 1:** Atmospheric stability bins

| Atmospheric stability class | Monin-Obukhov length interval (m) |
|---|---|
| Unstable (U) | $-200 \leq L \leq -100$ |
| Neutral (N) | $500 \leq \lvert L \rvert$ |
| Stable (S) | $50 \leq L \leq 200$ |

In each bin the spectra are normalized with the for each time period corresponding $u_{*0}$. The normalized spectra are averaged using the method of bins with respect to $\log(k_1)$, using a bin size of $0.2 \log(10)$. In order to make the fitting algorithm more robust we depart from the fitting procedure outlined in [3] in that we first determine $L_M$ by fitting all parameters only to $F_{33}\left(k_1\right)$ and $F_{13}\left(k_1\right)$. Keeping $L_M$ constant we then use $F_{11}\left(k_1\right)$, $F_{22}\left(k_1\right)$ and $F_{33}\left(k_1\right)$ to determine which $\alpha\epsilon^{2/3}$ and $\Gamma$ that gives the best fit. In this last step we only use one decade of the spectra, centered around $k_1 = L_M^{-1}$. For bins where both algorithms performed well, no systematic change in the resulting parameter values due to the change in method was observed.

The vertical wind speed gradient, $\frac{\partial U}{\partial z}$, is calculated by fitting a logarithmic profile to the mean wind speeds at the 3 measurement heights. This method is robust but not very precise as the

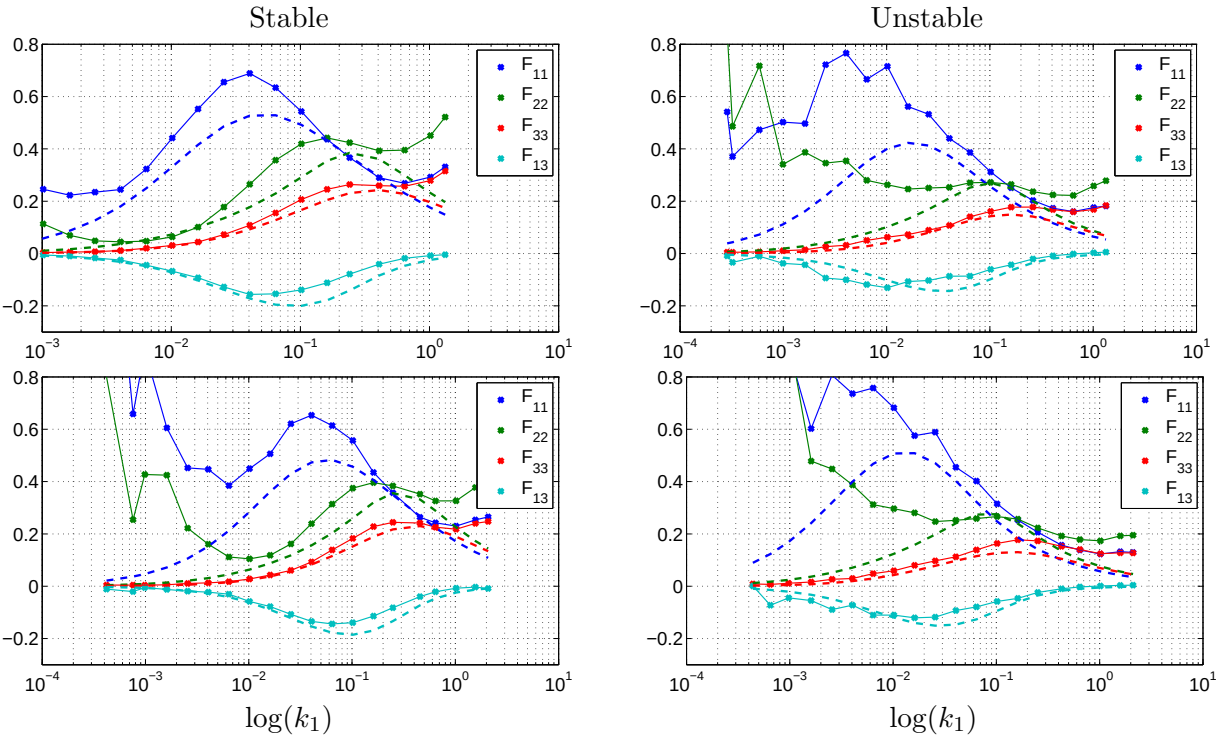


**Figure 1:** Spectra, $k_1E(k_1)/{u_{*0}}^2$ versus $\log(k_1)$ for the bins Stable and Unstable at 15 meters. The top row graphs shows spectra from the wind speed bin 12 ms$^{-1}$ and bottom row show the wind speed bin 8 ms$^{-1}$. The broken lines are the best fit of spectra derived from the Mann spectral tensor. For the $F_{11}$ and $F_{22}$ components we notice high energy levels at low wave numbers which are not matched in the Mann spectral tensor spectra, especially for the lower wind speed bin (bottom row).

wind profile is expected to be logarithmic only for the neutral case and then only close to the ground where $u_*$ is approximately constant. We see in the graph to the right in figure 7 that assuming $u_*$ to be constant is a not a good approximation in this case.

## 3. Results and discussion

The performance of the fitting algorithm is exemplified in figure 1 where the calculated spectra from a few bins are shown. We notice relatively high energy levels at low wave numbers which are not matched in the Mann spectral tensor spectra, especially in the lower wind speed bin. This behavior is not present in the vertical (red) component, which suggests that we are observing the high wave number end of the very large scale *quasi-geostrophic* turbulence, discussed e.g. in [2] and [8]. In figure 2 spectra using 90 minutes instead of 30 minutes of data are shown for the bins Stable and Unstable at 15 meters. The streamwise and lateral component shows a $|\boldsymbol{k}|^{-5/3}$-slope for low wave numbers, which is consistent with this being quasi-geostrophic turbulence.

In figures in 3 to 5 the resulting parameter values are plotted as a function of measurement height and wind speed. We notice that the wind speed has almost no influence on the parameter values while both atmospheric stability and measurement height are important factors. The results in figures 3 to 5 are consistent with what was observed in [1] and [6] except for the value of the parameter $\Gamma$ which here and in [1] decreases with stability, while [6] reports a more complex behavior.

Studying the equation for turbulent kinetic energy which can be derived from the Navier-Stokes

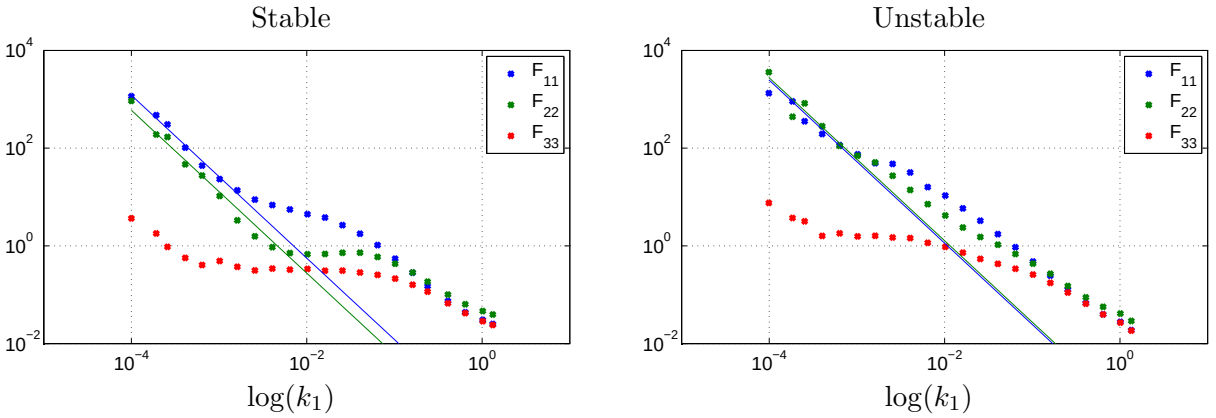


**Figure 2:** Spectra using 90 minutes of data, $\log(E(k_1))$ versus $\log(k_1)$, for the bins Stable and Unstable at 15 meters. The solid lines highlight the $|\boldsymbol{k}|^{-5/3}$-slope of $E(k_1)$ for low wave numbers. The fact that the wind speed bin is 12 ms$^{-1}$ shows that this contribution is present also for high wind speeds.

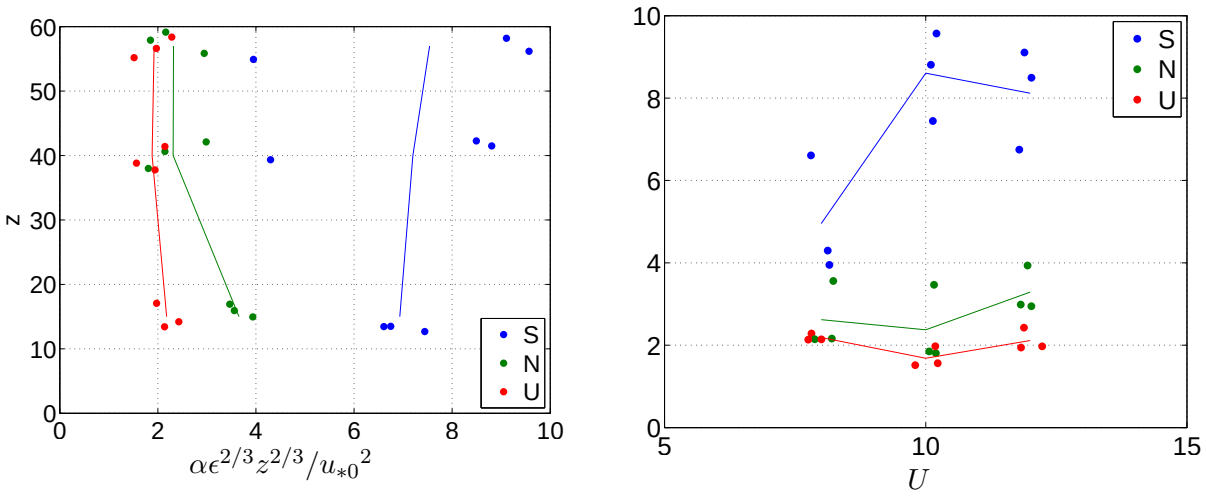


**Figure 3:** The parameter $\alpha\epsilon^{2/3}$ (normalized with measurement height $z$ and $u_{*0}$) as a function of measurement height and wind speed $U$. A small random offset has been added to the measurement height and wind speed for readability. Note that the x-axis of the left plot is the y-axis of the right plot.

equation the energy transfer from the mean flow is $-\overline{u_1 u_3}\frac{\partial U}{\partial z}$. In the left plot of figure 6 we see this turbulent energy production to the power $\frac{2}{3}$ divided by $\alpha\epsilon^{2/3}$. If the production and the dissipation were in perfect balance we would expect this ratio to be $\frac{1}{\alpha}$. In [7] the value 0.5 of $C_k$, the Kolmogorov constant for the one-dimensional spectra, is proposed, and this value combined with $\alpha = \frac{55}{18}C_k$ gives $\frac{1}{\alpha} \approx 0.65$.

In the plot to the right in figure 6 we see the ratio between the mixing length defined by $l_{mix}\frac{\partial U}{\partial z} = u_*$, and $L_M$. The result agrees reasonably but not perfectly with the $\frac{1}{1.70} \approx 0.59$ reported in [6].

In [3] the so called eddy life time, $\tau(|\boldsymbol{k}|)$, is given by

$$\tau(|\boldsymbol{k}|) = \Gamma \left(\frac{\partial U}{\partial z}\right)^{-1} \frac{|\boldsymbol{k}|^{-2/3} L_M^{-2/3}}{\sqrt{{}_2\mathrm{F}_1\left(\frac{1}{3}, \frac{17}{6}, \frac{4}{3}, -|\boldsymbol{k}|^{-2} L_M^{-2}\right)}}. \tag{3}$$

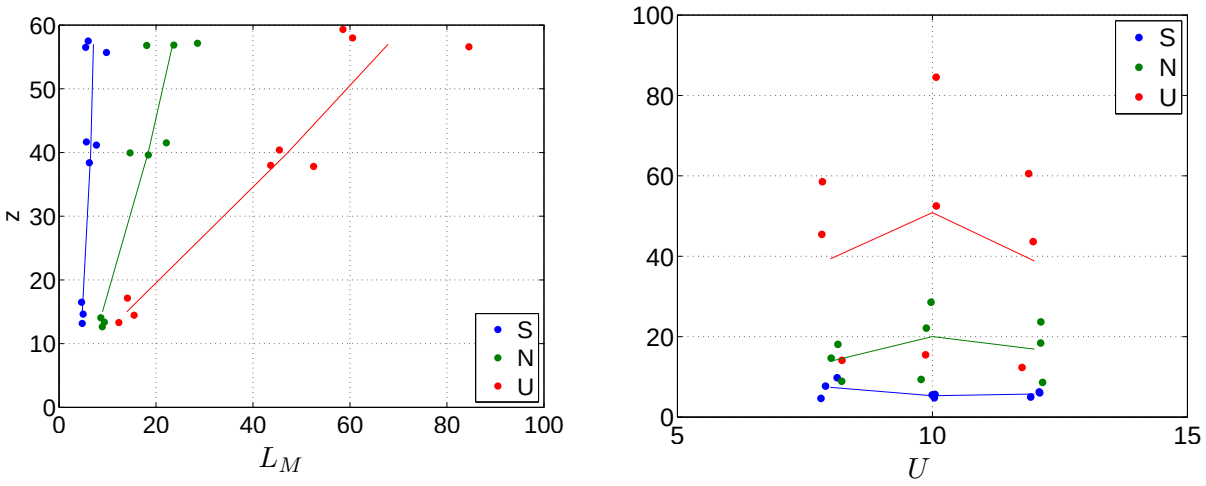


**Figure 4:** The parameter $L_M$ as a function of measurement height $z$ and wind speed $U$. A small random offset has been added to the measurement height and wind speed for readability. Note that the x-axis of the left plot is the y-axis of the right plot.

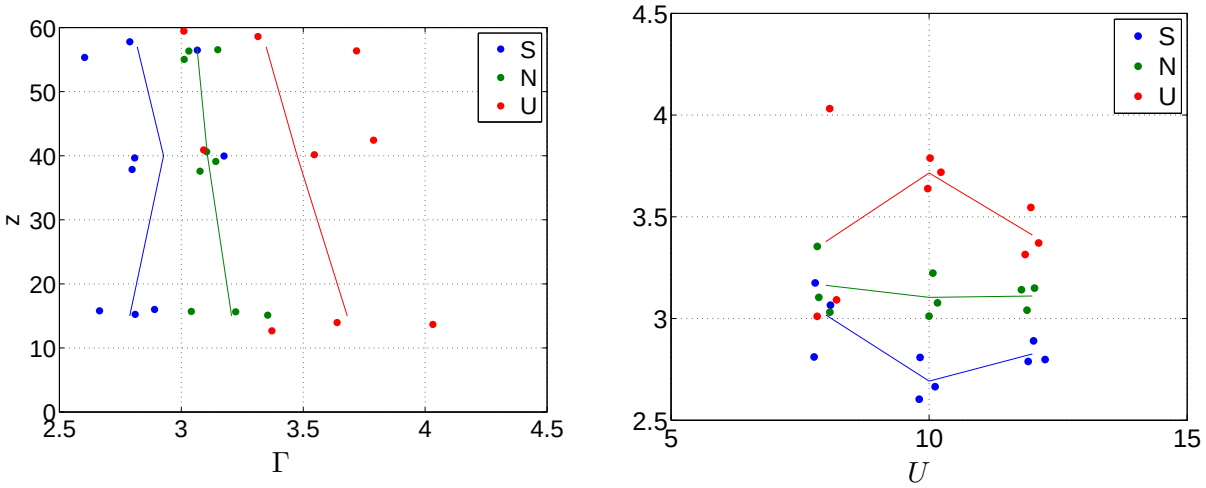


**Figure 5:** The parameter $\Gamma$ as a function of measurement height $z$ and wind speed $U$. A small random offset has been added to the measurement height and wind speed for readability. Note that the x-axis of the left plot is the y-axis of the right plot.

For $|\boldsymbol{k}|\, L_M \gg 1$ the hypergeometric function ${}_2\mathrm{F}_1\left(\frac{1}{3}, \frac{17}{6}, \frac{4}{3}, -|\boldsymbol{k}|^{-2} L_M^{-2}\right) \approx 1$. Thus for a $\boldsymbol{k}$ in the inertial subrange

$$\tau(|\boldsymbol{k}|) \approx \Gamma \left(\frac{\partial U}{\partial z}\right)^{-1} |\boldsymbol{k}|^{-2/3} L_M^{-2/3}. \tag{4}$$

Alternatively we can argue that, in the inertial subrange, $\tau$ should only be a function of $|\boldsymbol{k}|$ and the energy dissipation, $\epsilon$, which using dimensional analysis leads to

$$\tau(|\boldsymbol{k}|) \propto |\boldsymbol{k}|^{-2/3} \epsilon^{-1/3}. \tag{5}$$

Eliminating $\tau(|\boldsymbol{k}|)$ by combining (4) and (5) leads us to the conclusion that $\frac{\Gamma \epsilon^{1/3}}{\frac{\partial U}{\partial z}\, L_M^{2/3}}$ should be

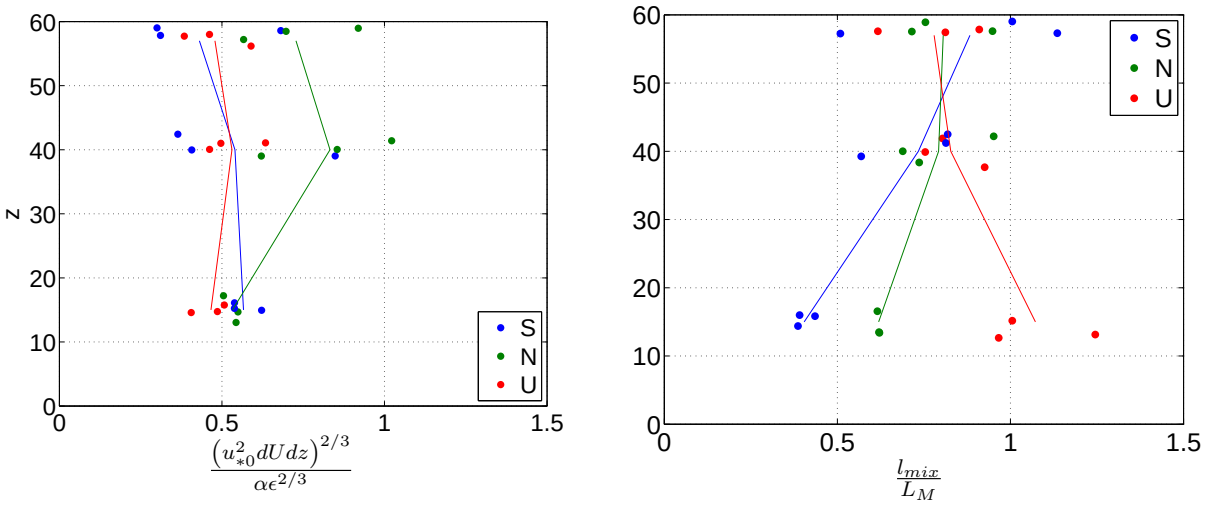


**Figure 6:** To the left, the quantity $\frac{\left(u_{*0}^2 \frac{\partial U}{\partial z}\right)^{2/3}}{\alpha\epsilon^{2/3}}$ which we expect to be approximately equal to $\frac{1}{\alpha} \approx 0.65$ versus measurement height. To the right the ratio $\frac{l_{mix}}{L_M}$ versus measurement height agrees reasonably but not perfectly with the $\frac{1}{1.70} \approx 0.59$ presented in [6]. A small random offset has been added to the measurement height.

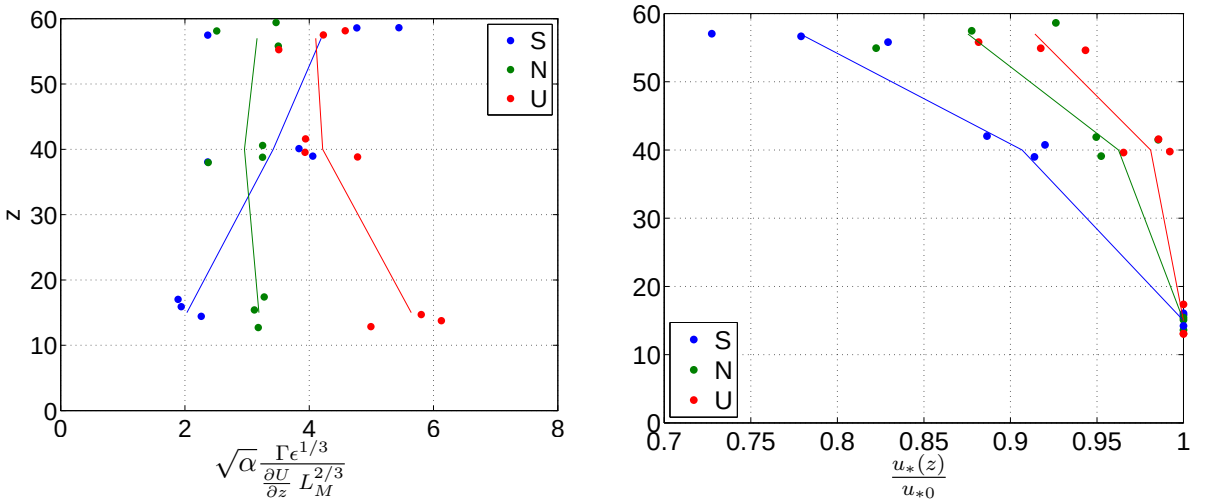


**Figure 7:** To the left the quantity $\sqrt{\alpha}\frac{\Gamma\epsilon^{1/3}}{\frac{\partial U}{\partial z} L_M^{2/3}}$, which we expect to be constant, plotted versus measurement height. If we focus exclusively on the Neutral case (green) then $\sqrt{\alpha}\frac{\Gamma\epsilon^{1/3}}{\frac{\partial U}{\partial z} L_M^{2/3}} \approx 3$. In the graph to the right $\frac{u_*(z)}{u_{*0}}$ versus measurement height illustrates that we are not generally measuring in the surface layer, as if so $u_*$ would be approximately constant. A small random offset has been added to the measurement height.

constant. In the left graph of figure 7 the quantity $\sqrt{\alpha}\frac{\Gamma\epsilon^{1/3}}{\frac{\partial U}{\partial z} L_M^{2/3}}$ is plotted versus measurement height. There is a lot of scatter in the graph but if we should assign a value we recommend $\sqrt{\alpha}\frac{\Gamma\epsilon^{1/3}}{\frac{\partial U}{\partial z} L_M^{2/3}} \approx 3$ as the neutral data is likely most reliable due to the method used to derive $\frac{\partial U}{\partial z}$. The graph to the right in figure 7 illustrates that we are not generally measuring in the surface

layer, and this could explain some of the scatter in figures 6 and 7 as they show results derived using $\frac{\partial U}{\partial z}$ which, as mentioned is calculated using a methodology suitable to the surface layer.

## 4. Conclusions

The parameter values giving the best fit of spectra calculated from the Mann spectral tensor to measured spectra was observed using data from the offshore meteorological mast at Rødsand II. Given optimal parameters the spectral tensor reproduces 3-dimensional turbulence contribution well, also for different atmospheric stabilities.

The results are consistent with what was observed in [1] and [6] except for the value of the parameter $\Gamma$ which here and in [1] decreases with stability, while [6] reports a more complex behavior.

It was argued that the quantity $\sqrt{\alpha}\frac{\Gamma\epsilon^{1/3}}{\frac{\partial U}{\partial z}L_M^{2/3}}$ should be constant and the value $\approx 3$ for was proposed for this constant.

At the low wavenumber end of the spectra a contribution from quasi-geostrophic turbulence was observed.

## References


[1] Abhijit S Chougule. *Influence of atmospheric stability on the spatial structure of turbulence*. DTU Wind Energy PhD-0028 (EN), 2013.

[2] Erik Lindborg. Can the atmospheric kinetic energy spectrum be explained by two-dimensional turbulence? *Journal of Fluid Mechanics*, 388:259–288, June 1999.

[3] Jakob Mann. The spatial structure of neutral atmospheric surface-layer turbulence. *Journal of Fluid Mechanics*, 273:141–168, April 1994.

[4] Jakob Mann. Wind field simulation. *Probabilistic Engineering Mechanics*, 13(4):269–282, October 1998.

[5] Andrei S Monin and Alexander M Obukhov. Basic laws of turbulent mixing in the surface layer of the atmosphere. 24(151):163–187, 1959.

[6] Alfredo Peña, Sven-Erik Gryning, and Jakob Mann. On the length-scale of the wind profile. *Quarterly Journal of the Royal Meteorological Society*, 136(653):2119–2131, October 2010.

[7] Katepalli R Sreenivasan. On the universality of the Kolmogorov constant. *Physics of Fluids (1994-present)*, 7(11), 1995.

[8] Ka Kit Tung, Wendell W Orlando, and Tyler Welch. On the differences between 2D and QG turbulence. *Discrete and continous dynamical systems - Series B*, 3(2):145–162, 2003.

# Paper D

**On the space-time structure of sheared turbulence**

Martin de Maré and Jakob Mann

*Accepted by Boundary-Layer Meteorology*

**Noname manuscript No.**
(will be inserted by the editor)

# On the space-time structure of sheared turbulence

**Martin de Maré · Jakob Mann**

Received: 2 May 2015 / Accepted: 23 February 2016

**Abstract** We develop a model that predicts all two-point correlations in high Reynolds number turbulent flow, in both space and time. This is accomplished by combining the design philosophies behind two existing models, the Mann spectral velocity tensor, in which isotropic turbulence is distorted according to rapid distortion theory, and Kristensen's longitudinal coherence model, in which eddies are simultaneously advected by larger eddies as well as decaying. The model is compared with data from both observations and large eddy simulations and is found to predict spatial correlations comparably to the Mann spectral tensor and temporal coherence better than any known model. Within the developed framework, Lagrangian two-point correlations in space and time are also predicted, and the predictions are compared with measurements of isotropic turbulence. The required input to the models, which are formulated as spectral velocity tensors, can be estimated from measured spectra or be derived from the rate of dissipation of turbulent kinetic energy, the friction velocity and the mean shear of the flow. The developed models can, for example, be used in wind turbine engineering, in applications such as lidar-assisted feed forward control and wind turbine wake modelling.

## 1 Introduction

Renewed interest in the spatio-temporal structure of sheared turbulence comes from research in wind energy, and whether forward-looking light detection and ranging (lidar) systems can reduce mechanical loads on wind turbines by anticipating incoming gusts (Pao and Johnson, 2011; Bossanyi et al., 2012;

M. de Maré
Wind Power, DONG Energy, Gentofte, Denmark
E-mail: mardm@dongenergy.dk

J. Mann
Wind Energy Department, Risø Campus, Technical University of Denmark (DTU), Denmark

Mikkelsen et al., 2013). The potential for both extreme and fatigue load reduction seems obvious, but to model the complex interactions between lidar-sensed turbulence and wind turbine control and aerodynamics it is necessary to have a realistic model for the spatio-temporal structure of turbulence (Bossanyi, 2013).

Most turbine-mounted lidars are placed close to the centre of the rotor, either on the nacelle or in the spinner, the aerodynamically shaped cover of the wind turbine rotor hub. Fluctuations along the direction of the mean flow constitute the most important turbulence component of the loads on the rotor. However, if a lidar is to measure these fluctuations over a rotor sized area upwind of the turbine, it would for geometrical reasons have to measure quite far upstream. The question arises whether the turbulent fluctuations measured there would arrive unchanged to the rotor a short time later, or equivalently, whether departures from Taylor's frozen turbulence hypothesis are important. For a nacelle-mounted lidar Simley et al. (2014) found that measurements made approximately one rotor diameter upstream reproduce most faithfully the gusts that impinge on the rotor. If measured further upstream, decorrelation during the advection to the rotor starts to become important. If measured closer to the rotor, fluctuations in directions other than along the mean flow will contaminate the measurements. Related questions pertain to how many beam directions will cover the rotor in an optimal way (Schlipf et al., 2013), and how the significant probe volume of the lidar influences the measurements (Sathe and Mann, 2013). All these issues depend on the spatial *and* temporal structure of sheared turbulence, the subject of the present study.

Wind turbine wakes are important not only because they affect the energy production adversely for downwind turbines in a wind farm but also because they increase dynamic loads on rotors intersecting them. Dynamic loads arise mainly because the blades of a downwind turbine partly in the wake of another, go in and out of the region with the wake velocity deficit. Another important effect is that wakes can meander such that the entire rotor of a downwind turbine alternately experiences unaffected flow and the reduced flow velocity of the wake. This typically creates dynamic loads that are greater than those on a free standing turbine. A popular way to model wake meandering assumes wakes to be advected passively in a frozen turbulence field (Larsen et al., 2008). A more realistic wake-meandering model may include the temporal evolution as well. Such a model would then likely require both the spatial *and* temporal structure of sheared turbulence as input.

Spatial correlations are tractable to describe in the Fourier domain by the use of a spectral velocity tensor (see e.g. Pope 2000). In Mann (1994), rapid distortion theory was employed to produce a spectral velocity tensor describing turbulence subjected to uniform shear. That model was recently tested over homogeneous terrain for different values of aerodynamic roughness length by Chougule et al. (2014) and for offshore conditions by de Maré and Mann (2014). Alternative rapid distortion formulations include a formulation with blocking effects from the ground also explored in Mann (1994), and for-

mulations including buoyancy effects, investigated e.g by Hanazaki and Hunt (2004) and Chougule (2013).

In Kristensen (1979), a model was developed to predict the correlation between two wind measurements separated in the streamwise direction. This model primarily predicts temporal correlations, and it has recently been implemented and used by Bossanyi (2013) in the context of lidar-assisted wind turbine control.

In Sect. 2, after first introducing definitions, we attempt to combine the design philosophy of the Mann (1994) tensor, in which isotropic turbulence is distorted by uniform shear, with the design philosophy of Kristensen (1979), in which eddies are simultaneously advected randomly by larger eddies as well as decaying. In Sect. 3, we discuss the implementation of the developed model as well as strategies for obtaining the necessary input information. Finally in Sect. 4, we compare the predictions of our model to data from experiments, data from large eddy simulations (LES) and where applicable, to the predictions of the Mann (1994) tensor.

Saffman (1963), Hunt et al. (1987), and more recently Wilczek and Narita (2012) and Wilczek et al. (2014), suggested the temporal evolution of the velocity tensor to be given by wavenumber-dependent Gaussian functions. A number of such models were evaluated for isotropic turbulence in Ott and Mann (2005). As the validation section includes comparisons with those same experiments, comparisons with the models evaluated in Ott and Mann (2005) are implicitly made.

## 2 Modelling

### 2.1 Preliminaries

It is common to assume statistical stationarity (as well as ergodicity) and decompose the three-dimensional flow velocity, $\tilde{\boldsymbol{u}}(\boldsymbol{x},t)$, into a mean velocity, $\boldsymbol{U}(\boldsymbol{x})$, and a fluctuating part, $\boldsymbol{u}(\boldsymbol{x},t)$. We define the coordinate system to move with a suitable velocity, $\boldsymbol{U_0}$, so that in our coordinate system $\boldsymbol{U}(\boldsymbol{0}) = 0$. We further assume a constant and non-negative shear, $\mathrm{d}U_1/\mathrm{d}z$, such that

$$\tilde{\boldsymbol{u}}(\boldsymbol{x},t) = \boldsymbol{U}(\boldsymbol{x}) + \boldsymbol{u}(\boldsymbol{x},t) = (x_3\frac{\mathrm{d}U_1}{\mathrm{d}z},0,0) + \boldsymbol{u}(\boldsymbol{x},t), \tag{1}$$

where $z$ and $x_3$ are used interchangeably. Provided that $\boldsymbol{u}(\boldsymbol{x},t)$ is statistically homogeneous, we can define a covariance tensor

$$R_{ij}(\boldsymbol{r},\tau) = \langle u_i(\boldsymbol{x},t)\, u_j(\boldsymbol{x}+\boldsymbol{r}+\boldsymbol{U}(\boldsymbol{x}+\boldsymbol{r})\tau, t+\tau)\rangle\,. \tag{2}$$

In (2) we have accounted for the mean velocity of the flow varying with height by introducing the term $\boldsymbol{U}(\boldsymbol{x}+\boldsymbol{r})\tau$, thereby modifying the traditional definition of the covariance tensor. The role of this term is easiest to demonstrate for $\boldsymbol{r} = 0$, when it causes the right-hand side of (2) to denote the covariance at a point that moves with the mean flow velocity, $\boldsymbol{U}(\boldsymbol{x})$. The spectral velocity

tensor (or velocity-spectrum tensor), $\widehat{R}_{ij}$, is the spatial Fourier transform of (2),

$$\widehat{R}_{ij}(\boldsymbol{k},\tau) = \frac{1}{(2\pi)^3}\iiint R_{ij}(\boldsymbol{r},\tau)\,\mathrm{e}^{-\mathrm{i}\,\boldsymbol{k}\cdot\boldsymbol{r}}\,\mathrm{d}^3\boldsymbol{r}, \tag{3}$$

where $\mathrm{d}^3\boldsymbol{r} = \mathrm{d}r_1\,\mathrm{d}r_2\,\mathrm{d}r_3$. From the spectral velocity tensor a number of quantities can be derived, for example the (one-dimensional) spatial cross-spectrum

$$\begin{aligned}\chi_{ij}(k_1,\boldsymbol{r},\tau) &= \frac{1}{2\pi}\int R_{ij}((\xi_1,0,0)+\boldsymbol{r},\tau)\,\mathrm{e}^{-\mathrm{i}\,k_1\,\xi_1}\,\mathrm{d}\xi_1 \\ &= \iint_{\kappa_1=k_1} \widehat{R}_{ij}(\boldsymbol{\kappa},\tau)\,\mathrm{e}^{\mathrm{i}\,\boldsymbol{\kappa}\cdot\boldsymbol{r}}\,\mathrm{d}^2\boldsymbol{\kappa},\end{aligned} \tag{4}$$

and the closely related quantity

$$\mathring{\chi}_{ij}(k) = \iint_{|\boldsymbol{\kappa}|=k} \widehat{R}_{ij}(\boldsymbol{\kappa},0)\,\mathrm{d}^2\boldsymbol{\kappa}. \tag{5}$$

From the spatial cross-spectra the spatial spectral coherence is in turn derived as

$$\mathrm{coh}_{ij}(k_1,\boldsymbol{r},\tau) = \frac{|\chi_{ij}(k_1,\boldsymbol{r},\tau)|^2}{\chi_{ii}(k_1,\boldsymbol{r},0)\chi_{jj}(k_1,\boldsymbol{r},0)}, \tag{6}$$

where, as our only exception, no summation over repeated indices is intended.

Batchelor (1953) used a generalized stochastic Fourier-Stieltjes decomposition of the fluctuating part of the wind velocity, however, as we find this notation somewhat unintuitive we use the less stringent notation

$$\boldsymbol{u}(\boldsymbol{x},t) = \iiint \widehat{\boldsymbol{u}}(\boldsymbol{k},t)\,\mathrm{e}^{\mathrm{i}\,\boldsymbol{k}\cdot\boldsymbol{x}}\,\mathrm{d}^3\boldsymbol{k}. \tag{7}$$

We find that

$$\begin{aligned}&\boldsymbol{u}\Big((x_1 + x_3\frac{\mathrm{d}U_1}{\mathrm{d}z}\tau, x_2, x_3), t+\tau\Big) \\ &= \iiint \widehat{\boldsymbol{u}}(\boldsymbol{\kappa},t+\tau)\,\mathrm{e}^{\mathrm{i}\,\boldsymbol{\kappa}\cdot\,(x_1+x_3\frac{\mathrm{d}U_1}{\mathrm{d}z}\tau,x_2,x_3)}\,\mathrm{d}^3\boldsymbol{\kappa} \\ &= \iiint \widehat{\boldsymbol{u}}\Big((k_1,k_2,k_3-\frac{\mathrm{d}U_1}{\mathrm{d}z}\tau\,k_1),t+\tau\Big)\,\mathrm{e}^{\mathrm{i}\,\boldsymbol{k}\cdot\boldsymbol{x}}\,\mathrm{d}^3\boldsymbol{k},\end{aligned} \tag{8}$$

where in the last step the variable transformation

$$\boldsymbol{\kappa} = (\kappa_1,\kappa_2,\kappa_3) = (k_1,k_2,k_3-\frac{\mathrm{d}U_1}{\mathrm{d}z}\tau\,k_1) \tag{9}$$

has been used. Combining (8) with (2) and (3) it is possible to show that

$$\widehat{R}_{ij}(\boldsymbol{k},\tau) = \left\langle \widehat{u}_i(\boldsymbol{k},t)\overline{\widehat{u}_j(\boldsymbol{k}(\tau),t+\tau)}\,\mathrm{d}^3\boldsymbol{k}\right\rangle, \tag{10}$$

where we have introduced notation for complex conjugation, and $\boldsymbol{k}(\tau)$ has been introduced as

$$\boldsymbol{k}(\tau) = (k_1, k_2, k_3 - \frac{\mathrm{d}U_1}{\mathrm{d}z}\tau\, k_1). \tag{11}$$

Formulating a model for $\widehat{R}_{ij}(\boldsymbol{k}, \tau)$ is one of our goals. For comparison, Mann (1994) developed a model for $\widehat{R}_{ij}(\boldsymbol{k}, 0)$ and Kristensen (1979) developed a model for $\mathrm{coh}_{11}(k_1, \boldsymbol{0}, \tau)$. We are also interested in the Lagrangian covariance tensor defined by

$$R^{\mathrm{L}}_{ij}(\boldsymbol{r}, \tau) = \left\langle u_i(\boldsymbol{x}, t_0)\, u_j\left(\boldsymbol{X}^{\mathrm{L}}_{t_0}(\boldsymbol{x} + \boldsymbol{r}, t_0 + \tau), t_0 + \tau\right)\right\rangle, \tag{12}$$

where $\boldsymbol{X}^{\mathrm{L}}_{t_0}(\boldsymbol{x}, t)$ is the position at time $t$ of a fluid particle, which at $t_0$ was located at $\boldsymbol{x}$. Therefore we also attempt to model the Lagrangian spectral velocity tensor defined through

$$\widehat{R}^{\mathrm{L}}_{ij}(\boldsymbol{k}, \tau) = \frac{1}{(2\pi)^3} \iiint R^{\mathrm{L}}_{ij}(\boldsymbol{r}, \tau)\, \mathrm{e}^{-\mathrm{i}\,\boldsymbol{k}\cdot\boldsymbol{r}}\, \mathrm{d}^3\boldsymbol{r}. \tag{13}$$

We will frequently sacrifice physical realism for mathematical tractability. One such example is our assumption of constant shear, which in reality would create infinitely large turbulent eddies. This particular problem is handled by having a turbulent length scale as a model input. Due to such simplifications, in the end, it will be the prediction capabilities of the final models that determine their applicability.

## 2.2 Analysis of eddy decay

The focus here is the evolution of turbulent eddies in the presence of vertical shear, excluding turbulent advection of small-scale eddies by larger eddies, a topic we address instead in the next section. We start from the rapid distortion equation for sheared flow derived by Moffatt (1967) and Townsend (1976),

$$\frac{\mathrm{D}\,\widehat{u}_i(\boldsymbol{k}(t), t)}{\mathrm{D}\,t} = \frac{\mathrm{d}U_1}{\mathrm{d}z}\left(-\delta_{i1} + 2\frac{k_i k_1}{|\boldsymbol{k}(t)|^2}\right)\widehat{u}_3(\boldsymbol{k}(t), t), \tag{14}$$

where

$$\boldsymbol{k}(t) = (k_1, k_2, k_{30} - k_1 \frac{\mathrm{d}U_1}{\mathrm{d}z}\,(t - t_0)). \tag{15}$$

Equation 14 does not include any term for buoyancy effects, so the results may or may not be valid for non-neutral atmospheric stratification. More elaborate rapid distortion formulations are in use (Kaneda and Ishida, 2000; Hanazaki and Hunt, 2004; Salhi and Cambon, 2010; Chougule, 2013), however, we stay with the above version for now.

In Fig. 1 we show a sequence of snapshots of conceptual turbulence; the sequence of snapshots is continued in Fig. 2, in which the dashed black lines illustrate the distortion of a sample wavenumber according to (15).

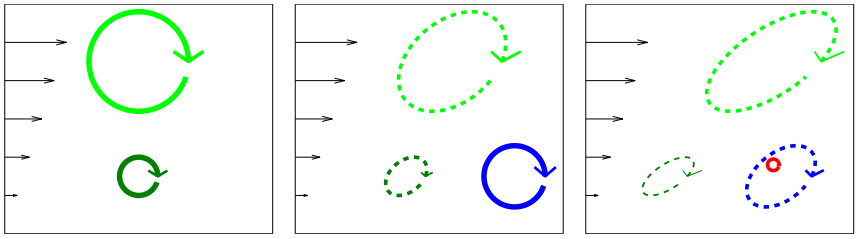

**Fig. 1** The three frames show a sequence of snapshots of conceptual turbulence being distorted by shear (illustrated by the black arrows). The two green eddies are being distorted (from circles to ellipses) by the shear while at the same time decaying (illustrated by the shift from solid lines to dashed lines). We note that the smaller, dark green, eddy appears to decay more rapidly than the larger, light green, eddy. We also note the newborn blue and red eddies in the middle and right-most frames, respectively.

We now write $\widehat{\boldsymbol{u}}(\boldsymbol{k},t)$ as

$$\widehat{\boldsymbol{u}}(\boldsymbol{k},t)=\int_{-\infty}^{t}\boldsymbol{\eta}(\boldsymbol{k}_0,t_0,t-t_0)\,\mathrm{d}t_0, \tag{16}$$

where we have introduced $\boldsymbol{\eta}(\boldsymbol{k}_0,t_0,t-t_0)\,\mathrm{d}t_0$ as the contribution to $\widehat{\boldsymbol{u}}(\boldsymbol{k},t)$ from eddies that were created between $t_0$ and $t_0+\mathrm{d}t_0$. The newborn eddies in Fig. 1 would thus contribute to different $\boldsymbol{\eta}$ than the older eddies in the same frames. In (16) $\boldsymbol{k}_0$ is derived from $\boldsymbol{k}$ by inverting (15),

$$\boldsymbol{k}_0=(k_1,k_2,k_{30})=\left(k_1,k_2,k_3+k_1\frac{\mathrm{d}U_1}{\mathrm{d}z}\,(t-t_0)\right). \tag{17}$$

It follows from homogeneity that for a fixed $t$, the $\boldsymbol{\eta}$'s contributing to *different* wavenumbers are uncorrelated. We, however, go beyond homogeneity and postulate that

$$\left\langle \eta_i(\boldsymbol{k}_0,t_0,t-t_0)\overline{\eta_j(\boldsymbol{\kappa}_0,\tau_0,t-\tau_0+\tau)}\,\mathrm{d}^3\boldsymbol{k}\,\mathrm{d}t_0\right\rangle=0 \tag{18}$$

unless $\tau_0=t_0$ and $\boldsymbol{\kappa}_0=\boldsymbol{k}_0$. This assumption reduces our objective of determining $\widehat{R}_{ij}$, to quantifying

$$\left\langle \eta_i(\boldsymbol{k}_0,t_0,t-t_0)\overline{\eta_j(\boldsymbol{k}_0,t_0,t-t_0+\tau)}\,\mathrm{d}^3\boldsymbol{k}\,\mathrm{d}t_0\right\rangle, \tag{19}$$

as we can then use (10) and (16) to find $\widehat{R}_{ij}$. Direct validation of (18) would require isolating the contribution of newly formed eddies, from the contributions of older eddies, an objective that may be challenging, to say the least, in practice.

We introduce the expected contribution from newborn eddies,

$$N_{ij}(\boldsymbol{k}_0)=\left\langle \eta_i(\boldsymbol{k}_0,t_0,0)\overline{\eta_j(\boldsymbol{k}_0,t_0,0)}\,\mathrm{d}^3\boldsymbol{k}\,\mathrm{d}t_0\right\rangle, \tag{20}$$

which is constant in time due to stationarity. As the eddies are expected to decay over time the contributions cannot, however, be expected to be statistically stationary with respect to $t - t_0$.

Townsend (1976) suggested that the time evolution of an eddy can be described as a superposition of rapid distortion and viscous decay. Inspired by this argument and Mann (1994) we introduce a term where the eddy viscosity depends on $\boldsymbol{k}(t)$ into the rapid distortion equation. Continuing to disregard advection by larger eddies, we thus postulate that the contributions, $\boldsymbol{\eta}$, evolve in time according to the deterministic equation,

$$\begin{aligned}\frac{\mathrm{D}\,\eta_i(\boldsymbol{k}_0, t_0, t-t_0)}{\mathrm{D}\,t} = \frac{\mathrm{d}U_1}{\mathrm{d}z}\left(-\delta_{i1} + 2\frac{k_i k_1}{|\boldsymbol{k}(t)|^2}\right)\eta_3(\boldsymbol{k}_0, t_0, t-t_0) \\ - \frac{1}{2\,\tau_e(\boldsymbol{k}(t))}\eta_i(\boldsymbol{k}_0, t_0, t-t_0),\end{aligned} \tag{21}$$

where the eddy viscosity term is the last term on the right-hand side. We will refer to the process described by (21) as eddy decay.

For the isotropic case, where $\mathrm{d}U_1/\mathrm{d}z = 0$ and therefore $\boldsymbol{k}(t) = \boldsymbol{k}_0$, the solution to (21) is simply

$$\boldsymbol{\eta}^{\mathrm{ISO}}(\boldsymbol{k}_0, t_0, t-t_0) = \boldsymbol{\eta}^{\mathrm{ISO}}_{t_0}(\boldsymbol{k}_0, t_0, 0)\exp\left(-\frac{t-t_0}{2\,\tau_e(\boldsymbol{k}_0)}\right). \tag{22}$$

From this solution it can be seen that the expected lifetime of the energy of eddies created at the same time is

$$\begin{aligned}\frac{\int_{t=t_0}^{\infty}\boldsymbol{\eta}^{\mathrm{ISO}}(\boldsymbol{k}_0, t_0, t-t_0)\cdot\overline{\boldsymbol{\eta}^{\mathrm{ISO}}(\boldsymbol{k}_0, t_0, t-t_0)}\,\mathrm{d}t}{\boldsymbol{\eta}^{\mathrm{ISO}}(\boldsymbol{k}_0, t_0, 0)\cdot\overline{\boldsymbol{\eta}^{\mathrm{ISO}}(\boldsymbol{k}_0, t_0, 0)}} &= \int_{t=t_0}^{\infty}\mathrm{e}^{-\frac{t-t_0}{2\,\tau_e(\boldsymbol{k})}}\,\mathrm{e}^{-\frac{t-t_0}{2\,\tau_e(\boldsymbol{k})}}\,\mathrm{d}t \\ &= \tau_e(\boldsymbol{k}).\end{aligned} \tag{23}$$

Based on (23) we refer to $\tau_e(\boldsymbol{k})$ as the eddy lifetime, even though this is not an entirely accurate term when $\mathrm{d}U_1/\mathrm{d}z \neq 0$. In Fig. 1 we have illustrated the dependence of $\tau_e$ on $\boldsymbol{k}$ by the smaller eddies decaying more rapidly than the large ones.

The general solution to (21) can be written

$$\boldsymbol{\eta}(\boldsymbol{k}_0, t_0, t-t_0) = \boldsymbol{B}(\boldsymbol{k}_0, t-t_0)\,\boldsymbol{\eta}(\boldsymbol{k}_0, t_0, 0), \tag{24}$$

where

$$\boldsymbol{B}(\boldsymbol{k}_0, t-t_0) = \mathrm{e}^{-(\Omega(\boldsymbol{k}_0, t-t_0)-\Omega(\boldsymbol{k}_0,0))}\begin{bmatrix}1 & 0 & \zeta_1\left(\boldsymbol{k}_0, \frac{\mathrm{d}U_1}{\mathrm{d}z}(t-t_0)\right) \\ 0 & 1 & \zeta_2\left(\boldsymbol{k}_0, \frac{\mathrm{d}U_1}{\mathrm{d}z}(t-t_0)\right) \\ 0 & 0 & |\boldsymbol{k}_0|^2/|\boldsymbol{k}(t)|^2\end{bmatrix}, \tag{25}$$

and where in turn $\zeta_1(\boldsymbol{k}_0, \beta)$ and $\zeta_2(\boldsymbol{k}_0, \beta)$, derived in Mann (1994) and Townsend (1976), are

$$\begin{aligned}\zeta_1(\boldsymbol{k}_0, \beta) = &\frac{\beta k_1^2 \left( |\boldsymbol{k}_0|^2 - 2k_{30}^2 + \beta k_1 k_{30} \right)}{|\boldsymbol{k}(t)|^2 \left(k_1^2 + k_2^2\right)} \\ &- \frac{k_2^2 |\boldsymbol{k}_0|^2}{k_1 \left(k_1^2 + k_2^2\right)^{3/2}} \arctan\left( \frac{\beta k_1 \left(k_1^2 + k_2^2\right)^{1/2}}{|\boldsymbol{k}_0|^2 - \beta k_1 k_{30}} \right),\end{aligned} \tag{26}$$

$$\begin{aligned}\zeta_2(\boldsymbol{k}_0, \beta) = &\frac{k_2 \beta k_1 \left( |\boldsymbol{k}_0|^2 - 2k_{30}^2 + \beta k_1 k_{30} \right)}{|\boldsymbol{k}(t)|^2 \left(k_1^2 + k_2^2\right)} \\ &+ \frac{k_2 |\boldsymbol{k}_0|^2}{\left(k_1^2 + k_2^2\right)^{3/2}} \arctan\left( \frac{\beta k_1 \left(k_1^2 + k_2^2\right)^{1/2}}{|\boldsymbol{k}_0|^2 - \beta k_1 k_{30}} \right)\end{aligned} \tag{27}$$

and $\Omega(\boldsymbol{k}_0, t - t_0)$ has been introduced such that

$$\frac{\partial \Omega(\boldsymbol{k}_0, t - t_0)}{\partial t} = \frac{1}{2\, \tau_e(\boldsymbol{k}(t))}. \tag{28}$$

For comparison, in Mann (1994) the eddies are not continuously decaying. Instead the eddy lifetime, $\tau_e(\boldsymbol{k})$, is used as the typical time the eddies contributing to $\boldsymbol{k}$ have been subjected to the rapid distortion.

We end by noting that eddy decay can be applied sequentially, i.e that

$$B_{im}(\boldsymbol{k}(t), \tau)\, B_{mj}(\boldsymbol{k}_0, t - t_0) = B_{ij}(\boldsymbol{k}_0, t - t_0 + \tau). \tag{29}$$

### 2.3 Modelling advection by larger eddies

Kristensen (1979) attributed loss of longitudinal coherence to a combination of eddies decaying, and large eddies advecting smaller eddies, causing them to miss the downstream anemometer. The latter process, which is not captured by rapid distortion theory, is illustrated in Fig. 2. A straightforward way of modelling this advection by larger eddies, is to assume that an eddy moves as a suitably sized sphere. To be more exact, let us assume that an eddy with a size corresponding to wavenumbers of magnitude $k$, positioned at $\boldsymbol{x}$ at time $t$, has a velocity $u_i^{R_k}(\boldsymbol{x}, t)$, which is the average velocity over a sphere with radius $R_k$, i.e.,

$$u_i^{R_k}(\boldsymbol{x}, t) = \frac{\iiint_{|\boldsymbol{r}|<R_k} u_i(\boldsymbol{x} + \boldsymbol{r}, t)\, \mathrm{d}^3\boldsymbol{r}}{\frac{4}{3}\pi R_k^3}. \tag{30}$$

Assuming that eddies move like spheres may not be entirely realistic because a sphere ends with a well-defined edge whereas an eddy most likely does not. It can also be argued that owing to eddy decay the shape of a typical eddy would be better represented by an ellipsoid, rather than by a sphere.

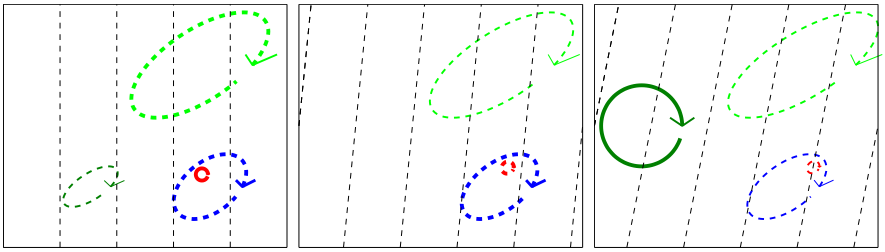

**Fig. 2** The three frames are a continuation of the sequence of conceptual turbulence in Fig. 1. The left-most frame is identical to the last frame of Fig. 1, except that the shear is now illustrated by the dashed black lines which represent a wavenumber evolving according to $\boldsymbol{k}(\tau) = (k_1, k_2, k_3 - \frac{\mathrm{d}U_1}{\mathrm{d}z}\tau\, k_1)$. In the two right-most frames we notice that the blue eddy advects the smaller red eddy, causing it to move relative to the illustrated wavenumber.

If we, inspired by (3), were to define a spectral velocity tensor based on the averaged wind velocity of (30) we would, for $\tau = 0$, get

$$\widehat{R}_{ij}^{R_k}(\boldsymbol{\kappa}, 0) = \mathrm{H}_k^2(|\boldsymbol{\kappa}|)\widehat{R}_{ij}(\boldsymbol{\kappa}, 0). \tag{31}$$

In (31),

$$\mathrm{H}_k(\kappa) = -3\frac{\kappa R_k \cos(\kappa R_k) - \sin(\kappa R_k)}{\kappa^3 R_k^3} \tag{32}$$

is the Fourier transform of the "averaging sphere" convolution kernel, which, we may add, effectively acts as a low-pass filter. The right-hand side of (32) is a scaled version of the Bessel function $J_{3/2}(x)$. Based on the argument that eddies do not advect themselves, we select $R_k$ such that $kR_k$ equals the first zero of $J_{3/2}(x)$, i.e.

$$R_k \approx \frac{4.4934}{k}. \tag{33}$$

We note that $R_k = \frac{\pi}{k}$ or $R_k = \frac{\pi}{2k}$ would be just as natural choices as (33). We will briefly return to this topic when discussing the cross-over point of Eulerian and Lagrangian covariances in Sect. 4.2.

From $\widehat{R}_{ij}^{R_k}(\boldsymbol{\kappa}, 0)$ in (31) we can, among many other quantities, derive the standard deviation of $u_i^{R_k}(\boldsymbol{x}, t)$ along any vector. We take the opportunity to introduce, $s(\boldsymbol{k})$, the standard deviation of the velocity of the eddies with radius $R_{|\boldsymbol{k}|}$, in the direction of $\boldsymbol{k}$,

$$s(\boldsymbol{k}) = \sqrt{\left\langle \frac{k_i k_j}{|\boldsymbol{k}|^2} u_i^{R_{|\boldsymbol{k}|}}(\boldsymbol{x}, t) u_j^{R_{|\boldsymbol{k}|}}(\boldsymbol{x}, t) \right\rangle} = \sqrt{\iiint \frac{k_i k_j}{|\boldsymbol{k}|^2} \mathrm{H}_{|\boldsymbol{k}|}^2(|\boldsymbol{\kappa}|)\widehat{R}_{ij}(\boldsymbol{\kappa}, 0)\, \mathrm{d}^3\boldsymbol{\kappa}} =$$

$$= \sqrt{\int_0^\infty \frac{k_i k_j}{|\boldsymbol{k}|^2} \mathrm{H}_{|\boldsymbol{k}|}^2(\kappa)\mathring{\chi}_{ij}(\kappa)\, \mathrm{d}\kappa}. \tag{34}$$

Now, let us again consider the blue eddy in Fig. 2. If we denote the illustrated wavenumber $\boldsymbol{k}(t)$ and assume that $R_{|\boldsymbol{k}|}$ happens to be the characteristic

size of the blue eddy, then, according our definitions, the blue eddy moves with a velocity

$$v_{\text{blue}}(t) = \frac{k_i}{|\boldsymbol{k}(t)|} u_i^{R_{|\boldsymbol{k}|}}(\boldsymbol{x}_{\text{blue}}(t), t), \tag{35}$$

in the direction of $\boldsymbol{k}(t)$, i.e. perpendicular to the dashed black lines. If the blue eddy was the only eddy described by $\boldsymbol{\eta}(\boldsymbol{k}_0, t_0, t - t_0)$, then $\boldsymbol{\eta}(\boldsymbol{k}_0, t_0, t - t_0 + \tau)$ would be equal to

$$\boldsymbol{B}(\boldsymbol{k}, \tau)\boldsymbol{\eta}(\boldsymbol{k}_0, t_0, t - t_0)\, \mathrm{e}^{-\mathrm{i}\,\phi_{\text{blue}}(\tau)}, \tag{36}$$

with $\phi_{\text{blue}}(\tau)$ the "distance travelled in radians" given by

$$\phi_{\text{blue}}(\tau) = \int_t^{t+\tau} v_{\text{blue}}(\tau')|\boldsymbol{k}(\tau')|\mathrm{d}\tau'. \tag{37}$$

Now, $\boldsymbol{\eta}(\boldsymbol{k}_0, t_0, t - t_0)$ does not only represent the blue eddy, but all eddies of approximately the same size and age as the blue eddy. Equation 34 introduced the standard deviation of the velocity of these eddies in the direction of $\boldsymbol{k}$, as $s(\boldsymbol{k})$, and we assume that $s(\boldsymbol{k})$, analogously to (37), can be integrated to give the standard deviation of the distance in radians travelled by the eddies,

$$\Theta(\boldsymbol{k}, \tau) = \int_t^{t+\tau} s(\boldsymbol{k}(\tau'))|\boldsymbol{k}(\tau')|\mathrm{d}\tau'. \tag{38}$$

We further assume that the distances in radians travelled by the eddies in question are normally distributed,

$$\frac{1}{\Theta(\boldsymbol{k}, \tau)\sqrt{2\pi}} \exp\left(-\frac{\phi^2}{2\Theta^2(\boldsymbol{k}, \tau)}\right), \tag{39}$$

a choice supported by the fact that this distribution has maximal entropy for given first and second moments. Combining (36) with (39) leads to

$$\begin{aligned}
&\left\langle \eta_i(\boldsymbol{k}_0, t_0, t - t_0)\overline{\eta_j(\boldsymbol{k}_0, t_0, t - t_0 + \tau)}\, \mathrm{d}^3\boldsymbol{k}\, \mathrm{d}t_0 \right\rangle \\
&= \left\langle \eta_i(\boldsymbol{k}_0, t_0, t - t_0)\left(\overline{\int_{-\infty}^{\infty} \frac{1}{\Theta(\boldsymbol{k}, \tau)\sqrt{2\pi}}\, \mathrm{e}^{-\frac{\phi^2}{2\Theta^2(\boldsymbol{k}, \tau)}}\, B_{jn}(\boldsymbol{k}, \tau)} \right.\right. \\
&\qquad \left.\left. \overline{\eta_j(\boldsymbol{k}_0, t_0, t - t_0 + \tau)\, \mathrm{e}^{-\,i\phi(\tau)}\, \mathrm{d}\phi}\right) \mathrm{d}^3\boldsymbol{k}\, \mathrm{d}t_0 \right\rangle \\
&= \left\langle \eta_m(\boldsymbol{k}_0, t_0, t - t_0)\overline{\mathrm{e}^{-\frac{1}{2}\Theta^2(\boldsymbol{k}, \tau)}\, B_{jn}(\boldsymbol{k}, \tau)\eta_n(\boldsymbol{k}_0, t_0, t - t_0)}\, \mathrm{d}^3\boldsymbol{k}\, \mathrm{d}t_0 \right\rangle \\
&= \mathrm{e}^{-\frac{1}{2}\Theta^2(\boldsymbol{k}, \tau)}\, B_{im}(\boldsymbol{k}_0, t - t_0)N_{mn}(\boldsymbol{k}_0)B_{jn}(\boldsymbol{k}_0, t + \tau - t_0),
\end{aligned} \tag{40}$$

where in the last step we have used (20) and (29). The last line of (40) describes newborn eddies, $N_{mn}(\boldsymbol{k}_0)$, which, since their birth at $t_0$, have been subjected to eddy decay, $B_{ij}(\boldsymbol{k}_0, t - t_0)$. Moreover, if observed twice, at $t$ and $t + \tau$, advection by larger eddies has caused unalignment resulting in a loss of correlation according to $\exp\left(-\frac{1}{2}\Theta^2(\boldsymbol{k}, \tau)\right)$.

We can now, using (10), (16), (18) and (40), derive an expression for $\widehat{R}_{ij}(\boldsymbol{k},\tau)$,

$$\begin{aligned}\widehat{R}_{ij}(\boldsymbol{k},\tau) &= \left\langle \widehat{u}_i(\boldsymbol{k},t)\,\overline{\widehat{u}_j(\boldsymbol{k}(\tau),t+\tau)}\,\mathrm{d}^3\boldsymbol{k}\right\rangle \\ &= \left\langle \int_{-\infty}^{t}\eta_i(\boldsymbol{k},\xi_0,t-\xi_0)\,\mathrm{d}\xi_0\int_{-\infty}^{t}\overline{\eta_j(\boldsymbol{k}_\tau,\zeta_0,t-\zeta_0)}\,\mathrm{d}\zeta_0\,\mathrm{d}^3\boldsymbol{k}\right\rangle \\ &= \int_{-\infty}^{t}\left\langle \eta_i(\boldsymbol{k}_0,t_0,t-t_0)\overline{\eta_j(\boldsymbol{k}_0,t_0,t+\tau-t_0)}\,\mathrm{d}^3\boldsymbol{k}\,\mathrm{d}t_0\right\rangle \mathrm{d}t_0 \\ &= \int_{-\infty}^{t}\mathrm{e}^{-\frac{1}{2}\Theta^2(\boldsymbol{k},\tau)}\,B_{im}(\boldsymbol{k}_0,t-t_0)N_{mn}(\boldsymbol{k}_0)B_{jn}(\boldsymbol{k}_0,t+\tau-t_0)\,\mathrm{d}t_0,\end{aligned} \tag{41}$$

where $\boldsymbol{k}_0$ and and $\Theta(\boldsymbol{k},\tau)$ are given by (17) and (38), respectively. We note that $\Theta(\boldsymbol{k},\tau)$ by definition is equal to 0 for $\tau = 0$ and it is therefore not a problem that $\widehat{R}_{ij}(\boldsymbol{k},0)$ is used, through the definition of $s(\boldsymbol{k})$, to define $\Theta(\boldsymbol{k},\tau)$. Owing to stationarity, the right-hand side of (41) does not depend on the value of $t$.

We cannot evaluate (41) numerically just yet because we have neither introduced an expression for the eddy lifetime nor an expression for the added energy due to newborn eddies, $N_{ij}(\boldsymbol{k}_0)$. Before addressing these needs, we turn our attention to the Lagrangian covariance tensor, $\widehat{R}^{\mathrm{L}}_{ij}$, defined in (13).

### 2.4 A model for the Lagrangian tensor

The Lagrangian approach can be described as observing the flow by tracking fluid particles and recording their instantaneous velocities. If we follow one of the fluid particles within the small red eddy of Fig. 2 and use it to study the wavenumber illustrated by the dashed black lines, then it is clear that the Lagrangian velocity may lose coherence even when, as in this case, the blue eddy (which likely contributes to the illustrated wavenumber) stays more or less coherent. Our assumption is therefore that the evolution of the Lagrangian tensor is a combination of eddy decay and the fluid particles moving relative to the eddies of which they are a part.

If we want to quantify the movement of a point within the small red eddy, relative to the red eddy itself, then the fact that the blue eddy is advecting both the red eddy and our observation particle should be of little importance. Similarly, if we are interested in the point's movement, relative to the *blue* eddy, then the fact that it is also moving within the small red eddy likely has limited impact. Based on these arguments we quantify the velocity of a particle relative to an eddy of size $R_{|\boldsymbol{k}|}$, as the velocity of the particle minus *both* the velocity contribution from eddies that are large enough to move the eddy of interest, $\mathrm{H}_{|\boldsymbol{k}|}(|\boldsymbol{\kappa}|)\widehat{u}_i(\boldsymbol{\kappa},0)$, *and* the velocity contribution from eddies that are small enough to be moved by the eddy of interest, $\mathrm{H}_{|\boldsymbol{\kappa}|}(|\boldsymbol{k}|)\widehat{u}_{ij}(\boldsymbol{\kappa},0)$. The

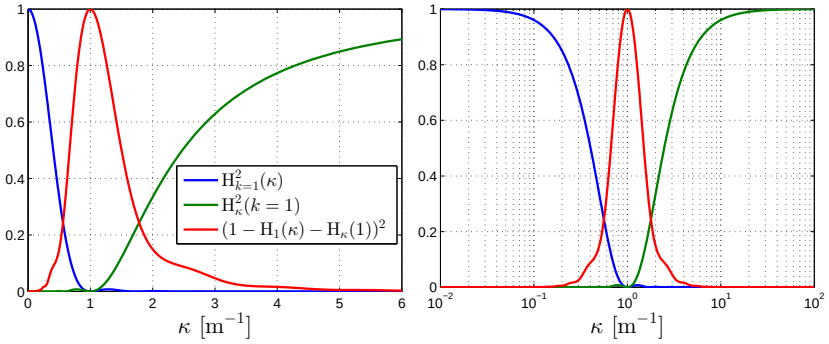


**Fig. 3** The velocity of a particle relative to an eddy of size $R_{|\boldsymbol{k}|=1}$ is quantified as the velocity of the particle minus *both* the velocity contribution from eddies that are large enough to move the eddy of interest, $\mathrm{H}_{|\boldsymbol{k}|=1}(|\boldsymbol{\kappa}|)\widehat{u}_i(\boldsymbol{\kappa},0)$, *and* the velocity contribution from eddies that are small enough to be moved by the eddy of interest, $\mathrm{H}_{|\boldsymbol{\kappa}|}(|\boldsymbol{k}|=1)\widehat{u}_i(\boldsymbol{\kappa},0)$. The resulting factor $(1-\mathrm{H}_1(\kappa)-\mathrm{H}_\kappa(1))^2$ is illustrated (in red) versus a linear as well as a logarithmic $\kappa$. We note that the choice of expression for $R_k$ in (33) ensures that $\mathrm{H}_1(\kappa)=0$ for $\kappa=1$.

standard deviation of the velocity with which a fluid particle moves relative to its eddy in the direction of $\boldsymbol{k}$ can then be quantified as

$$\begin{aligned} s_{\mathrm{L}}(\boldsymbol{k}) &= \sqrt{\iiint \frac{k_i k_j}{|\boldsymbol{k}|^2}\left(1-\mathrm{H}_{|\boldsymbol{k}|}(|\boldsymbol{\kappa}|)-\mathrm{H}_{|\boldsymbol{\kappa}|}(|\boldsymbol{k}|)\right)^2 \widehat{R}_{ij}(\boldsymbol{\kappa},0)\,\mathrm{d}^3\boldsymbol{\kappa}} \\ &= \sqrt{\int_0^\infty \frac{k_i k_j}{|\boldsymbol{k}|^2}\left(1-\mathrm{H}_{|\boldsymbol{k}|}(|\boldsymbol{\kappa}|)-\mathrm{H}_{|\boldsymbol{\kappa}|}(|\boldsymbol{k}|)\right)^2 \mathring{\chi}_{ij}(\kappa)\,\mathrm{d}\kappa}. \end{aligned} \tag{42}$$

The factor $\left(1-\mathrm{H}_{|\boldsymbol{k}|}(|\boldsymbol{\kappa}|)-\mathrm{H}_{|\boldsymbol{\kappa}|}(|\boldsymbol{k}|)\right)^2$ is illustrated for $|\boldsymbol{k}|=1$ in Fig. 3.

Using similar arguments as the ones leading from (38) to (40) we arrive at modelling $\widehat{R}^{\mathrm{L}}_{ij}(\boldsymbol{k},\tau)$ as

$$\widehat{R}^{\mathrm{L}}_{ij}(\boldsymbol{k},\tau) = \int_{-\infty}^{t} \mathrm{e}^{-\frac{1}{2}\Theta^2_{\mathrm{L}}(\boldsymbol{k},\tau)}\, B_{im}(\boldsymbol{k}_0,t-t_0)N_{mn}(\boldsymbol{k}_0)B_{jn}(\boldsymbol{k}_0,t+\tau-t_0)\,\mathrm{d}t_0, \tag{43}$$

where $\boldsymbol{k}_0$ is given by (17), however, contrary to the Eulerian expression in (38), $\Theta_{\mathrm{L}}(\boldsymbol{k},\tau)$ is now given by

$$\Theta_{\mathrm{L}}(\boldsymbol{k},\tau) = \int_0^\tau s_{\mathrm{L}}(\boldsymbol{k}_{\tau'})|\boldsymbol{k}(\tau')|\mathrm{d}\tau', \tag{44}$$

where $\boldsymbol{k}(\tau') = (k_1, k_2, k_3 - \frac{\mathrm{d}U_1}{\mathrm{d}z}\tau'\, k_1)$ and $s_{\mathrm{L}}(\boldsymbol{k})$ is given by (42).

In terms of studying turbulence by tracking fluid particles and recording their instantaneous velocities, the right-hand side of (43) is the sum of the energy from newborn eddies, $N_{mn}(\boldsymbol{k}_0)$, that have been subjected to eddy

decay, $B_{ij}(\boldsymbol{k}_0, t-t_0)$ since their birth at $t_0$. When attempting to make the observation, however, the tracked particles used for the observation have left their original positions relative to their designated eddy, and, therefore, lost correlation according to $\exp\left(-\frac{1}{2}\Theta_{\mathrm{L}}^2(\boldsymbol{k},\tau)\right)$.

### 2.5 Remaining modelling choices

In order to evaluate (41) and (43) numerically we need expressions both for the added energy due to newborn eddies, $N_{ij}(\boldsymbol{k}_0)$, and for the eddy lifetime, $\tau_e(\boldsymbol{k})$.

With the first objective in mind, we follow Kolmogorov (1968) and assume that the isotropic energy spectrum, $E(|\boldsymbol{k}|)$, which is closely related to the isotropic spectral velocity tensor, is only a function of $|\boldsymbol{k}|$ and the rate of dissipation of turbulent energy, $\epsilon$, in the inertial subrange. Dimensional analysis then leads to

$$E(|\boldsymbol{k}|) \propto |\boldsymbol{k}|^{-\frac{5}{3}}\epsilon^{2/3}. \tag{45}$$

An isotropic energy spectrum with this property was suggested by von Kármán (1948) as

$$E\Big(\alpha_{\mathrm{K}}\epsilon^{2/3}, L_M, |\boldsymbol{k}|\Big) = \alpha_{\mathrm{K}}\epsilon^{2/3}\frac{|\boldsymbol{k}|^4}{\Big(L_M^{-1}+|\boldsymbol{k}|^2\Big)^{17/6}}, \tag{46}$$

where $\alpha_{\mathrm{K}}$ is the Kolmogorov constant. With (46) we can write the isotropic spectral velocity tensor as

$$\widehat{R}_{ij}^{\mathrm{ISO}}\Big(\alpha_{\mathrm{K}}\epsilon^{2/3}, L_M, \boldsymbol{k}\Big) = \frac{E\big(\alpha_{\mathrm{K}}\epsilon^{2/3}, L_M, |\boldsymbol{k}|\big)}{4\pi|\boldsymbol{k}|^2}\left(\frac{\delta_{ij}|\boldsymbol{k}|^2 - k_ik_j}{|\boldsymbol{k}|^2}\right). \tag{47}$$

Now, if we attempt to evaluate (41), for $\mathrm{d}U_1\big/\mathrm{d}z = 0$ and $\tau = 0$, using (23) we get

$$\begin{aligned}\widehat{R}_{ij}^{\mathrm{ISO}}(\boldsymbol{k}_0, 0) &= \int_{-\infty}^{t}\Big\langle \eta_i(\boldsymbol{k}_0, t_0, t-t_0)\overline{\eta_j(\boldsymbol{k}_0, t_0, t-t_0)}\,\mathrm{d}^3\boldsymbol{k}\,\mathrm{d}t_0\Big\rangle\,\mathrm{d}t_0 \\ &= \int_{-\infty}^{t}\mathrm{e}^{-\frac{t-t_0}{\tau_e(\boldsymbol{k})}}\Big\langle \eta_i(\boldsymbol{k}_0, t_0, 0)\overline{\eta_j(\boldsymbol{k}_0, t_0, 0)}\,\mathrm{d}^3\boldsymbol{k}\,\mathrm{d}t_0\Big\rangle\,\mathrm{d}t_0 \\ &= \tau_e(\boldsymbol{k}_0)N_{ij}(\boldsymbol{k}_0).\end{aligned} \tag{48}$$

Thus we have, for the isotropic case, quantified the added energy due to newborn eddies as

$$N_{ij}(\boldsymbol{k}_0) = \frac{\widehat{R}_{ij}^{\mathrm{ISO}}(\boldsymbol{k}_0)}{\tau_e(\boldsymbol{k}_0)}, \tag{49}$$

and we will assume that (49) is approximately true also for the non-isotropic case. Equation 49 thus follows Mann (1994) in that the eddies start out isotropic and become anisotropic through rapid distortion.

Regarding the eddy lifetime, we can argue that in the inertial subrange, $\tau_e(\boldsymbol{k})$ should only be a function of $|\boldsymbol{k}|$ and the rate of dissipation of turbulent energy, $\epsilon$, and use dimensional analysis to arrive at

$$\tau_e(\boldsymbol{k}) \propto |\boldsymbol{k}|^{-\frac{2}{3}} \epsilon^{-\frac{1}{3}}. \tag{50}$$

Although somewhat simplistic, we will, going forward, assume

$$\tau_e(\boldsymbol{k}) = \tau_e(|\boldsymbol{k}|) = \frac{M}{\sqrt{\alpha_{\mathrm{K}}}} |\boldsymbol{k}|^{-\frac{2}{3}} \epsilon^{-\frac{1}{3}}, \tag{51}$$

where the constant $M$ is introduced, also outside the inertial subrange. The Kolmogorov constant has been included in (51) because we find it convenient to keep the quantity $\alpha_{\mathrm{K}}\epsilon^{2/3}$ intact. We can now integrate (28) which, for $\mathrm{d}U_1/\mathrm{d}z > 0$, gives us

$$\begin{aligned}\Omega(\boldsymbol{k}_0, t-t_0) = \frac{\left(-k_{30} + \frac{\mathrm{d}U_1}{\mathrm{d}z} k_1 (t-t_0)\right)}{10M \frac{\mathrm{d}U_1}{\mathrm{d}z} k_1} \left| (k_1, k_2, k_{30} - \frac{\mathrm{d}U_1}{\mathrm{d}z} k_1 (t-t_0)) \right|^{2/3} \\ \left(3 + 2\,{}_2\mathrm{F}_1\left(5/6, 1, 3/2, -\frac{\left(k_{30} - \frac{\mathrm{d}U_1}{\mathrm{d}z} k_1 (t-t_0)\right)^2}{k_1^2 + k_2^2}\right)\right) \sqrt{\alpha_{\mathrm{K}}} \epsilon^{1/3},\end{aligned} \tag{52}$$

where ${}_2\mathrm{F}_1$ is the hypergeometric function. For $\mathrm{d}U_1/\mathrm{d}z \to 0$, we expect (52) to approach $\frac{t-t_0}{2\tau_e(\boldsymbol{k}_0)}$ plus an integration constant.

One way of determining the constant $M$ would be to use that in the inertial subrange

$$\begin{aligned}\chi_{13}(k_1, 0) \to \iint\limits_{\kappa_1 = k_1} \tau_e(\boldsymbol{\kappa})^2 \left( -\frac{1}{\tau_e(\boldsymbol{\kappa})} \frac{\mathrm{d}\, \widehat{R}_{13}^{\mathrm{ISO}}(\boldsymbol{\kappa}_0(0))}{\mathrm{d}t_0} \right. \\ \left. + \frac{\mathrm{D}\left\langle \eta_1(\boldsymbol{\kappa}_0, 0, 0)\, \overline{\eta_3(\boldsymbol{\kappa}_0, 0, 0)}\, \mathrm{d}^3\boldsymbol{\kappa}\, \mathrm{d}t_0 \right\rangle}{\mathrm{D}\, t} \right) \mathrm{d}^3\boldsymbol{\kappa} \\ \to \iint\limits_{\kappa_1 = k_1} \frac{\mathrm{d}U_1}{\mathrm{d}z} \frac{5k_1^2 k_3^2 - 3k_2^2|\boldsymbol{k}|^2}{12\pi|\boldsymbol{k}|^6} \tau_e(\boldsymbol{\kappa}) E(|\boldsymbol{\kappa}|)\, \mathrm{d}^3\boldsymbol{\kappa} = -\frac{33}{1729} \frac{\mathrm{d}U_1}{\mathrm{d}z} \tau_e(k_1) E(k_1),\end{aligned} \tag{53}$$

in which $\boldsymbol{\kappa}_0(t-t_0) = (\kappa_1, \kappa_2, \kappa_3 + \kappa_1 \frac{\mathrm{d}U_1}{\mathrm{d}z}(t-t_0))$. Inserting the asymptotic behavior of $\tau_e(k_1)$ and $E(k_1)$ we see that the right-hand side of (53) scales as $k_1^{-\frac{7}{3}} \epsilon^{1/3}$, which is consistent with observations (Wyngaard and Coté, 1972). To remove its dependence on $\epsilon$ we can divide the square of $\chi_{13}(k_1, 0)$ with $\chi_{11}(k_1, 0)$, which correspondingly approaches $\frac{9}{55} k_1^{-\frac{5}{3}} \alpha_{\mathrm{K}} \epsilon^{2/3}$. In Section 4 we will follow this line of reasoning and study

$$M^*(k_1) = \sqrt{\frac{k_1^3\, \chi_{13}(k_1, 0)^2}{\chi_{11}(k_1, 0)}} \frac{1729}{33} \sqrt{\frac{9}{55}} \left(\frac{\mathrm{d}U_1}{\mathrm{d}z}\right)^{-1}, \tag{54}$$

where $M^*(k_1)$ consequently should approach $M$ in the inertial subrange. Equation 54 thus indicates that studying the ratio between different components of the cross-spectra at known shear could be interesting in terms of determining $M$.

This section introduced an expression for the added energy due to newborn eddies, $N_{ij}(\boldsymbol{k}_0)$, as well as an expression for the eddy lifetime, $\tau_e(\boldsymbol{k})$. It can be argued that these expressions are on the simplistic side and that they should depend on, for example, $R_{ij}$. The counter argument would be that coupling the building blocks of the model to the end result in such a way would make the model significantly harder to evaluate. The section ended with implicitly suggesting an experiment for determining $M$ (introduced in (51)), which is a key quantity of the framework.

## 3 Practical application of the models

### 3.1 Implementing the spectral velocity tensor for $\tau = 0$

When implementing the spectral velocity tensor(s) it is convenient to introduce

$$G = \frac{M}{\sqrt{\alpha_{\mathrm{K}}}\epsilon^{1/3}} \frac{\mathrm{d}U_1}{\mathrm{d}z} L_M^{2/3}, \tag{55}$$

which, for $\mathrm{d}U_1/\mathrm{d}z > 0$, enables us to write (51) as

$$\tau_e(\boldsymbol{k}) = G \left(\frac{\mathrm{d}U_1}{\mathrm{d}z}\right)^{-1} L_M^{-\frac{2}{3}} |\boldsymbol{k}|^{-\frac{2}{3}} \tag{56}$$

and (52) can then, for $G > 0$, be written as

$$\begin{aligned}\Omega(L_M, G, \boldsymbol{k}_0, \beta) = \frac{(-k_{30} + k_1\beta)}{10Gk_1} |(k_1, k_2, k_{30} - k_1\beta)|^{2/3} \\ L_M^{2/3} \left(3 + 2\,{}_2\mathrm{F}_1\left(5/6, 1, 3/2, -\frac{(k_{30} - k_1\beta)^2}{k_1^2 + k_2^2}\right)\right)\end{aligned} \tag{57}$$

with $\beta = \frac{\mathrm{d}U_1}{\mathrm{d}z}(t - t_0)$. This in turn allows us to write (25) as

$$\begin{aligned}&\boldsymbol{B}(L_M, G, \boldsymbol{k}_0, \beta) \\ &= \mathrm{e}^{-(\Omega(L_M, G, \boldsymbol{k}_0, \beta) - \Omega(L_M, G, \boldsymbol{k}_0, 0))} \begin{bmatrix} 1 & 0 & \zeta_1(\boldsymbol{k_0}, \beta) \\ 0 & 1 & \zeta_2(\boldsymbol{k_0}, \beta) \\ 0 & 0 & |\boldsymbol{k}|^2/|(k_1, k_2, k_{30} - k_1\beta)|^2 \end{bmatrix}\end{aligned} \tag{58}$$

with $\zeta_1$ and $\zeta_1$ still given by (26) and (27). We can now reformulate (41) for $\tau = 0$ and $\mathrm{d}U_1/\mathrm{d}z > 0$ according to

$$\begin{aligned}\widehat{R}_{ij}(\boldsymbol{k},0) &= \int_{-\infty}^{t} B_{im}(\boldsymbol{k}_0, t-t_0)\frac{1}{\tau_e(\boldsymbol{k}_0)}\widehat{R}^{\mathrm{ISO}}_{mn}(\boldsymbol{k}_0)B_{jn}(\boldsymbol{k}_0, t-t_0)\,\mathrm{d}t_0 \\ &= \int_0^{\infty} B_{im}(L_M, G, \boldsymbol{k}_0, \beta)\frac{L_M^{2/3}|\boldsymbol{k}_0|^{2/3}}{G}\widehat{R}^{\mathrm{ISO}}_{mn}\Big(\alpha_{\mathrm{K}}\epsilon^{2/3}, L_M, \boldsymbol{k}\Big)B_{jn}(L_M, G, \boldsymbol{k}_0, \beta)\,\mathrm{d}\beta \\ &= \widehat{R}_{ij}\Big(\alpha_{\mathrm{K}}\epsilon^{2/3}, L_M, G, \boldsymbol{k}_0\Big), \end{aligned} \tag{59}$$

where $\boldsymbol{k}_0 = (k_1, k_2, k_3 + k_1\frac{\mathrm{d}U_1}{\mathrm{d}z}(t-t_0)) = (k_1, k_2, k_3 + k_1\beta)$. In the last step of (59) we have introduced $\widehat{R}_{ij}\big(\alpha_{\mathrm{K}}\epsilon^{2/3}, L_M, G, \boldsymbol{k}\big)$ for $G > 0$. For $G = 0$ (which corresponds to $\mathrm{d}U_1/\mathrm{d}z = 0$) we set

$$\widehat{R}_{ij}\Big(\alpha_{\mathrm{K}}\epsilon^{2/3}, L_M, 0, \boldsymbol{k}\Big) = \widehat{R}^{\mathrm{ISO}}_{ij}\Big(\alpha_{\mathrm{K}}\epsilon^{2/3}, L_M, \boldsymbol{k}\Big), \tag{60}$$

with $\widehat{R}^{\mathrm{ISO}}_{ij}$ given by (47). As $R^{\mathrm{L}}_{ij}(\boldsymbol{x}, 0) = R_{ij}(\boldsymbol{x}, 0)$ it should come as no surprise that also $\widehat{R}^{\mathrm{L}}_{ij}$ can be simplified to $\widehat{R}_{ij}\big(\alpha_{\mathrm{K}}\epsilon^{2/3}, L_M, G, \boldsymbol{k}\big)$ for $\tau = 0$.

The spectral velocity tensor defined in (59) is closely related to the Mann (1994) tensor, which can similarly be written $\widehat{R}_{ij}\big(\alpha_{\mathrm{K}}\epsilon^{2/3}, L_M, \Gamma, \boldsymbol{k}\big)$. The difference between the two tensors lies in how $\tau_e(\boldsymbol{k})$, which in Mann (1994) is given by

$$\Gamma\,\frac{\mathrm{d}U_1}{\mathrm{d}z}^{-1}\frac{|\boldsymbol{k}|^{-\frac{2}{3}}L_M^{-\frac{2}{3}}}{\sqrt{{}_2\mathrm{F}_1\Big(\frac{1}{3}, \frac{17}{6}, \frac{4}{3}, -|\boldsymbol{k}|^{-2}L_M^{-2}\Big)}} \tag{61}$$

instead of (56), is combined with the rapid distortion equation. As previously mentioned, instead of decaying continuously, the eddies in Mann (1994) are subjected to rapid distortion according to their current age, which is set to exactly $\tau_e(\boldsymbol{k})$. This way of assigning a typical age to the eddies enables the Mann (1994) tensor to avoid the integration over eddy birth times seen e.g. in (41). As has been shown before and will be demonstrated again in Sect. 4.1, the Mann (1994) tensor performs very well for the case $\tau = 0$, despite its simplified approach to eddy decay.

Next, we consider the case $\tau \neq 0$, a situation in which the Mann (1994) tensor is not applicable.

### 3.2 Implementing the spectral velocity tensor for $\tau \neq 0$

Using (29) and (59) we can simplify (41) to

$$\begin{aligned}\widehat{R}_{ij}\Big(\alpha_{\mathrm{K}}\epsilon^{2/3}, L_M, G, \boldsymbol{k}, \tau\Big) = \mathrm{e}^{-\frac{1}{2}\Theta^2(\boldsymbol{k},\tau)}\widehat{R}_{im}\Big(\alpha_{\mathrm{K}}\epsilon^{2/3}, L_M, G, \boldsymbol{k}\Big) \\ B_{jm}\left(L_M, G, \boldsymbol{k}, \frac{G\sqrt{\alpha_{\mathrm{K}}}\epsilon^{1/3}}{ML_M^{2/3}}\tau\right),\end{aligned} \tag{62}$$

where $B_{ij}$ is given by (58), and where $\Theta(\boldsymbol{k},\tau)$ is defined in (38). Though not clear from the notation, $\Theta(\boldsymbol{k},\tau)$ depends also on $\alpha_{\mathrm{K}}\epsilon^{2/3}$, $L_M$ and $G$.

Equation 43 can analogously be simplified to

$$\widehat{R}^{\mathrm{L}}_{ij}\Big(\alpha_{\mathrm{K}}\epsilon^{2/3}, L_M, G, \boldsymbol{k}, \tau\Big) = \mathrm{e}^{-\frac{1}{2}\Theta^2_{\mathrm{L}}(\boldsymbol{k},\tau)}\,\widehat{R}_{im}\Big(\alpha_{\mathrm{K}}\epsilon^{2/3}, L_M, G, \boldsymbol{k}\Big) \qquad (63)$$
$$B_{jm}\left(L_M, G, \boldsymbol{k}, \frac{G\sqrt{\alpha_{\mathrm{K}}}\epsilon^{1/3}}{ML_M^{2/3}}\tau\right),$$

with $\Theta_{\mathrm{L}}$ defined in (44).

Evaluating (62) or (63) for $\tau \neq 0$ can, however, be very computationally intensive. The reason is that, in the process, we evaluate (38) or (44), and then integrate (34) and (42), respectively, both of which in turn integrate (59). One solution to this problem is to first evaluate $\mathring{\chi}_{ij}\big(\alpha_{\mathrm{K}}\epsilon^{2/3}, L_M, G, |\boldsymbol{k}|\big)$, defined in (5), for a range of $|\boldsymbol{k}|$-values and use interpolation in the resulting look-up table when evaluating (34), or (42). The look-up table can be calculated once and for all if the relationship

$$\widehat{R}_{ij}(1,1,G,L_M\boldsymbol{k}) = \frac{\widehat{R}_{ij}\big(\alpha_{\mathrm{K}}\epsilon^{2/3}, L_M, G, \boldsymbol{k}\big)}{\alpha_{\mathrm{K}}\epsilon^{2/3}L_M^{11/3}}, \qquad (64)$$

which leads to

$$\mathring{\chi}_{ij}\Big(\alpha_{\mathrm{K}}\epsilon^{2/3}, L_M, G, |\boldsymbol{k}|\Big) = \alpha_{\mathrm{K}}\epsilon^{2/3}\,L_M^{5/3}\,\mathring{\chi}_{ij}(1,1,G,L_M|\boldsymbol{k}|), \qquad (65)$$

is used and the look-up table is constructed in two dimensions, $G$ and $L_M|\boldsymbol{k}|$.

Next, we discuss two different strategies for obtaining the necessary input information required to evaluate the presented models, an objective that, assuming knowledge of the constants $\alpha_K$ and $M$, is equivalent to finding suitable values of the parameters $\alpha_{\mathrm{K}}\epsilon^{2/3}$ , $L_M$ and $G$.

### 3.3 Deriving parameter values from $\epsilon$, $u_*$ and $\mathrm{d}U_1/\mathrm{d}z$

Assuming knowledge of the rate of dissipation of turbulent kinetic energy, $\epsilon$, the friction velocity, $u_*$, and the shear, $\mathrm{d}U_1/\mathrm{d}z$, then clearly $\alpha_{\mathrm{K}}\epsilon^{2/3}$ is given directly by the rate of dissipation, $\epsilon$, and the Kolmogorov constant, $\alpha_{\mathrm{K}}$. With the objective of deriving $L_M$ and $G$ from $\epsilon$, $u_*$ and $\mathrm{d}U_1/\mathrm{d}z$, we start by rearranging (55) to

$$M = \frac{G\sqrt{\alpha_{\mathrm{K}}}\epsilon^{1/3}}{\frac{\mathrm{d}U_1}{\mathrm{d}z}L_M^{2/3}} \qquad (66)$$

and multiplying both sides by $\frac{u_*^2\frac{\mathrm{d}U_1}{\mathrm{d}z}}{\alpha_{\mathrm{K}}^{3/2}\epsilon}$ to obtain

$$M\frac{u_*^2\frac{\mathrm{d}U_1}{\mathrm{d}z}}{\alpha_{\mathrm{K}}^{3/2}\epsilon} = \frac{G\sqrt{\alpha_{\mathrm{K}}}\epsilon^{1/3}}{\frac{\mathrm{d}U_1}{\mathrm{d}z}L_M^{2/3}}\frac{u_*^2\frac{\mathrm{d}U_1}{\mathrm{d}z}}{\alpha_{\mathrm{K}}^{3/2}\epsilon} = \frac{Gu_*^2}{\alpha_{\mathrm{K}}\epsilon^{2/3}L_M^{2/3}} = -G\iiint \widehat{R}_{13}(1,1,G,\boldsymbol{\xi})\,\mathrm{d}^3\boldsymbol{\xi}, \qquad (67)$$

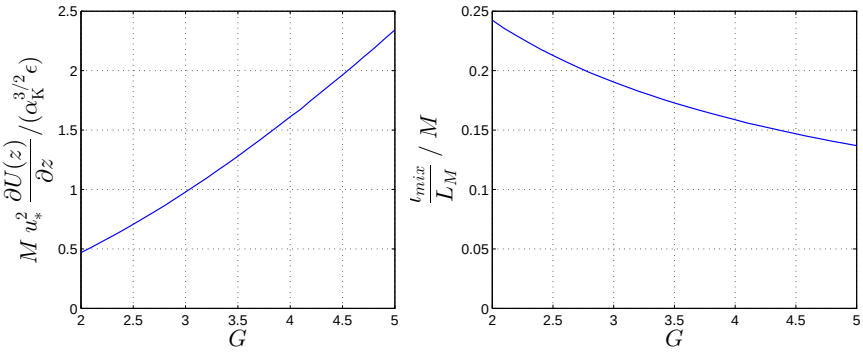


**Fig. 4** To the left, the left-hand side of (67) versus G shows that G is uniquely determined by the ratio between the turbulent energy production from the shear gradient and the rate of dissipation or turbulent kinetic energy. To the right, the left-hand side of (69) divided by M shows that the ratio ${}^{l_{mix}}\!/_{L_M}$ depends on $G$ and thereby, also this quantity depends on the ratio between the turbulent energy produced from the shear gradient and the rate of dissipation.

where, in the last step, we have used (64). We note that the right-hand side of (67) is a function of $G$ only. In Fig. 4, this quantity is displayed for a typical range of $G$. The left-hand side of (67) can be interpreted as the ratio between the shear production of turbulent kinetic energy, $u_*^2 \frac{\mathrm{d}U_1}{\mathrm{d}z}$, and the rate of dissipation of turbulent kinetic energy, $\epsilon$, multiplied by a constant. As seen in Fig. 4, this ratio determines $G$ uniquely.

Having determined $G$, then $L_M$ is given by (55) as

$$L_M = \frac{G^{3/2} \alpha_K^{3/4} \epsilon^{1/2}}{\frac{\mathrm{d}U_1}{\mathrm{d}z}^{3/2} M^{3/2}}. \tag{68}$$

Digressing slightly, we divide the definition of the mixing length, $l_{mix} = u_* / \frac{\mathrm{d}U_1}{\mathrm{d}z}$, with (68) and obtain

$$\frac{l_{mix}}{L_M} = \frac{u_* / \frac{\mathrm{d}U_1}{\mathrm{d}z}}{\left( \frac{G^{3/2} \alpha_K^{3/4} \epsilon^{1/2}}{\frac{\mathrm{d}U_1}{\mathrm{d}z}^{3/2} M^{3/2}} \right)} = \frac{M}{G} \sqrt{\frac{u_*^2 \frac{\mathrm{d}U_1}{\mathrm{d}z} M}{G \alpha_K^{3/2} \epsilon}} = \frac{M}{G} \sqrt{- \iiint \widehat{R}_{13}(1, 1, G, \boldsymbol{\xi})\, \mathrm{d}^3 \boldsymbol{\xi}}, \tag{69}$$

where in the last step we have used (67). In the right-hand graph of Fig. 4 we see how $\frac{l_{mix}}{L_M} / M$ depends on $G$.

In this section we have shown that knowledge of $\epsilon$, $u_*$ and ${}^{\mathrm{d}U_1}\!/_{\mathrm{d}z}$ is sufficient to derive the necessary input information for the spectral velocity tensor. In the process we have also shown that both $G$ and the ratio $\frac{l_{mix}}{L_M}$ are given uniquely by the ratio between the shear production of turbulent kinetic energy, $u_*^2 \frac{\mathrm{d}U_1}{\mathrm{d}z}$, and the rate of dissipation of turbulent kinetic energy, $\epsilon$.

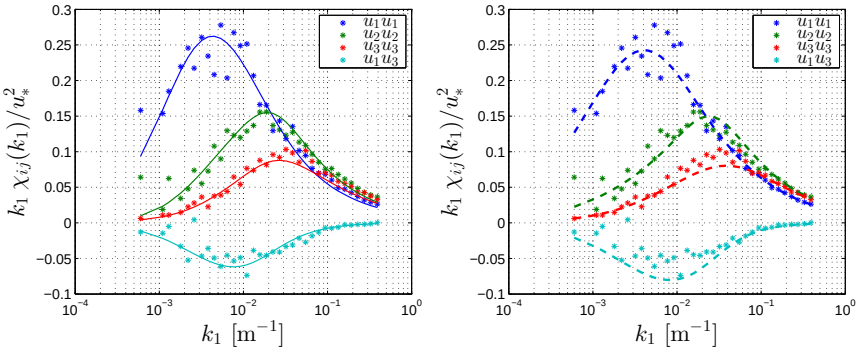


**Fig. 5** Comparison of spatial spectra from the spectral velocity tensor (left) and the Mann (1994) tensor (right) for neutral stratification at 16 m s$^{-1}$. The spectral velocity tensor fits the components of the measured spectra at least as well as the Mann (1994) tensor, and it does not, at least in this example, over-predict the $u_1u_3$ cross-spectrum as Mann (1994) has been reported to do. The resulting parameters of the spectral velocity tensor vs. the Mann (1994) tensor are $\alpha_{\mathrm{K}}\epsilon^{2/3} = 0.070$ m$^{4/3}$s$^{-2}$ vs. $\alpha_{\mathrm{K}}\epsilon^{2/3} = 0.085$ m$^{4/3}$s$^{-2}$, $L_M = 63.3$ m vs. $L_M = 51.2$ m and $G = 3.46$ vs. $\Gamma = 3.49$. The experience so far is that the difference in the resulting parameters is smaller than the uncertainty incurred by the choices made when designing the fitting procedure.

### 3.4 Determining parameter values from measured spectra

For many applications the physical properties $\epsilon$, $u_*$ and $\mathrm{d}U_1/\mathrm{d}z$ are not known, and it can be advantageous to use the alternative strategy outlined in Mann (1994), of measuring spectra and determining which set of tensor parameter values best reproduces the measured spectra.

Finding tensor parameters in this way requires repeated evaluation of (4), and with this in mind it may be beneficial to first produce a look-up table of $\chi_{ij}(1, 1, G, L_M k_1)$ and interpolate to find

$$\chi_{ij}\left(\alpha_{\mathrm{K}}\epsilon^{2/3}, L_M, G, k_1\right) = \alpha_{\mathrm{K}}\epsilon^{2/3}\, L_M^{5/3}\, \chi_{ij}(1, 1, G, L_M k_1). \tag{70}$$

In Fig. 5 this method is applied to spectra measured at 80 m height and 16 m s$^{-1}$ at Høvsøre, Denmark, for neutral atmospheric stability. The resulting values of $\alpha_{\mathrm{K}}\epsilon^{2/3}$, $L_M$ and $G$ are not identical to the closely related parameters of the Mann (1994) tensor $\alpha_{\mathrm{K}}\epsilon^{2/3}$, $L_M$ and $\Gamma$. However, the differences between the resulting parameter values of the two tensors are dwarfed by the uncertainty owing to the choices made in the fitting procedure, i.e. a small change in the fitting procedure would change the comparison result. The spectral velocity tensor fits the components of the measured spectra at least as well as the Mann (1994) tensor. We note that the spectral velocity tensor does not, at least in this example, over-predict the $u_1u_3$ cross-spectrum as apparently the case using the Mann (1994) tensor, see Peña et al. (2010).

We have not taken into consideration the fact that the measured spectra in this case were not truly spatial spectra, but obtained using a stationary

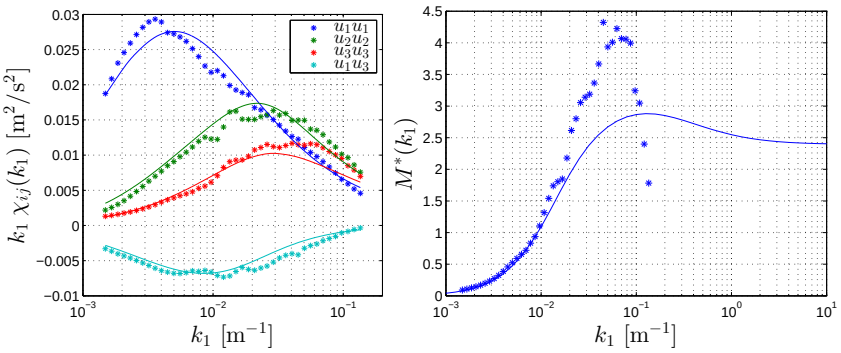


**Fig. 6** To the left, fitting the spectral velocity tensor to spatial LES spectra, resulting in parameter values: $\alpha_{\mathrm{K}}\epsilon^{2/3} = 0.0085\ \mathrm{m}^{4/3}\mathrm{s}^{-2}$, $L_M = 57.7$ m and $G = 3.23$. To the right, an attempt to determine $M$ using (54), where, as we recall, the quantity, $M^*$, is expected to approach $M$ asymptotically in the inertial subrange. The solid line shows the quantity in question using the spectral velocity tensor with the set of parameter values resulting from the afore-mentioned spectral fitting. As expected, the curve approaches the value given by (66) for high values of $k_1$. The corresponding LES results indicates a higher trajectory than the solid line, before trailing off, presumably due to the finite resolution of the calculation grid.

anemometer. The spectra corresponding to a stationary anemometer can be derived from $\widehat{R}(\boldsymbol{k},\tau)$ by first calculating $R(\boldsymbol{x} - (\boldsymbol{U_0} + \boldsymbol{U}(\boldsymbol{x}))\,\tau, \tau)$. This avenue is, however, not pursued here because it appears quite computationally intensive. When attempting this, one may keep in mind that $x_1$ of the spectral velocity tensor is not defined as aligned with the mean wind, $\boldsymbol{U_0} + \boldsymbol{U}(\boldsymbol{x})$, but with the direction of the shear, $\mathrm{d}\boldsymbol{U}/\mathrm{d}z$.

## 4 Validation

### 4.1 Lateral and longitudinal coherence

To investigate the spectral velocity tensor's ability to predict coherences, we turn to data from LES performed on a $600 \times 600 \times 400$ cell mesh with a resolution of $4 \times 4 \times 2.5$ m. We choose data from a height of 100 m of a neutrally stratified simulation, and here we define $x_1$ as being parallel to $\mathrm{d}\boldsymbol{U}/\mathrm{d}z$. For more information regarding the LES see Sullivan and Patton (2011) and Berg et al. (2013).

Given that we have access to whole planes of data we can calculate spatial spectra, and in Fig. 6 we have determined the parameter values of the spectral velocity tensor that best reproduces the LES spatial spectra. The resulting values, $\alpha_{\mathrm{K}}\epsilon^{2/3} = 0.0085\ \mathrm{m}^{4/3}\mathrm{s}^{-2}$, $L_M = 57.7$ m and $G = 3.23$, together with $\mathrm{d}U_1/\mathrm{d}z = 0.0083s^{-1}$ correspond to $M = 2.40$. Determining $M$ from the parameters resulting from the fitting of measured spectra was tried in de Maré and Mann (2014) in which the value $M = 3$ was proposed, however,

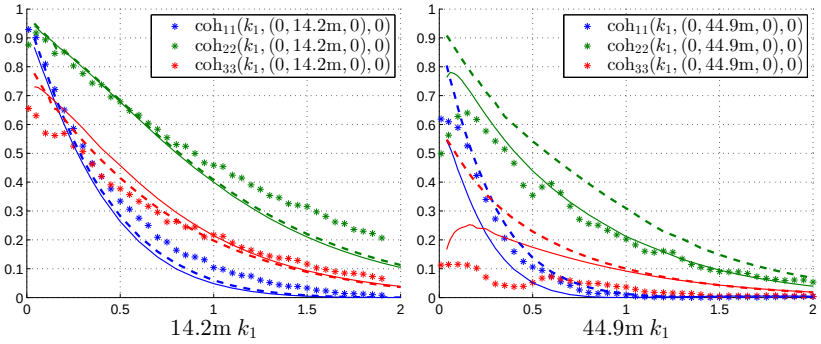


**Fig. 7** To the left, lateral coherence, $\mathrm{coh}_{ij}(k_1, \boldsymbol{r}, 0)$ for $\boldsymbol{r} = (0, 14.2\mathrm{m}, 0)$. Both the spectral velocity tensor (solid lines) and the Mann (1994) tensor (dashed) perform well for this distance. To the right, the same quantity for $\boldsymbol{r} = (0, 44.9\mathrm{m}, 0)$. The Mann (1994) tensor performs better for the streamwise component (blue), whereas the situation is reversed for the transversal component (green). Both tensors over-predict the vertical component (red).

the uncertainty using this methodology is considerable. Perhaps a better way of determining $M$ is to use (54), and this method is demonstrated in the right-hand graph of Fig. 6 where the LES results indicate a higher value than the afore-mentioned $M$-value of 2.40. Using LES to determine $M$ in this way is, however, not ideal owing to the finite resolution of the calculation grid. Therefore, we recommend using $M = 3$ for now, however, based on the above considerations, the uncertainty in this value is currently 20% or more.

It is worth mentioning that, with the look-up table of $\chi_{ij}(1, 1, G, L_M k_1)$, mentioned in Sect. 3.4, it is straightforward to verify the formal manipulations of (53) (which is the basis for (54)). If the derivation is correct then the quantity

$$G^{-1} k_1^{7/3} L_M^{7/3} \, \chi_{13}(1, 1, G, L_M k_1) \tag{71}$$

should, according to (53) combined with (51), (66) and (70), approach $-\frac{33}{1729}$ in the inertial sub-range.

In Fig. 7, to the left, we compare lateral coherence, $\mathrm{coh}_{ij}(k_1, \boldsymbol{r}, 0)$, for $\boldsymbol{r} = (0, 14.2\,\mathrm{m}, 0)$ derived from the spectral velocity tensor with the same quantity extracted from the LES data. The right-hand graph of Fig. 7 shows the same quantities for $\boldsymbol{r} = (0, 44.9\,\mathrm{m}, 0)$. In the graphs of Fig. 7, lateral coherence derived from the Mann (1994) tensor is shown for comparison, and it is found that the new spectral velocity tensor performs on par with the Mann (1994) tensor. Both tensors over-predict coherence for the vertical component at separations larger than $0.5 L_M$ in the lateral direction.

Coherence in the vertical direction is not addressed at this point, as the lack of homogeneity makes this direction less straightforward. When addressing such coherences, the methodology of Mann (1994) can be used as inspiration.

In Fig. 8, to the left, we compare the longitudinal coherence, $\mathrm{coh}_{ij}(k_1, \mathbf{0}, \tau)$, derived from the spectral velocity tensor with the same quantity extracted from the LES data, for $k_1 = 0.33/l_{\mathrm{mix}} = 0.71/L_M$. The Mann (1994) tensor

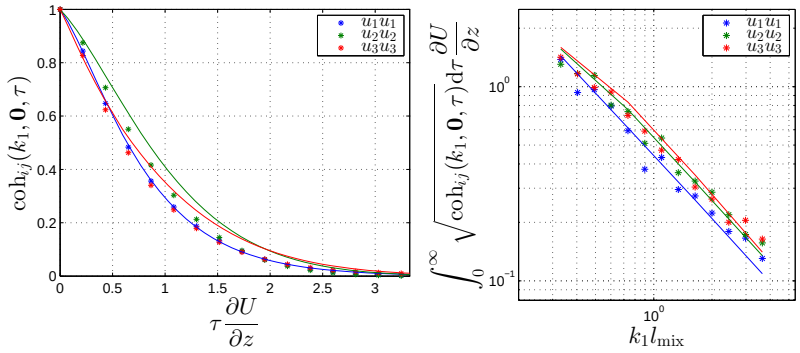


**Fig. 8** To the left, longitudinal coherence derived from the spectral velocity tensor (solid lines) for $k_1 = 0.33/l_{\mathrm{mix}} = 0.71/L_M$ is compared to the same quantity extracted from the LES data. To the right, an integral time scale constructed from the longitudinal coherence. The value of $k_1$ in the left-hand graph corresponds to the left-most dot(s) in the right-hand graph.

is not included in the graphs because, combined with Taylor's assumption of frozen turbulence, it would predict $\mathrm{coh}_{ij}(k_1, \mathbf{0}, \tau) = 1$ for all time lags. The right-hand graph of Fig. 8 shows an integral time scale constructed as $\int_0^\infty \sqrt{\mathrm{coh}_{ij}(k_1, \mathbf{0}, \tau)}\, \mathrm{d}\tau$.

### 4.2 Eulerian and Lagrangian two-point correlations in isotropic turbulence

We also compare how the spectral velocity tensor and its Lagrangian counterpart perform compared to measured results for isotropic turbulence presented in Ott and Mann (2005). In Fig. 9, we see the Eulerian covariance, $R_{ii}(\boldsymbol{r}, \tau)$, for different separations $\boldsymbol{r}$ and $\tau$, as well as the Lagrangian covariance, $R^{\mathrm{L}}_{ii}(\mathbf{0}, \tau)$, and the Eulerian covariance, $R_{ii}(\mathbf{0}, \tau)$. Both quantities are predicted significantly better than by any of the models presented in Ott and Mann (2005).

The cross-over point of the Eulerian and Lagrangian covariances, seen in the right-hand graph of Fig. 9, is sensitive to the choice of expression for $R_k$, see (33). As seen in the graph, the chosen expression predicts a cross-over at approximately half the maximum value, a behavior reported in e.g Fung et al. (1992) and Ott and Mann (2005). For comparison, no cross-over point is predicted, if one the alternative expressions mentioned in section 2.3, is used instead. In the evaluation of the models we have used $\mathrm{d}U_1/\mathrm{d}z = 0$, $\alpha_{\mathrm{K}}\epsilon^{2/3} = 0.00622\ \mathrm{m}^{4/3}\mathrm{s}^{-2}$, $L_M = 0.0273$ m and $M = 3$.

## 5 Conclusions

A spectral velocity tensor has been developed to predict all two-point correlations in space and time in sheared homogeneous turbulence. This was accomplished by combining the design philosophies behind two existing models,

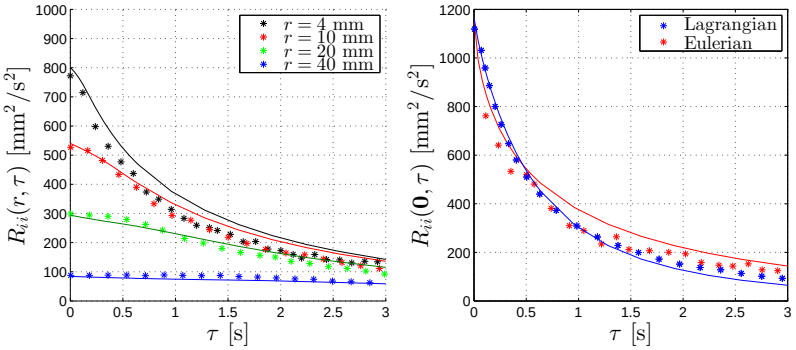


**Fig. 9** Sum of covariances for all three components derived from the spectral velocity tensor (solid lines) compared to measured results for isotropic turbulence presented in Ott and Mann (2005). To the left, Eulerian covariance for various separations in space and time. To the right, a comparison between the Eulerian and the Lagrangian covariance for $\boldsymbol{r} = 0$. We see that our model reproduces the crossover of $R^{\mathrm{L}}_{ii}(\mathbf{0},\tau)$ and $R_{ii}(\mathbf{0},\tau)$ at approximately half the maximum value, a behaviour also reported in Fung et al. (1992).

the Mann spectral velocity tensor, in which isotropic turbulence is distorted according to rapid distortion theory, and Kristensen's longitudinal coherence model, in which eddies are simultaneously advected by larger eddies as well as decaying.

The model is built on simplified physics and assumptions such as that *eddies created at different times are uncorrelated*, and that *larger eddies displace smaller eddies as if the smaller eddies were shaped like spheres*. Assumptions such as these can be challenging to validate directly, and are here instead seen as indirectly validated by the prediction capabilities of the resulting model.

The model needs values of three parameters, $\alpha_{\mathrm{K}}\epsilon^{2/3}$, $L_M$ and $G$, as input. It was shown that these values can be derived from the following physical properties of the flow: the rate of dissipation of turbulent kinetic energy, $\epsilon$, the friction velocity, $u_*$, and the shear, $\mathrm{d}U_1/\mathrm{d}z$. Alternatively, the values of the input parameters can, as with the closely related parameters of the Mann (1994) tensor, be derived from measured spectra.

The resulting model predicts spatial correlations comparably to the Mann (1994) tensor and temporal coherence better than any of the models evaluated in Ott and Mann (2005). As part of the framework, a spectral velocity tensor for Lagrangian correlations in space and time is also developed and validated versus measurements of isotropic turbulence. Combined, the models reproduce the cross-over point between Eulerian and Lagrangian temporal covariances. As per the scope of the validation, the developed models can be used, for example, in wind turbine engineering applications such as lidar-assisted feed forward control and wind turbine wake modelling.

Future work might include experiments to better determine the introduced quantity $M$. An experiment with this objective, studying the ratio between different components of the cross-spectra at known shear, is implicitly proposed

in Sect. 2.5. Other developments could include investigating the implications of using a rapid distortion formulation that also includes, e.g., buoyancy effects.

## 6 Acknowledgments

This work has been made possible by funding from Forsknings- og Innovationsstyrelsen, DONG Energy A/S and the DSF Flow Center. The authors would like to thank Ned Patton at UCAR for generously making LES data available, and Gunner Larsen and Søren Ott for valuable suggestions and feedback.

## References

Batchelor GK (1953) The theory of homogeneous turbulence. Cambridge University Press, United Kingdom, pp 28–33

Berg J, Mann J, Patton EG (2013) Lidar-Observed Stress Vectors and Veer in the Atmospheric Boundary Layer. J Atmos OceanTechnol 30(9):1961–1969, DOI 10.1175/JTECH-D-12-00266.1

Bossanyi E (2013) Un-freezing the turbulence: application to LiDAR-assisted wind turbine control. IET Renewable Power Generation 7(4):321–329

Bossanyi E, Savini B, Iribas M, Hau M, Fischer B, Schlipf D, van Engelen T, Rossetti M, Carcangiu CE (2012) Advanced controller research for multi-MW wind turbines in the UPWIND project. Wind Energy 15(1):119–145, DOI 10.1002/we.523

Chougule A, Mann J, Segalini A, Dellwik E (2014) Spectral tensor parameters for wind turbine load modeling from forested and agricultural landscapes. Wind Energy 18(3):469–481, DOI 10.1002/we.1709

Chougule AS (2013) Influence of atmospheric stability on the spatial structure of turbulence. DTU Wind Energy PhD-0028 (EN)

Fung JCH, Hunt JCR, Malik NA, Perkins RJ (1992) Kinematic simulation of homogeneous turbulence by unsteady random Fourier modes. J Fluid Mech 236:281–318, DOI 10.1017/S0022112092001423

Hanazaki H, Hunt JCR (2004) Structure of unsteady stably stratified turbulence with mean shear. J Fluid Mech 507:1–42, DOI 10.1017/S0022112004007888

Hunt JCR, Wray AA, Buell JC (1987) Big whorls carry little whorls. Res Proc of 1987 Summer Program,CTR-S87 NASA Centre for Turb Res

Kaneda Y, Ishida T (2000) Suppression of vertical diffusion in strongly stratified turbulence. J Fluid Mech 402:311–327

von Kármán T (1948) Progress in the statistical theory of turbulence. Proceedings of the National Academy of Sciences, 34(11):530–539

Kolmogorov AN (1968) Local structure of turbulence in an incompressible viscous fluid at very high Reynolds numbers. Soviet Physics Uspekhi 10(6):734

Kristensen L (1979) On longitudinal spectral coherence. Boundary-Layer Meteorol 16(2):145–153, DOI 10.1007/BF02350508

Larsen GC, Madsen HA, Thomsen K, Larsen TJ (2008) Wake meandering: a pragmatic approach. Wind Energy 11(4):377–395, DOI 10.1002/we.267

Mann J (1994) The spatial structure of neutral atmospheric surface-layer turbulence. J Fluid Mech 273:141–168, DOI 10.1017/S0022112094001886

de Maré M, Mann J (2014) Validation of the Mann spectral tensor for offshore wind conditions at different atmospheric stabilities. Journal of Physics: Conference Series 524(1):12,106

Mikkelsen T, Angelou N, Hansen K, Sjöholm M, Harris M, Slinger C, Hadley P, Scullion R, Ellis G, Vives G (2013) A spinner-integrated wind lidar for enhanced wind turbine control. Wind Energy 16(4):625–643, DOI 10.1002/we.1564

Moffatt K (1967) Interaction of turbulence with strong wind shear. Atmosphere Turbulence and Radio Wave Propagation (Ed. A.M. Yaglom & V.I. Tatarski, (Nauka, Moscow)):139–156

Ott S, Mann J (2005) An experimental test of Corrsin's conjecture and some related ideas. New Journal of Physics 7(1):142

Pao LY, Johnson KE (2011) Control of wind turbines. Control Systems, IEEE 31(2):44–62

Peña A, Gryning SE, Mann J (2010) On the length-scale of the wind profile. Q J R Meteorol Soc 136(653):2119–2131, DOI 10.1002/qj.714

Pope SB (2000) Turbulent Flows. Cambridge University Press, United Kingdom, pp 219–223

Saffman PG (1963) An approximate calculation of the Lagrangian autocorrelation coefficient for stationary homogeneous turbulence. Applied Scientific Research, Section A 11(3):245–255, DOI 10.1007/BF03184983

Salhi a, Cambon C (2010) Stability of rotating stratified shear flow: An analytical study. Phys Rev E 81(2):026,302, DOI 10.1103/PhysRevE.81.026302

Sathe A, Mann J (2013) A review of turbulence measurements using ground-based wind lidars. Atmos Meas Tech 6(11):3147–3167, DOI 10.5194/amt-6-3147-2013

Schlipf D, Cheng PW, Mann J (2013) Model of the Correlation between Lidar Systems and Wind Turbines for Lidar-Assisted Control. J Atmos Ocean-Technol 30:2233

Simley E, Pao LY, Frehlich R, Jonkman B, Kelley N (2014) Analysis of light detection and ranging wind speed measurements for wind turbine control. Wind Energy 17(3):413–433, DOI 10.1002/we.1584

Sullivan PP, Patton EG (2011) The Effect of Mesh Resolution on Convective Boundary Layer Statistics and Structures Generated by Large-Eddy Simulation. Journal of the Atmospheric Sciences 68(10):2395–2415, DOI 10.1175/JAS-D-10-05010.1

Townsend AA (1976) The Structure of Turbulent Shear Flow, 2nd edn. Cambridge University Press, United Kingdom, pp 88–91

Wilczek M, Narita Y (2012) Wave-number–frequency spectrum for turbulence from a random sweeping hypothesis with mean flow. Phys Rev E 86(6):066,308, DOI 10.1103/PhysRevE.86.066308

Wilczek M, Stevens RJAM, Narita Y, Meneveau C (2014) A wavenumber-frequency spectral model for atmospheric boundary layers. J Physics: Conference Series 524(1):12,104

Wyngaard JC, Coté OR (1972) Cospectral similarity in the atmospheric surface layer. Q J R Meteorol Soc 98(417):590–603, DOI 10.1002/qj.49709841708

DTU Wind Energy is a department of the Technical University of Denmark with a unique integration of research, education, innovation and public/private sector consulting in the field of wind energy. Our activities develop new opportunities and technology for the global and Danish exploitation of wind energy. Research focuses on key technical-scientific fields, which are central for the development, innovation and use of wind energy and provides the basis for advanced education at the education.

We have more than 240 staff members of which approximately 60 are PhD students. Research is conducted within nine research programmes organized into three main topics: Wind energy systems, Wind turbine technology and Basics for wind energy.

**Technical University of Denmark**
Department of Wind Energy
Frederiksborgvej 399
Building 118
4000 Roskilde
Denmark
Telephone 46 77 50 85

info@vindenergi.dtu.dk
www.vindenergi.dtu.dk